RESIDUAL STRESS MEASUREMENTS IN LOW CARBON STEEL BUTT WELDS BY THE X-RAY DIFFRACTION TECHNIQUE

A thesis presented for the degree of
Master of Engineering in Mechanical Engineering
in the University of Canterbury,
Christchurch, New Zealand.

by

C.F. SOONG

1973

ACKNOWLEDGEMENTS

I wish to thank Mr R.M. Taylor of the Mechanical Engineering Department for his guidance and supervision throughout the course of this project.

My grateful thanks also to Mr M. Rodger, Mr F.W. Fahy and Dr L.A. Erasmus for equipment made available for this project. A note of thanks also to Dr Erasmus for his assistance on certain aspects of the work.

My thanks also to Messrs E.D. Retallick, A.E. Taylor, K. Sinclair and O. Bolt for constructing experimental equipment. I am also grateful to Messrs R.I. Stewart, M.E. Webb and H.J. Anink for assistance given so freely in obtaining equipment required in the experimentation.

To my fellow post-graduate students of the Mechanical Engineering Department, I wish to thank them for their encouragement.

Finally I am indebted to my parent , brothers and sisters, and my wife for their financial assistance and sharing much of the hardship and frustration.

ABSTRACT

Residual stress is a complex subject which requires clear understanding of the phenomenon before any serious attempt in measuring it can be made. A variety of different phenomena is often lumped together under one collective name as residual stress and to complicate it further, these various types of residual stress can exist simultaneously together in an elastic body. Hence when interest is focussed on a specific type of residual stress, not only a distinction in identifying the type of residual stress is required, but it is imperative to be able to separate the various types of residual stress during its measurement.

The magnitude and distribution of residual welding stresses produced in plates due to fusion welding are determined from X-ray diffraction measurements. In the investigation, the gas metal-arc welding process, using CO_2 as shielding gas and 1.2 mm consumable solid wire as electrode, is employed. Residual stresses arising out of two different methods of metal transfer by this process, namely the spray and short-circuiting arc methods, are measured and compared. Effects of edge preparation and weld length upon the residual welding stress patterns are investigated.

Results obtained so far from X-ray measurements have indicated large scatter of experimental points on the residual stress patterns. The author believes it can be attributed to local variation in initial stresses present in the plates before welding. Large variation in initial stress distribution can plausibly obscure the residual welding stress patterns sought in the present investigation.

An interesting question immediately arises from this, namely how the initial stresses add on to the residual welding stresses during welding. This problem has been discussed in length in section 1.2. The main school of throught supports simple additiveness of the two types of residual stress. However, conclusive evidence is lacking in this conjecture. This is mainly attributable to the lack of 'the' method of residual stress measurement upon which reliability can be confidently placed.

Various methods of residual stress measurement have been discussed in section 1.5 and the difference in characteristics is discussed in section 2.4. It would appear that each method has its own drawbacks which are serious when accurate measurements of residual stress are required.

The main drawback with the X-ray methods is the shallow effective penetration of the diffracted X-rays, and thus the method could only reveal surface stresses present in the surface layer of the elastic body. Problems peculiar to the X-ray methods are discussed in Chapter Six where the effects of surface preparation and preferred orientation on X-ray stress measurements are presented.

TABLE OF CONTENTS

LIST OF FIGURES

LIST OF SYMBOLS

n	Order of reflection
$\bar{n}$	Number of points on the $K\alpha_1$ line profile used in the parabolic fitting procedure in the determination of peak angle
d	Lattice spacing
$\lambda, \lambda_1, \lambda_2$	Characteristic wavelengths of the primary X-ray beam
ε	Lattice strain
$\bar{d}$	Depth from the surface
d_0	Lattice spacing for a set of planes in the strain-free condition
d_ψ	Lattice spacing for a set of planes whose normal is inclined to the specimen surface normal with an included angle of ψ.
ψ	Angle between the normal to a set of diffracting planes and the normal to the surface of the specimen.
ψ_0	Angle between the incident primary X-ray beam and the surface normal to the specimen.
θ	Bragg angle of diffraction
θ_0	Diffraction angle in the strain-free condition
θ_p	Angle of inclination of one of the principal stresses with respect to $\sigma_{\beta=0}$o taken in the anticlockwise direction
σ_ϕ	Surface stress measured at the angle ϕ with respect to the principal axis 1.
σ_β	Surface stress measured in the direction β with the rolling direction

β	Angle to the rolling direction
ϕ	Angle to the principal axis 1
$\sigma_1, \sigma_2, \sigma_3$	Principal stresses
$\varepsilon_1, \varepsilon_2, \varepsilon_3$	Principal strains
$\varepsilon_{\phi,\psi}$	Normal strain in any chosen direction in the strain ellipsoid
$\bar{\sigma}_0^2, \bar{\sigma}_1^2, \bar{\sigma}_2^2$	Variances
$\bar{\sigma}_0, \bar{\sigma}_1, \bar{\sigma}_2$	Standard errors
a_1, a_2, a_3	Direction cosines of the normal strain vector $\varepsilon_{\phi,\psi}$ with respect to the principal directions
K	X-ray stress constant
$\bar{K}$	Steady-state value of function f
f	Some function
$\tilde{K}$	Degree of constraint
s_0	Average stress
$\bar{\delta}$	Average deflection
E	Modulus of elasticity
ν	Poisson's ratio
$f(x), f_1(x), f_2(x)$	Intensity distribution functions
x	= 2θ angle
Δx	Separation of the $K\alpha_1$ and $K\alpha_2$ line profile maxima
x_1, x_2	Peak positions of the $K\alpha_1$ and $K\alpha_2$ line profiles
$I_{K\alpha_1 max}, I_{K\alpha_2 max}$	Maximum intensities of the $K\alpha_1$ and $K\alpha_2$ line profiles
$K\alpha_2/K\alpha_1$	Ratio of the maxima of the $K\alpha_2$ and $K\alpha_1$ line profiles
k	Ratio of the maxima of $f_2(x)$ and $f_1(x)$

A_p, B_p, a_p, b_p	Fourier coefficients
N	Number of intervals over which the Kα line profile was recorded
$H(t), G(t)$	Fourier transforms of the functions $h(x)$ and $g(x)$.
$I_{K\alpha}(2\theta), I_{K\alpha_1}(2\theta), I_{K\alpha_2}(2\theta)$	Intensities of the $K\alpha_1$-α_2, $K\alpha_1$ and $K\alpha_2$ line profiles at 2θ angle
$\Delta 2\theta$	Doublet separation
Ω	$= -\frac{(1 - 2\sin^2\theta_0)^2}{2\tan\theta_0}$
η	$= 90^\circ - \theta$
$\bar{t}$	Time
t	Thickness
τ	Time constant
S	Area of cross-section of incident X-ray beam
I_0	Primary X-ray intensity
I	Reflected X-ray intensity
$I_{\bar{d}}$	Reflected X-ray intensity contributed by crystals from a depth $\bar{d}$
$I_{\bar{d}_{inf}}$	Reflected X-ray intensity contributed by crystals from an infinite depth $\bar{d}_{inf}$
L_s	Slit length
ℓ_s	Weld length
L_p	Specimen overall length
W_p	Specimen overall width
$I_{breadth}^{K\alpha_1}$	Integral breadth of the $K\alpha_1$ line profile

Peak $K\alpha_1$	Diffraction angle of the $K\alpha_1$ line profile
$I_{max}K\alpha_1$	Maximum intensity of the $K\alpha_1$ line profile

CHAPTER 1

RESIDUAL STRESS

1.1 Introduction

The existence of residual stress has plagued the beginning of many industries. It makes its appearance by such damaging effects as cracking, warping and stress corrosion.

In the fabrication processes, the most commonly known mechanical effects are the occasional cracking or warping of forgings, castings, or welded structures. Similarly in machining process, inaccuracy in machining is often caused by relief of residual stress.

The phenomena of stress corrosion in deep drawn brass articles and in boiler plates are well known examples of the chemical effects of residual stress in grain-boundary corrosion. These deleterious effects are most noted as in season cracking[1] of cold-worked brass when exposed to an ammoniacal atmosphere, and in caustic embrittlement[2] in boilers when the alkaline feed water together with the service stress attack the steel plates.

1.2 Role of Residual Stress

The role of residual stress during the service of a structure with such stress is a debatable subject. Residual stress may be induced in the course of processing or during fabrication and it may affect the strength of the metal either directly or indirectly through corrosion at the grain boundaries.

In autofrettage processes[3], peening[4] and shot-blasting, they have recognised beneficial effects such as raising the strength of the material. In season cracking, they have disastrous effects. However, in welded structures[5], their effect is contradictory. As reviewed by Cepolina and Canonico[6] in 1971, they reported that Ship Structure Committee in 1947 stated that locked-in stresses do not contribute materially to failure (in regard to World War II Ship failures). In contrast, a subcommittee of the ASME implied that the residual stress adds to the applied stress or service stress to initiate fast fracture.

Similar observations were made by Greene and Holzbaur[7] in 1946. They stated that reaction stresses, which are caused by shrinkage against the reaction of surrounding structure, will add to service stresses. However, it was also stated that it is doubtful if residual stress, which is localised along the weld and heated plate, adds to service stresses in the same manner as reaction stresses. In earlier work done before 1937, Spraragen and Claussen[8] stated that it was not possible to ascertain whether residual stresses are harmful or what happens to them in services.

Support for the additiveness of applied and residual stresses is made by Weck[9], Beedle and Tall[10], and Barton and Hall[12]. More recently, Hall et al.[13] indicated that the residual stresses and externally applied stresses are alike in that they exist in large volume, and their effects are tensorially additive, provided that yielding does not occur.

Hence, the main school of thought supports that residual stress can affect the initiation and propagation of a failure

at stresses below the designed stresses. It usually affects the strength properties of the metal adversely. However, under proper control, beneficial effects can be obtained from these stresses as in autofrettage. The prospect of utilising residual stress to improve the column strength of heavy welded shapes has been considered by Alpsten and Tall[14]. They concluded that the high tensile residual stresses that exist at the welded joints and also at the flame-cut edges improved the compressive load carrying capacity of these weld-fabricated columns when compared with their rolled-counterparts.

In general, residual stresses of the opposite sign to the service stresses will increase the strength of elastic materials. Conversely, residual stresses of the same sign to the service stresses will lower the strength of the material.

1.3 Definition of Residual Stress

The term 'residual stress' can be defined that stress which would exist in an elastic solid body if all the external load, acceleration, and gravitation were removed. The significant point here is that when all external influences have been removed the 'fictitious' stress which remains is called residual stress.

In literature, terms like locked-in[15] or locked-up stress[16a], inherent stress, self-stress, internal stress[17] initial stress[11] and shrinkage stress[8] have often been referred synonymous to residual stress. These terms are equally appropriate in meaning when they are used to describe stresses arising from their respective sources of origin.

1.4 Types of Residual Stress

According to Orowan[18], residual stresses can be classified into two groups as follows:

a. Body stresses - They arise from non-uniformities of external factors, which may be mechanical, thermal, or chemical, may affect different parts of a body differently, even if the material of the body is quite homogeneous.

b. Textural stresses - They arise from textural inhomogeneities, which may either be present in the material initially, or produced by plastic deformation or structural changes, may result even if the external influences acting on the body are uniform.

Body stresses are often referred to as macroscopic stresses or simply 'macrostresses'. In Germany, Macherauch[19] referred to it as residual stress of the first kind. Textural stresses or tessellated stresses[18] are referred to as 'microstresses' or as residual stresses of the second kind.

As summarised by Orowan, the main purpose of the classification is to emphasize the variety of different phenomena lumped together under one collective name as residual stress. The various types of residual stress can exist simultaneously together in an elastic body. Hence, it is important to differentiate it into its components when measuring residual stress in a material containing both kinds of residual stress.

TABLE 1-1: Physical methods of stress measurement.

Method	Physical properties measured	Remark
X-ray methods (22-27)	Crystal lattice dimension.	Quantitative and non-destructive. Measure elastic surface stress only. With control of irradiated area, strain measurements can be refined to point measurements virtually.
Magnetostriction method (20,28,37)	Magnetic parameters e.g., susceptibility, permeability, and remanence.	Quantitative and generally non-destructive. Applicable to ferromagnetic material only. Possibility of measuring stress below the surface.
Eddy current method (20,29)	Electrical resistivity.	Non-destructive and Qualitative.

1.5 Measurement of Residual Stress

1.5.1 Introduction

A number of methods are available for the measurement of residual stress. Like the conventional technique of determining the state of stress in a body, they may be classified under two broad classifications, namely, destructive and non-destructive methods. However, a more meaningful classification can be made, namely physical methods[20] and mechanical methods[21,35].

Most physical methods are non-destructive and they measure both macro- and micro-stresses together. However, to differentiate between these two types of stress, only the X-ray diffraction technique has been developed to such state. The mechanical methods are basically destructive and they only measure the macrostresses. Hence, complete correlation cannot be expected or obtained between the results of residual stress measurements obtained from both physical and mechanical methods especially when the material is subjected to both types of stresses.

In general, most methods involve measuring the strain in the body by some conventional methods of strain gauging and calculating from it the state of stress on the assumption that the usual equations of elasticity theory apply. The exception here is in the physical methods involving the magnetostriction or eddy current technique. These techniques directly relate the measured physical parameters with stress.

1.5.2 Physical Methods

The physical methods measure the change in physical properties with stress. Any physical property of a material which is modified by stress can be used in the investigation

TABLE 1-2: Mechanical methods of stress measurement.

Method	Description
Etching method (21,38)	Use of chemical reagent to detect surface stress. Qualitative and highly destructive. A phenomenon of crack formation closely related to seasonal cracking.
Brittle lacquer (Stress coat) method (21,30)	A combination of the use of stress coat, as an indicator, with stress relief through drilling of shallow holes. Semiquantitative and destructive. Useful for visualization of stress distribution.
Mathar's method (31-34)	Use of electrical strain gauges or mechanical gauges to measure the ensuing strain relieved by drilling small through or blind shallow holes. Quantitative and destructive.
Sachs method (6,35)	Mainly used with cylindrical specimen where the relieved strains brought about by boring are measured by electrical strain gauges or variation in dimensions is measured by micrometer. Quantitative and highly destructive.
Subdivision method (10,14,21)	Method involved small rectangular block containing strain gauges or gauge points to be freed from flat specimen. In depth variation of stress can be measured through progressive machining layer off the surface or by splitting the block. Quantitative and highly destructive.

of residual stress which may exist in a sample of that material. The various physical methods are briefly summarised in Table 1-1.

1.5.3 Mechanical Methods

All mechanical methods involve the process of uncoupling the residual stress by one of these methods, namely, etching, application of plastic strains, sectioning, boring of small through holes or shallow blind holes, and machining. They are therefore destructive methods of stress measurement.

These methods are fully described in texts and only a brief summary is presented in Table 1-2.

1.6 Scope of Research

The measurement of residual stresses in weldments has been pursued almost since the beginning of modern welding. With the introduction of the gas metal-arc welding[39a] process in 1951, the economics of the arc welding process is improved favourably by the versatility and speed of this welding process. In the present work, the author shall endeavour to measure the residual stress distribution in weldments made with the gas metal-arc welding process. Simple butt welds on low carbon steel plates will be studied in conjunction with the gas metal-arc welding process. The shielding gas used in the present work is carbon dioxide. It is relatively a cheaper gas than most inert gases used with the process and its applications[39b] have been widely accepted in the welding of mild and low alloy steel.

The method of stress measurements selected for the present work is the X-ray diffraction technique. The Rigaku Dengki Strainflex unit, which is a portable X-ray diffractometer

using the non-focussing Debye-Scherrer geometry, was used in conjunction with the X-ray stress measurements. With this portable unit, it is possible to take X-ray diffraction measurements on any engineering structure in situ.

Various descriptions of residual stress in weldments are presented and results from previous work are discussed (Chapter 2).

An investigation on the materials used in welding and the preparation of welded specimens is presented (Chapter 3).

The X-ray diffraction method of stress measurement is presented and the basic equations are derived (Chapter 4).

Various methods of analysis of X-ray data for measures of line breadth and peak position of the $K\alpha_1$ component are discussed and the development of the Fourier method, a modified version of the Rachinger method, is presented (Chapter 5).

Effects of surface preparations and preferred orientation on X-ray stress measurements and X-ray elastic constants are presented (Chapter 6).

Results from the present investigation on residual stresses in simple butt welds are presented. A comparison of the present results with published experimental results is discussed (Chapter 7).

An attempt to explain why compressive residual stresses were found on the weld bead is discussed and mechanical testing of the welded plates is made (Chapter 8).

CHAPTER 2

RESIDUAL STRESSES IN WELDMENTS

2.1 Introduction

Residual welding stresses were recognised to exist in weldments since the beginning ot modern welding. Many investigators had attempted theoretical[8,40-44,48] and experimental[6-10,12,14,24,45-47,49] studies on this 'stress of interest'. During the early part of the second world war, residual welding stresses came into importance because welded ships built during that period received considerable unfavourable publicity with regard to structural failures. These events focused attention on the residual stresses in welds and their role in the service of large welded structures.

2.2 Formation of Residual Welding Stresses

In actual welding, many types of residual stresses are generated as a result of thermal and mechanical treatments. At the very first application of heat, a molten puddle formed will serve as a heat source into which the metal can expand. This local heating will set up thermal stresses especially when the surroundings obstruct the expansion of the locally heated region. At sufficiently high temperature, the flow strength of the locally heated metal may be lowered to the extent that the ensuing thermal stresses will cause upsetting in the locally heated metal. The subsequent freezing of the molten pool is not deleterious until temperatures are reached wherein the strength of the metal is sufficiently high to restrict plastic flow. At this point, shrinkage stresses will make their appearance in the upset portion and its surroundings.

Further cooling only affects the distribution of these stresses and not their magnitudes.

The 'fictitious' stresses set up in the welded structure as a result of welding and remaining after the welding is completed and the joint has cooled down are referred to as residual welding stresses. The stresses due to rigid surroundings; that is in the case of welding under constraints, which prevent expansion and contraction of the surrounding metal during the thermal cycle of the welding process, are termed reaction stresses.

However, more localised stresses are also set up during welding. These residual stresses, or microstresses, arise from phase changes such as from liquid to solid, austenite to pearlite and in some cases austenite to martensite. In the case of martensitic transformation, hardening stresses are set up in the zone of structural change in the weld. In extreme cases, cracking at the heat affected zone and weld bead could happen.

In the present investigation, it is the residual welding stresses which are concerned. Reaction stresses are removed by freeing the welded specimen from the restraining jig before actual stress measurements. Hardening stresses will not be a problem in the present work because of the low carbon content of the parent plates and filler metal used. In medium carbon steels to alloy steels, the problem of metallurgical transformation stresses will be more serious. The interaction between welding thermal and metallurgical transformation stresses has been treated by Wilson et al.[48].

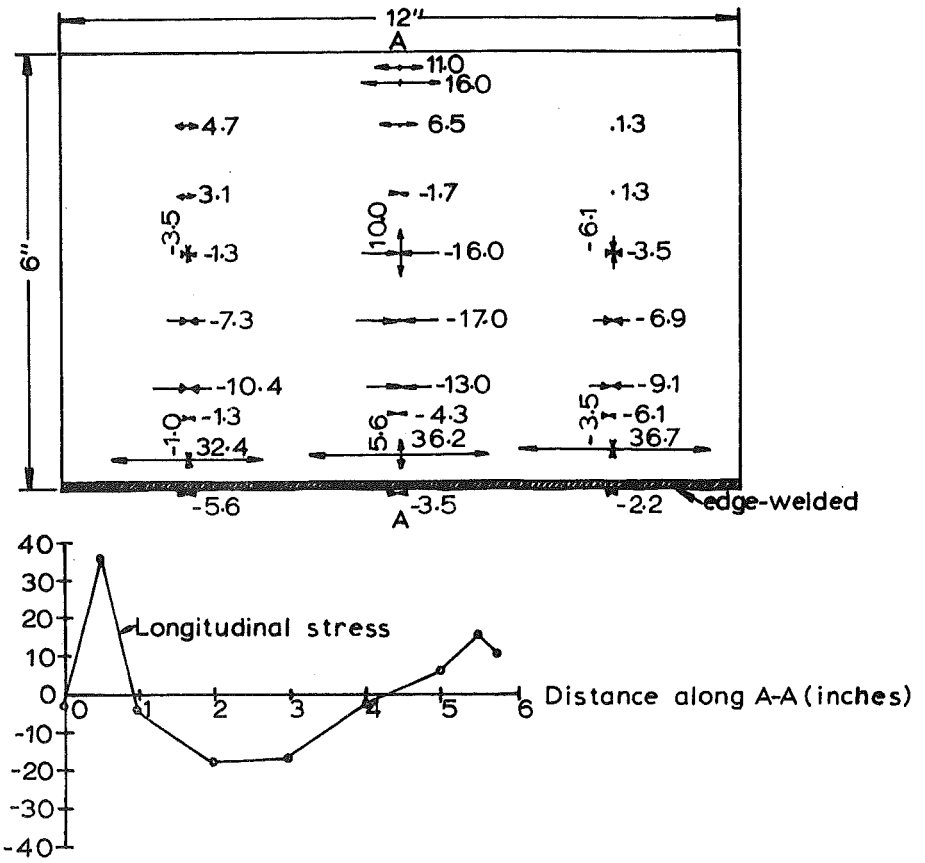

Fig.2.1 Residual stress patterns obtained by X-ray method.(49)

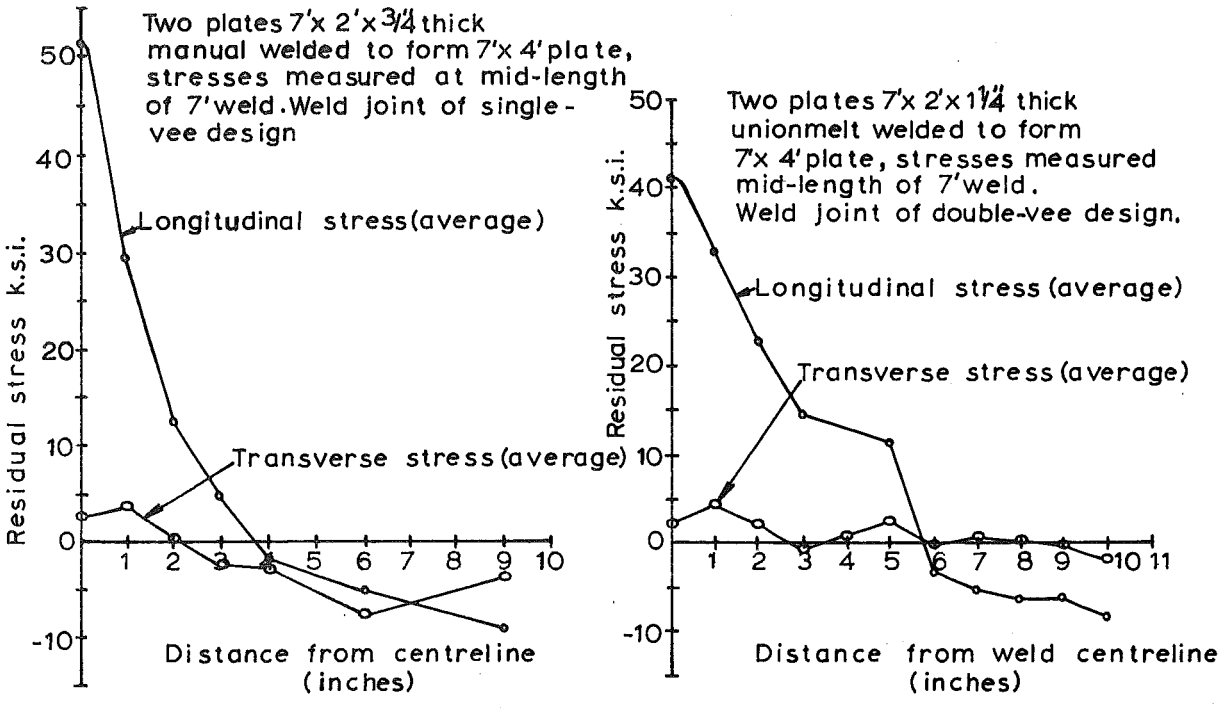

Fig.2.2 Residual stress patterns obtained by Subdivision method.(7)

2.3 Previous Work

Early experimental and analytical studies on residual welding stresses before 1937 were reviewed by Sparagen et al.[8]. In the review, studies on butt joints, fillet-welded joints, T-joints and plug welds were reported. Effects of thickness and welding with and without restraint were also reported. Oxyacetylene and arc welding processes were used in the above studies.

As summarised by Spraragen et al., residual stresses approaching the yield point of the material perpendicular to the weld and at short distances (2 inches or less) therefrom were invariably found in fusion welding of low-carbon steel ½ inch thick or more. The stresses parallel to the weld are even greater as the biaxial, and in very thick plates triaxial, stresses apparently raise the yield point 30% or more. The methods of stress measurement used in the above studies were the Mathar and Subdivision methods.

In 1938, Stephen[47] used a portable Philips back-reflection camera unit to measure the residual stresses in a welded experimental pressure vessel. Stephen used the Huber-Henky theory of Yielding to express his results.

In 1941, Norton and Loring[49] applied the X-ray method to measure the residual stresses near a weld. The two-exposure method was used and the results obtained are shown in Fig. 2.1 for an edge-welded plate.

In 1946, Greene and Holzbaur[7] studied the stress distribution of Unionmelt[50] butt welds in mild steel plate. Single-vee welds and double-vee welds were studied and the stresses were measured by the subdivision technique. Typical stress distribution is shown in Fig. 2.2. Effects of low

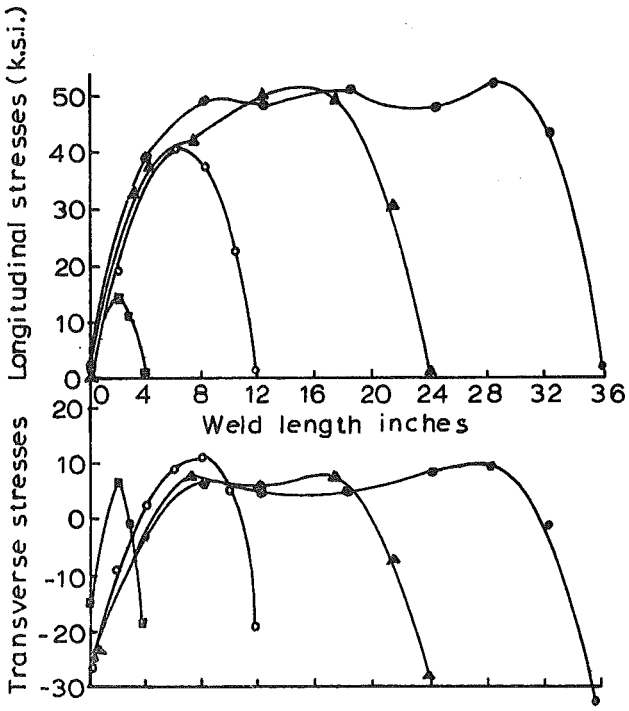

Fig.2·3 Effect of weld length on residual stress patterns[45b].

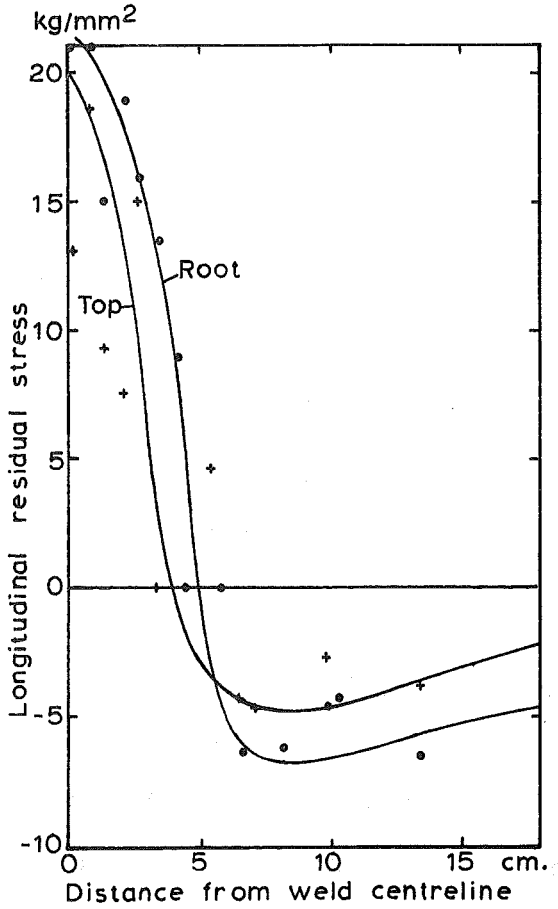

Fig.2·4 Residual stress patterns obtained by Trepanning method[52].

temperature stress relieving of the stress distribution were also studied. In the same year, Meriam et al.[45a] studied the redistribution of Residual Welding Stresses by tensile loading along a Unionmelt weld joining two 3 ft x 12 x 1 inch plates. Meriam et al.[45b] also studied the effect of weld length upon the residual stresses of unrestrained butt welds. The results are shown in Fig. 2.3.

In 1949, Weck[51] studied the residual stress distribution due to welding and concluded that stress approaching the yield point was always found in the welded steel. He also stated that welding procedure was of little influence on the magnitude of the stresses.

In 1955, Gunnert[52] measured the stress distribution on a plate having the dimension 500 x 360 x 15 mm, which was unionmelt welded at the centre. He measured the residual stresses by the trepanning method, but using a mechanical extensometer instead of electrical strain gauges to measure the ensuing relaxed strains. The longitudinal stress distribution is shown in Fig. 2.4.

In 1961, Nagaraja Rao and Lambert Tall[53] studied residual stresses in welded plates. The residual stresses were measured by the sectioning method. Typical distribution of the longitudinal residual stress in the centre welded plates is shown in Fig. 2.5(a). They concluded that there is no great variation of residual stress in welded plates between successive welding runs. Plates smaller than ½ inch in thickness show the same stress patterns on both faces. Furthermore, they showed that the residual stress patterns for edge-welded plates showed high tensile stress at the welded edge and compressive stress further away from the weld (see Fig. 2.5(b)).

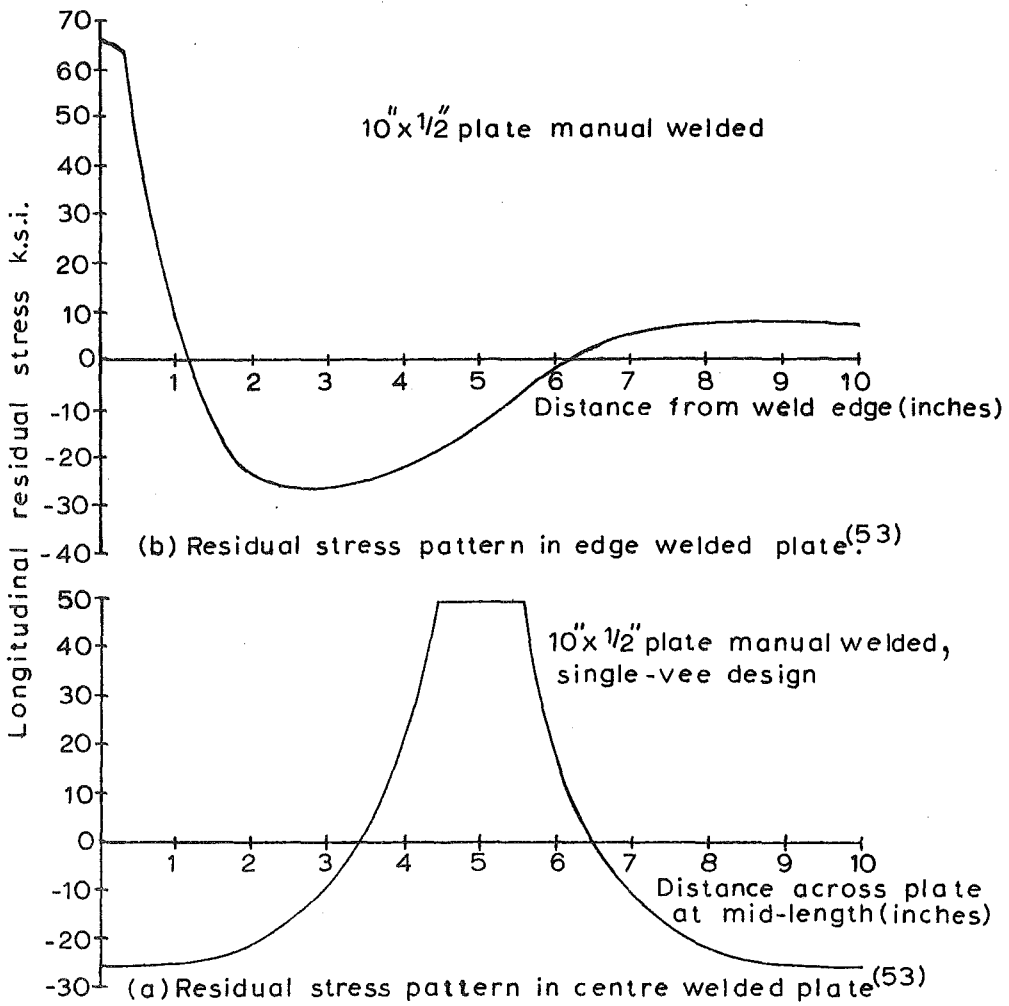

Fig.2·5

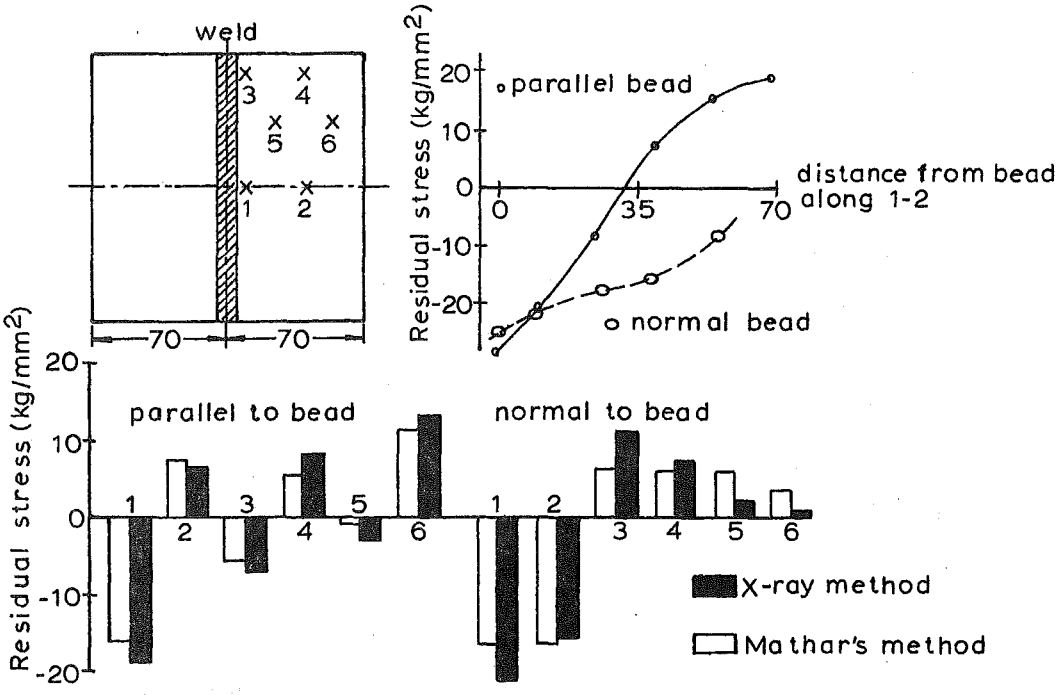

Fig.2·6 Residual stress patterns obtained by Mathar's and X-ray method.(46)

This is similar to results obtained for centre-welded plates.

In 1964, Murakami et al.[46] measured the residual stress distribution on mild steel plates, which were butt welded with a groove angle of 75 deg. by an ordinary a.c. arc welding machine. The X-rays and Mathar methods were applied in the investigation. Characteristic results plotted are shown in Fig. 2.6. The results of both X-ray and Mathar methods of stress measurement showed satisfactory agreement.

2.4 Discussion

With respect to the mechanical methods (Subdivision and Mathar methods), it is interesting to note that the residual stresses in the weld and its vicinity are almost monotonously tensile whilst further away from the weld bead, they are compressive. The residual stresses in the longitudinal direction are generally much larger in magnitude when compared with their transverse components. Furthermore, Rao[53] has shown the residual stress patterns are similar for both edge-welded plate and centre-welded plate. The consistent results obtained by the mechanical methods give confidence in the basic validity of the mechanical methods.

By contrast, residual stress patterns obtained by X-ray method (Norton et al.[49] and Murakami et al.[46]) showed conflicting results. Norton et al. showed the residual stress patterns for the longitudinal stresses to be complex (see Fig. 2.1). Murakami et al. showed stress patterns totally opposite to those obtained by the mechanical methods. However, Murakami et al. also showed good correlation between results obtained by the Mathar and X-ray methods (see Fig. 2.6).

In view of the discrepancy in the results obtained by the X-ray method, residual stress patterns determined by the X-ray method are expected to be complex and difficult to interpret. The disagreements between the mechanical and X-ray measurements are related to basic differences between the characteristic of the two methods.

The basic differences between the X-ray method and the mechanical methods are briefly summarised below:

a. Composition of gauge length

Mechanical methods of strain gauging yield the integrated effect of all the strained crystallites of various constituents (e.g., ferrite, pearlite and cementite in steels) present in the polycrystalline metal and including any which may have yielded plastically over a large gauge length. Whereas in the X-ray method, the elastic changes in lattice spacing of the chosen (hkl) planes from a selected aggregate of strained crystallites of a particular constituent (i.e., ferrite in steel) which is favourably oriented with respect to the incident X-ray beam are measured.

b. Effective depth of penetration

In the mechanical methods, the depth of penetration over which the ensuing strain relaxation is measured can be varied from the total depth of the sample (Subdivision method) to shallow blind hole of depth up to half the diameter of the hole (Mathar's method). In comparison, the X-ray method will only reveal the surface stress down to probably one crystal layer in depth; that is the effective depth of penetration of the soft X-ray beam is of the order of about 10^{-4} inch (see Appendix 1).

In brief, X-ray measurements are sensitive to local variations and surface effects. It is these characteristics, or attributes, which permit the method in determining localised stress in high stress gradient or in-depth variation of stress in machined and hardened surfaces. Therefore the concordance of results between the X-ray and mechanical measurements is not usually expected. A recent comparison[37] of results from X-ray, magnetic and slitting (an extension of Sachs' method of mechanical relaxation) measurements confirmed the above belief.

2.5 The Present Work

For low carbon steels, the distributions of residual stress in straight butt welds, determined by the various methods of stress measurement, were shown to differ in magnitude and character. Results obtained by the mechanical methods (Subdivision and Mathar methods) showed consistent residual stress patterns. However, the patterns were different from those obtained by the X-ray method. In addition, the residual stress patterns obtained by the X-ray method differed amongst workers (as referred to results obtained by Norton et al.[49] and Murakami et al.[46]).

The present work was primarily intended to determine the residual stress distribution in straight butt welds made by the gas metal-arc welding process using carbon dioxide gas for shielding. The X-ray method of stress measurement used in the present work would allow the works of Murakami et al. and Norton et al. to be checked. At the same time, influencing factors affecting the magnitude and distributions of residual stress produced in plates due to fusion welding were investigated.

The objectives of this investigation were:

1. To determine the effect of two different modes of metal transfer, with regard to the gas metal-arc welding process, on the residual stress patterns. The 'spray' and 'dip' or 'short-circuiting' arc techniques were investigated.
2. To determine the effect of weld length upon the residual stress patterns.
3. To determine the effect of weld edge preparations on the residual stress patterns, using single and double vee-notched specimens.
4. To determine the effect of restraint on the residual stress patterns.

NOTE: The aim of studying the effect of restraint on the residual stress patterns was subsequently dropped because it was found that with the present restraining jig, it is not possible to set the goniometer head close enough to the clamped specimen. This mistake in design was due to the fact that the restraining jig was designed and made before the diffractometer arrived. Hence, considerations in the design were based on a picture in a manual which was not dimensioned.

However, for the sake of future work, self-restrained welding specimen is discussed in Appendix 2 and the degree of constraint of the self-restrained specimen is determined by a Finite Element programme.

CHAPTER 3

GAS METAL-ARC WELDING PROCESS, EQUIPMENT, MATERIAL AND SPECIMEN PREPARATION

3.1 Gas Metal-Arc Welding Process

The gas metal-arc welding process is an arc welding process. The heat of welding is provided by an electric arc between a filler metal electrode (consumable) and the work. Shielding of the arc and weld puddle is provided by a continuous flow of gas, as mixture, or a mixture of a gas and a flux. This continuous flow forms an enveloping shield between the weld pool and the atmosphere. The primary purpose of the shielding gas is protection of the molten weld metal from oxidation or contamination by the surrounding atmosphere.

The equipment for the gas metal-arc welding process comprises a power source which provides direct current and is preferably of the constant potential type; a wire feed unit with variable rate; a welding gun or torch with or without water cooling; shielding gas cylinders and other ancillaries.

3.1.1 Advantages of Gas Metal-Arc Process

The gas metal-arc welding process is an important and versatile arc process by which structural metals such as low carbon steel, stainless steel and aluminium can be welded with ease. The production of sound weld with good penetration is characteristic of the gas metal-arc welding process. The metal deposition rate is usually high with the spray metal transfer technique, and stub-end loss is minimal as compared to the conventional manual arc welding.

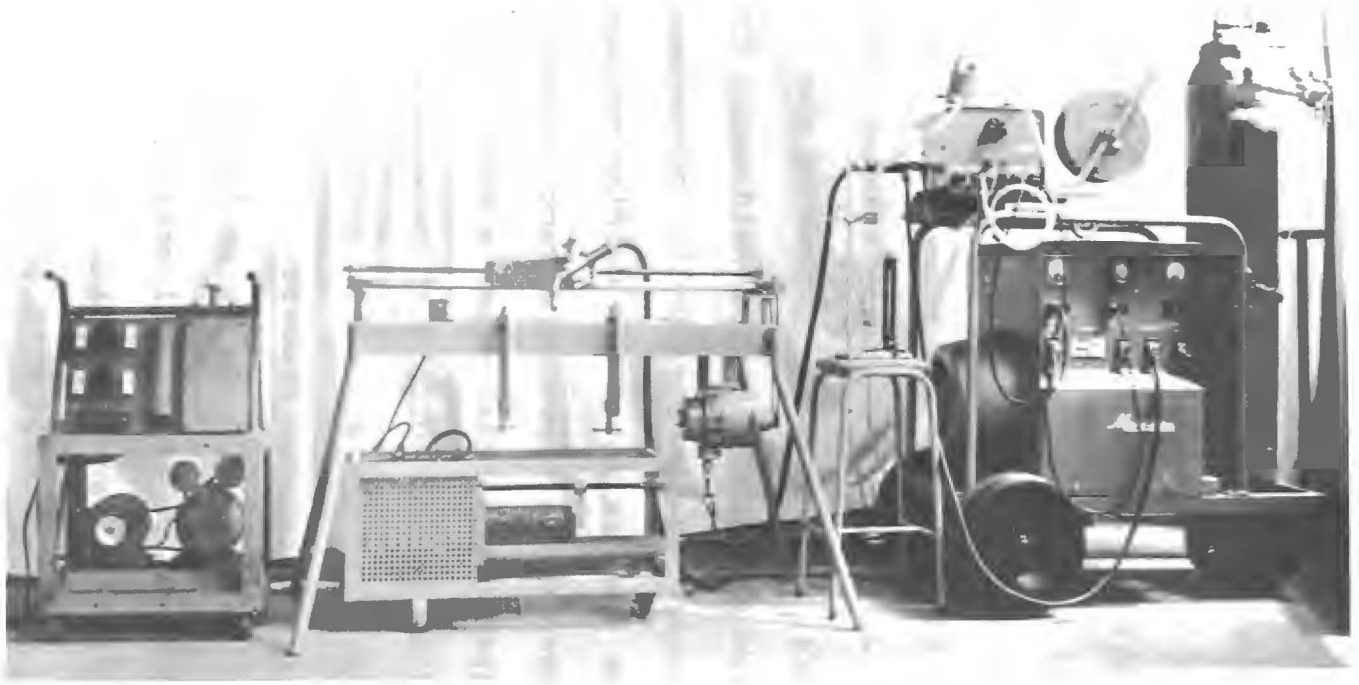

Fig.3.1 Welding equipment. (Showing Ward-Leonard Set, Welding Rig and the Hobart Brothers Micro-wire MIG Welder as from the left).
(Courtesy of Yang, M.E. Thesis, U. of Canterbury)

With the introduction of short-circuiting metal transfer technique, the problem of positional welding is overcome. Hence joints of various sizes and shapes can be welded with the gas metal-arc welding process.

The gas metal-arc welding process, being semi-automatic possesses some of the advantages of automatic machine welding and some of those of hand welding. It is the flexibility and versatility of the process which gives its recent popularity in the welding industry.

3.1.2 Metal Transfer Characteristics

There are three types of metal transfer currently used with the gas metal-arc welding process. They are the "spray", "dip" or short circuiting, and "pulsed" arc transfer.

In the "spray" arc transfer technique, droplets of molten metal are projected from the tip of the electrode through the arc to the work in the form of a spray. Currents of over 200 amps are required and the large heat input to the work resulted in a high metal deposition with excellent penetration.

In the short-circuiting arc method, the metal transfer takes place chiefly during repetitive short circuits through contact of the molten electrode with the weld puddle, rather than by droplets or spray transfer through the arc column. As less heat is available, the molten weld pool freezes very rapidly. Hence welding of light gauge plates is possible without burning through. Welding with a short-circuiting arc employs low currents generally ranging from 50 to 225 amps and low voltages of 12 to 22 volts.

In pulsed-arc welding[54], two levels of current are used. One is continuous at a quite low level and is known as the background current. The other is above the critical or

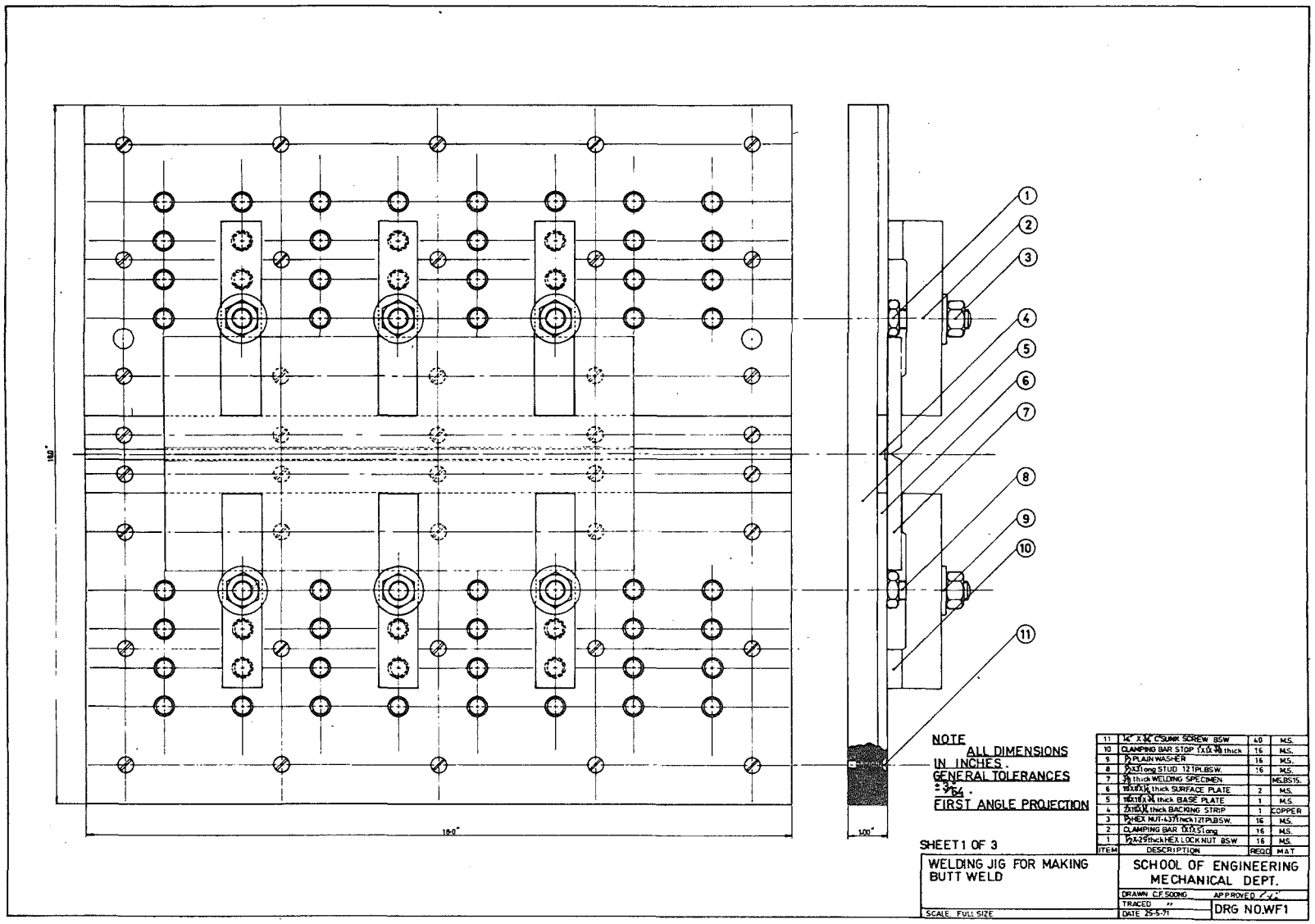

NOTE
ALL DIMENSIONS IN INCHES.
GENERAL TOLERANCES ± 1/64.
FIRST ANGLE PROJECTION

ITEM	DESCRIPTION	REQD	MAT
11	1/4" X 3/4" CSUNK SCREW BSW	40	M.S.
10	CLAMPING BAR STOP 1"x1"x 3/8 thick	16	M.S.
9	1/2 PLAIN WASHER	16	M.S.
8	1/2"x3"long STUD 12TPI.BSW.	16	M.S.
7	3/8 thick WELDING SPECIMEN		MS.BS15.
6	18"x18"x1/2 thick SURFACE PLATE	2	M.S.
5	18"x18"x3/4 thick BASE PLATE	1	M.S.
4	2"x18"W thick BACKING STRIP	1	COPPER
3	1/2 HEX NUT-4371 thick 12TPI.BSW.	16	M.S.
2	CLAMPING BAR 1"x1"x5"long	16	M.S.
1	1/2"x2"9 thick HEX LOCK NUT BSW	16	M.S.

SHEET 1 OF 3

WELDING JIG FOR MAKING BUTT WELD

SCHOOL OF ENGINEERING
MECHANICAL DEPT.

DRAWN C.F.SOONG. APPROVED
TRACED "
DATE 25-5-71
DRG NO.WF1

SCALE. FULL SIZE

Fig.3·2 Restraining jig.

"threshold" current for the wire being used and is intermittent. The background current maintain the arc and melts the end of the wire whilst the pulsed or intermittent current greatly increases the power in the arc for sufficient time to detach the droplet of metal and project it across the weld pool. No short circuit occurs and normally only one droplet of metal is carried across by such pulse.

3.2 Welding Equipment

The welding equipment used in this investigation consisted of a Hobart Brother micro-wire MIG welder, a welding rig and a restraining jig for restraining the specimen. The welding machine and welding rig is shown in Fig. 3.1. The welding machine is of the constant voltage type and the maximum current capacity is rated 300 amps. The welding rig is driven by a variable speed d.c. motor controlled by a Ward-Leonard set. A restraining jig is also specially made for holding the base plates in position and preventing out-of-plane distortion (see Fig. 3.2). The restraining jig is designed so that plates of various sizes can be accommodated when making simple butt welds. The work piece is held down by clamp bars which have been previously calibrated with the aid of a C.E. Johanssen dynamometer.

Philips CO_2 welding wire of 1.2 mm (0.047 inch) diameter is used in all the weldings. The FVRDE specification of the electrode is FV1050. The electrode is recommended for welding mild and low alloy steel. The chemical composition of the electrode and weld deposit as supplied by the supplier (Mesco Riddell of Christchurch) is shown in Table 3-1.

TABLE 3-1: Chemical composition of electrode.

Element	C	Mn	Si	P	S
Percentage	0.11	1.2	0.5	0.02	0.019

TABLE 3-2: Chemical composition of parent plate.

Element	C	Si	Mn	P	S	N
Percentage	0.19	0.5	0.89	0.015	0.022	0.004

Shielding is provided by carbon dioxide which is pre-heated during welding. The flow of gas is regulated by a flow meter.

3.3 Material

In the present investigation, a low carbon steel of 0.19%C was chosen because when welding low carbon steel it is easy to duplicate or even better the strength properties of the base metal in weld metal.

The low carbon steel was supplied by the Hirohata Works of Japan in the form of hot-rolled 3/8 inch thick plates. The chemical composition of the plates as supplied by the manufacturer is shown in Table 3-2.

The above metal was quoted to have the property of good weldability and conformed to BS15.

3.4 Heat Treatment of Material

3.4.1 Introduction

To facilitate the X-ray measurements, the material must be conditioned so that under diffraction condition, sharp diffraction lines are produced. Conditions[16c] which promote this occur when the grain size is of the order of 10^{-4} cm and the grains are randomly oriented.

With unduly large grain size, the number of crystallites irradiated is not sufficient for coalescence of the individual reflection spots to take place, and hence lead to spotty unrepresentative reflection and inaccuracies in the X-ray lattice-parameter measurements. However, with too small grain size (less than 10^{-4} cm), undesirable broadening[16d]

(a) Hot-rolled (film stationary)

(b) Hot-rolled (film oscillated)

(c) Recovery annealed (film oscillated)

Fig.3-3 Back reflection patterns.

Section normal to R.D. Section parallel to R.D. Section parallel to rolled surface

10 μm

Fig.3-5 Microstructures of recovery annealed specimen.

of the diffraction line profiles would occur.

When grains are not randomly oriented, the specimen is said to possess a definite orientation texture[16e]. The preferred orientation arises from the particular crystallographic texture developed by previous treatment; in this particular case the hot rolling process will develop crystallographic texture much similar to that as in cold rolling[55a]. Anisotropy caused by preferred orientation of crystals give rise to directional dependence of mechanical properties[55b] as well as X-ray stress constants[26,27,56]. Greater detail will be discussed in section 6.5.

3.4.2 Examination of Metal Condition in the Hot-rolled State

The back-reflection patterns from the hot-rolled plate showed diffused and broadened Debye Scherrer halo from (310) planes (see Fig. 3.3(a),(b)). This indicates the presence of microstresses in the hot-rolled metal. With regard to the orientation texture, a fairly continuous Debye Scherrer halo (refer to patterns taken with stationary film in Fig. 3.3(a)) with some prominent arc indicates that some degree of preferred orientation is present. Also from the continuous Debye Scherrer halo, it can be deduced that the grain size is of the order of 10^{-4} cm[16c].

3.4.3 Experimental Procedure

Since a suitable grain size already prevails in the as-received metal, a suitable stress-relief annealing[57a] procedure will be satisfactory. For most practicable methods of stress-relieving, recovery annealing[55c] up to the recrystallisation temperature is often required. For low carbon steel, the recrystallisation temperature is about $650^{o}C$[55d]; actual recrystallisation temperature depends on the thermal and mechanical history of the sample.

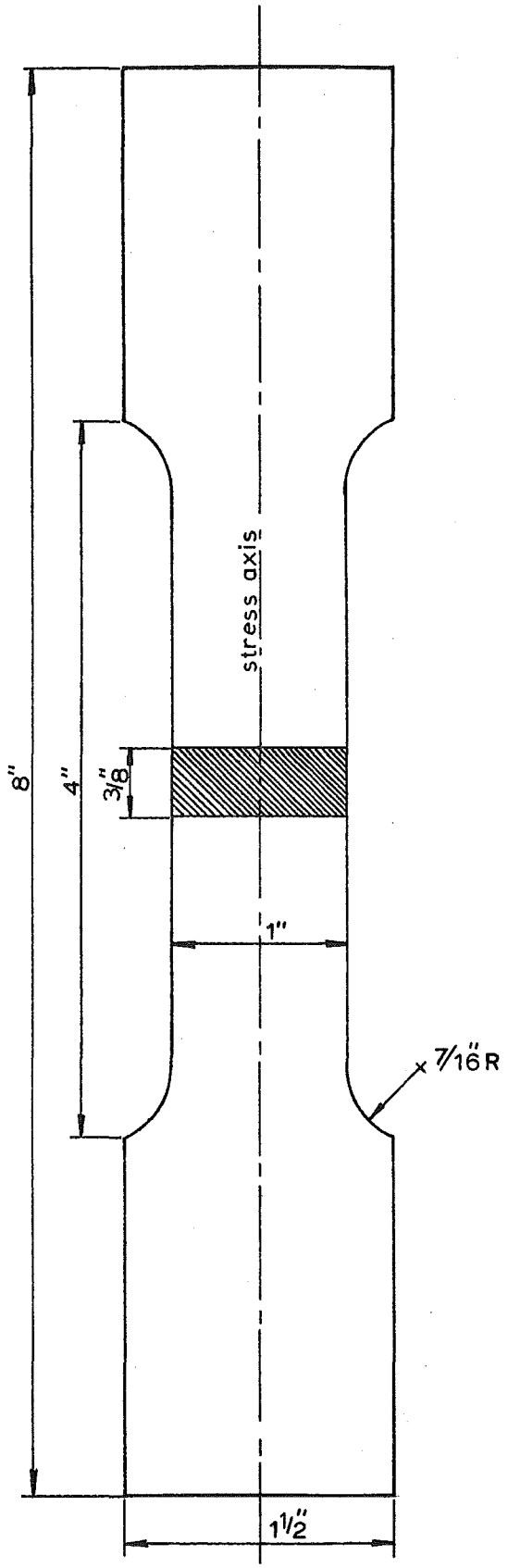

Fig.3.4 Flat tensile specimen

In the present work, all parent plates for welding and tensile specimens for calibration purposes were recovery annealed at 650°C in a Gallenkemp Muffler furnace. After a soaking period of 1½ hr at the annealing temperature, the specimens were air cooled. It would be better if vacuum annealing was used and thus eliminate scaling, but such a facility is not available in the present work.

3.4.4 Results

To ascertain the effectiveness of the stress-relief annealing treatment, back reflection pattern was obtained from the same specimen, which was recovery annealed at 650°C for ½ hr (see Fig. 3.3(c)). The much sharper Debye Scherrer halo indicated a substantial reduction in microstresses had taken place. However, care must be taken when making such interpretation because line breadth is also affected by stacking fault[16f] and crystallite size[16d].

The back reflection pattern (see Fig. 3.3(c)) from the annealed specimen also showed a lesser prominence of some of the arcs evident in the pattern obtained in the as-received condition (see Fig. 3.3(b)). This indicated a slight reduction in the degree of preferred orientation brought about by the onset of recrystallisation. However, such conjecture is not totally true as some doubts[55e] have been expressed on the actual effect of recrystallisation on the deformation texture initially present in a deformed metal.

3.4.5 Mechanical Testing and Microscopic Examination of Material

Mechanical testing of tensile specimens (see Fig. 3.4) in the as-received and annealed state were conducted on the STE (Southwark Tate-Emery) tensile testing machine. A sample size

TABLE 3-3: Mechanical properties of material

Mechanical Property	Perpendicular to R.D.		Parallel to R.D.	
	Hot-rolled	Recovery Annealed	Hot-rolled	Recovery Annealed
U.T.S.(kg/mm^2)	46.20	44.30	46.00	43.53
Yield Stress(kg/mm^2)	29.90	28.64	28.80	27.65
% Elongation	37.0	42.0	40.0	45.0

Hardness before annealing: 155VPN.

Hardness after annealing: 140VPN.

of three was used for each sample and the results are tabulated in Table 3-3.

The recovery annealing resulted in a slight decrease in strength and about 5% increase in percentage elongation. However, the same difference in directional strength prevails as in both conditions. This is due to orientation texture which remains unaltered by the recovery annealing process.

From examination of the microstructures in the annealed specimens, the grain size as measured by the mean linear intercept method[59a] is about 10 μm (see Fig. 3.5). The measured grain size of 10 μm or 10^{-3} cm is not significantly higher than the required mean grain size of the order of 10^{-4} cm for production of perfectly sharp, continuous Debye Scherrer halo[16c]. Macrosegregation[59b] was not observed in any of the micrographs.

3.4.6 Conclusion

It can be concluded that the hot-rolled structural plates are sound with reasonably small grain size. After heat treatment, the mechanical strength of the annealed metal is good and ductile. The directional strength did vary with direction parallel and perpendicular to the rolling direction, but only by a small amount. Preferred orientation is observed from back-reflection patterns, but it is not marked as in some highly deformed steel[60]. All in all it can be concluded that the material is reasonably conditioned for X-ray measurements.

However, it remains to be seen whether the presence of a small degree of preferred orientation will affect the X-ray stress constants by any significant amount (see section 6.5).

TABLE 3-4: Welding Conditions.

Settings	Short-circuiting arc	Spray arc
Arc Voltage, volts	23	32
Current, amps	145	280
Polarity	DCRP*	DCRP*
Welding Speed, in./min.	9	18
Wire feed position on Control Cabinet.	2.4	4.8
Extension of electrode from contact tube to work piece, in.	1/2	1/2
Wire Diameter, in.	3/64	3/64

*DCRP - Direct current reversed polarity with electrode positive.

3.5 Preparation of Welded Specimens

3.5.1 Introduction

Simple butt welds were made for the study of residual stress distribution in weldments. Plates with single vee groove and double vee groove preparation (see Fig. 3.6) were gas cut from a large hot-rolled plate and the edges were machined. The included angle of the groove was 60 deg. The parent plates were subsequently recovery annealed at 650^{o}C for 1½ hr and air cooled. Descaling of the annealed parent plates was required and the edges to be welded were cleaned with carbon tetrachloride prior to welding. The plates were welded automatically on the welding rig with the spray and short-circuiting techniques under conditions listed in Table 3-4.

To study the effects of mode of metal transfer, weld length and weld edge preparations as described in section 2.5, a number of specimens were welded. Various weld lengths, weld edge preparations and modes of metal transfer were used. All the specimens were welded under restraint.

3.5.2 Selection of Welding Conditions

Preliminary work was required to establish the welding conditions for the spray and short-circuiting arc technique. Information from text or handbooks is scanty with regard to welding conditions for both methods of metal transfer used in conjunction with carbon dioxide shielding gas.

The burn off rate of 0.047 inch diameter steel electrode with carbon dioxide shielding gas was determined. A linear relationship was obtained between the wire speed and welding current. When plotted with burn off curves for steel electrode

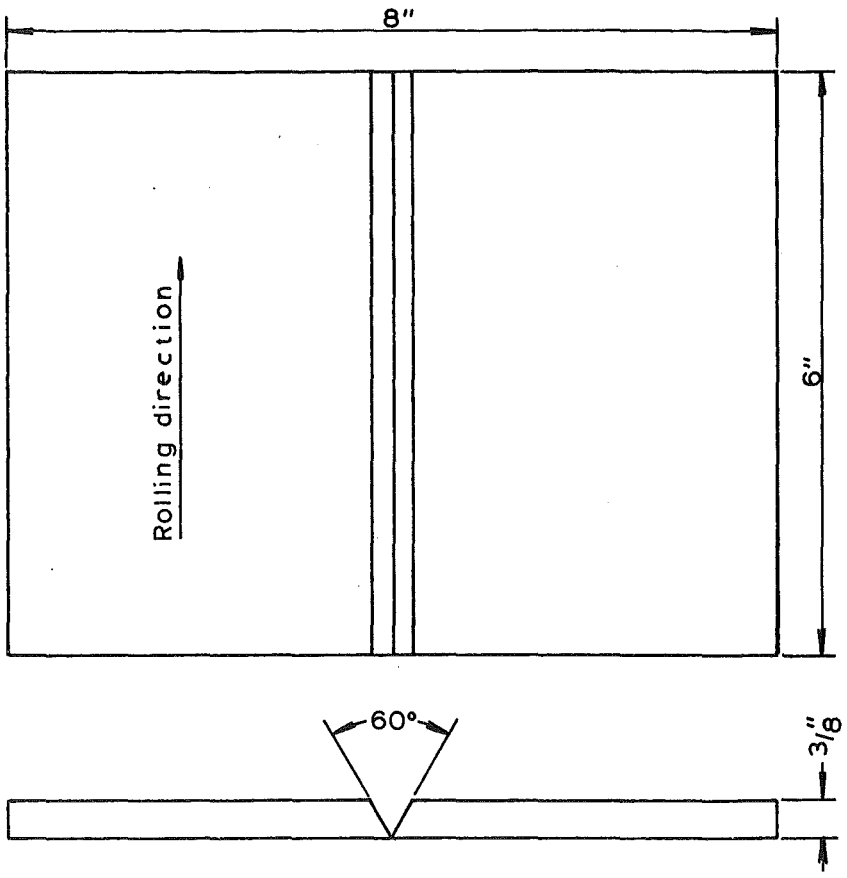

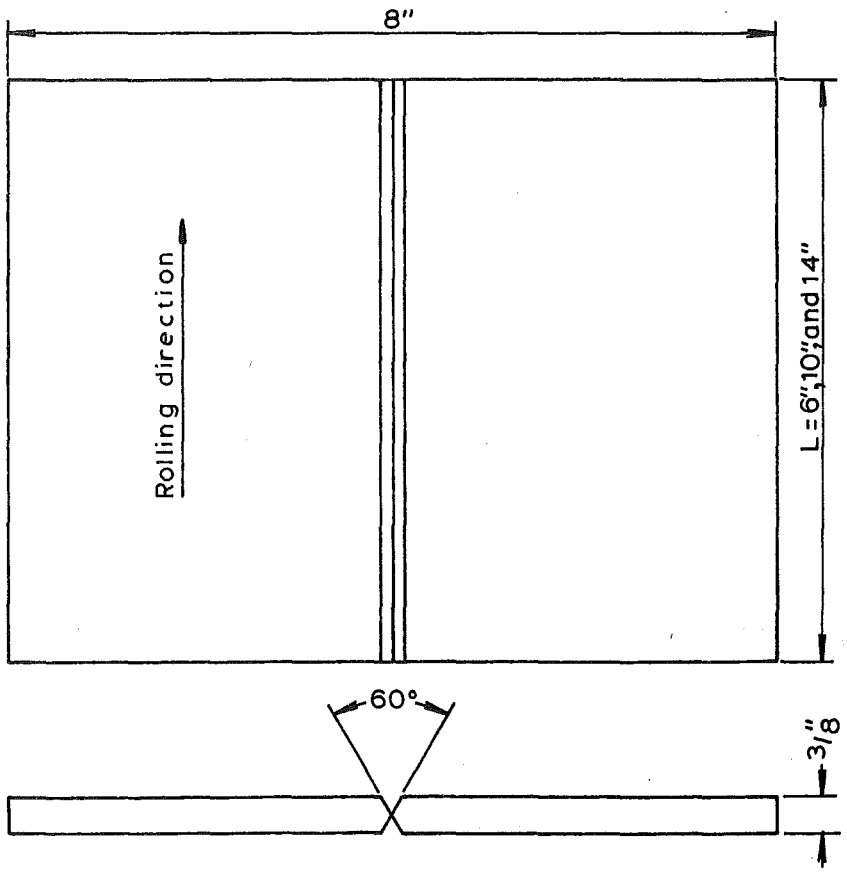

Fig.3·6 Plates of single- and double-vee groove.

with argon or argon -2% oxygen gas[39b], the burn off curve for the 0.047 inch diameter electrode with carbon dioxide gas falls in place quite well for the particular electrode size (see Fig. 3.7).

During the course of the investigation, direct welding current was employed on reversed polarity[39c] (electrode positive). Straight polarity was not used because it is generally not recommended when using straight carbon dioxide for shielding. Moreover, reversed polarity used with the gas metal-arc welding process provides maximum heat input into the work, which in turn produces relatively deep penetration. Another unique quality of the reversed polarity mode is that it removes oxides from parent metal, thus creating a relatively clean and good quality weld deposit.

In the reversed polarity mode, the short-circuiting arc prevails up to current level of about 200 amps. The closed-circuit voltage is normally in the range of 12 to 20 volts, but this can sometimes be increased to 30 volts to suit the particular joint being made[57b]. The actual mode of transfer is difficult to observe through a shielding mask; especially in the short-circuiting arc condition with rapid alternation from arc to short-circuit condition at a rate that may exceed 100 per second. However, the short-circuiting arc produces a buzzing sound that is easily heard. In the spray transfer mode, the mode of transfer tends to be globular and spattery. To obtain true spray mode, higher current level must be used, but the present machine limits the maximum current capacity to 300 amps. The "spray" or globular mode of metal transfer prevails from current level of about 230 amps at 32 volts.

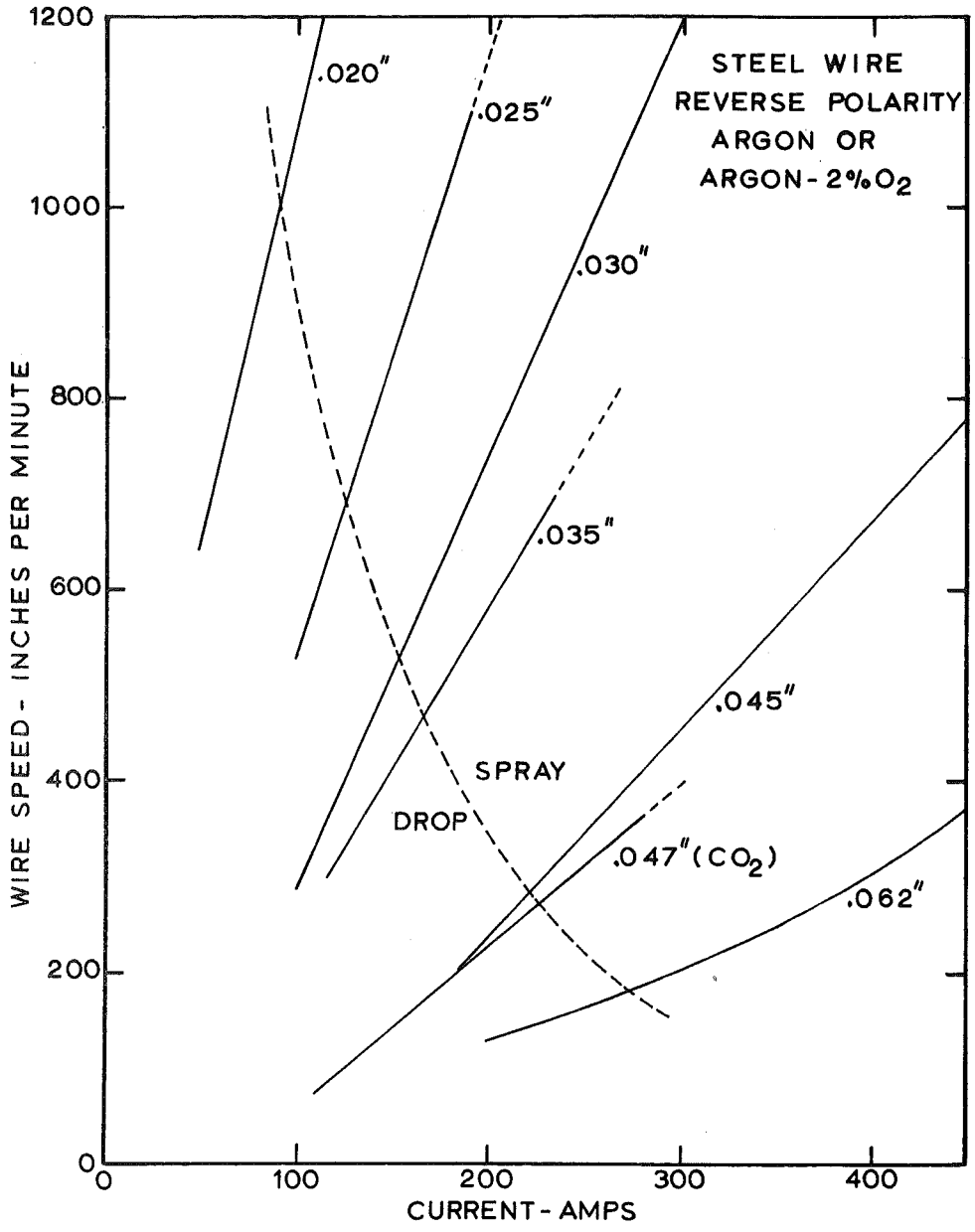

Fig.3·7 BURN-OFF CURVES OF STEEL GAS METAL-ARC ELECTRODES.[39b]

Proper welding conditions were established for both short-circuiting and spray transfer mode. Trial runs were made on similar joints of single and double vee groove preparation and four passes were required to fill each weld joint. The established welding conditions are tabulated in Table 3-4.

3.5.3 Welding Procedure

Prior to welding, it is usually desirable to clean surfaces that are to be welded. This was accomplished by swabbing the surfaces with cotton wool soaked in carbon tetrachloride.

The parent plates were positioned on the restraining jigs with a root gap of 3/64 inch. Clamping bars were applied at 2 inch intervals. Clamping force of 1 ton was applied per clamp to hold the parent plates rigidly during welding.

Since four passes are required to fill the joint, interpass cleaning is required. With the gas metal-arc welding process, no slag is produced. However, oxide films are formed on the weld metal and wire brushing between runs is necessary. In between runs, the previous weld bead is allowed to cool sufficiently to room temperature before the next run begins. Starting and run-off tabs approximately 2 inch square were fitted to each end of the joint to assure sound welds clear to the ends. These tabs were sawn off after welding was completed.

3.5.4 Results

To study the effects of weld length, mode of metal transfer and weld edge preparation on the residual stress patterns in simple butt welds, a series of plates of fixed width, but of varying length and weld edge preparation were welded as shown

TABLE 3-5: Welded Specimens.

Specimen No.	Dimensions of each half of parent plates. Width(inch)	Length(inch)	Edge Preparation	Metal Transfer mode
1	4	6	sv	short circuiting
2	4	6	sv	spray
3	4	6	dv	spray
4	4	6	dv	short circuiting
5	4	10	sv	short circuiting
6	4	14	sv	short circuiting

sv: single vee notched.

dv: double vee notched.

in Table 3-5.

In the investigations into the effects of two different modes of metal transfer and two different weld edge preparations on the residual stress patterns, Specimens No. 1, 2, 3 and 4 were used, whilst specimens No.1, 5 and 6 were used in the investigation into the effect of weld length upon the residual stress patterns.

CHAPTER 4

X-RAY DIFFRACTION METHOD OF STRESS MEASUREMENT

4.1 Introduction

The application of the X-ray diffraction method to the measurement of the stress and strain states in a polycrystalline metal was first attempted in 1925 by Lester and Abborn[61]. They measured the lattice parameter changes in a thin strip of steel subjected to tension. The accuracy of their measurements was poor because the lattice parameters were determined from reflection in the low Bragg angle region, that is in the forward reflection region.

It was not until 1930, when Sach et al.[62] introduced the flat back-reflection camera, was accuracy improved sufficiently for practical application. This was possible by incorporating the high Bragg angle in the determination of the lattice parameter. This can be shown as follows:

From Bragg's law

$$n\lambda = 2d \sin \theta \tag{4.1}$$

where n = order of reflection

θ = Bragg angle

d = lattice spacing

λ = characteristic wavelength of the X-ray radiation used.

Differentiating equation (4.1),

$$\frac{\Delta\theta}{\Delta d} = -\frac{1}{d} \tan \theta. \tag{4.2}$$

It can be seen that as θ approaches 90°, the sensitivity, $\frac{\Delta\theta}{\Delta d}$, is a maximum, that is for a given small change in lattice

spacing d, the greatest possible change in the diffracted angle is produced.

4.2 Review of Literature

Many investigators[22-27,63-66] have applied the X-ray method of stress measurements for measuring macroscopic and microscopic stresses in polycrystalline metals. The single-exposure, double-exposure and the $Sin^2\psi$ methods have been reviewed by Rutledge[26]. The advances made in equipment design have also aided the recent development of the X-ray method.

More important is the ready availability of portable X-ray equipment used in the field of X-ray stress analysis. Portable X-ray equipment for the back-reflection camera technique of X-ray stress measurement has been used by Norton and Rosenthal[24], Stephen[47] and many others. However, portable X-ray equipment using the counter-method of stress analysis has only been introduced recently. These modern portable X-ray units (Toshiba MDP 103 Type and the Rigaku Dengki Strainflex unit) or more appropriately known as X-ray Stress Analysers, have high versatility in setting over any large specimen. Camera and counter-methods can be used in conjunction with these units. Furthermore, sophisticated X-ray detecting devices like proportional and scintillation counters with or without pulse-height discrimination can be incorporated into these units. These developments have opened up the field of X-ray stress analysis for practical applications in laboratories as well as in industries.

However, the validity of X-ray stress measurements has been questioned ever since it was introduced by Sach et al.[62].

Many investigators have given different views and interpretations, sometimes contradictory, on results obtained with the X-ray method. These differences are centred on the question as to whether residual tensile or compressive surface stresses, which develop during unilateral plastic compression or extension of polycrystalline materials respectively, were macrostresses or microstresses.

Donachie and Norton[67] found disagreement between X-ray and mechanical relaxation determinations in fcc metals. This can be explained by the characteristics of the two different methods; namely the X-ray diffraction method may indicate a residual stress to exist while mechanical methods do not. It stems from the fundamental difference in X-ray and mechanical methods as explained in section 2.4; that is stresses of macroscopic nature and microscopic nature could plausibly contribute to X-ray results whereas only the macroscopic stresses contribute to the mechanical results. Macherauch[68] studied the effect in unilaterally deformed copper by both X-ray and mechanical methods and he confirmed the existence of a macrostress distribution producing the surface stress. On the other hand, Woods[71] concluded, from his experiment on aluminium, copper, iron and mild steels specimens, that the presence of a single macroscopic stress system acting in the surface of the specimen was inconsistent with the X-ray findings. It follows that the residual stress system is different for different grains, hence suggesting a microstress system.

Most investigators did find the axial residual stresses induced by plastic deformation do not satisfy the macroscopic equilibrium. The magnitude and sign of the fictitious stress depend upon the crystallographic plane used to diffract the X-ray beam. This was confirmed by the extensive works of Hayashi[69].

Another controversy exists with regard to the magnitude of the surface stress induced by externally applied load. Wagner et al.[70] found the effective stress in the surface region penetrated by the radiation is lower than the average stress applied to the specimen. This is supported by the experimental evidence of Kolb and Macherauch[72] who concluded that the less severe work hardening in the surface resulted simply from the surface grains being under less constraint with regard to slip processes, thus suggesting a soft surface layer. Support for a soft surface layer is provided by Brydges[76], Fourie[73] and Block and Johnson[74] while Krammer et al.[75] and Kajima et al.[77] concluded that a hardened layer is found at the surface of plastically deformed crystals.

All in all the X-ray diffraction method of stress measurement is a powerful and intriguing method of stress measurement, but many inherent problems peculiar to the method must be considered in evaluating residual stress measurements. A summary on the above problems has been provided by Macherauch[19].

4.3 Present Work

The primary intention of the present study is to apply the X-ray method of stress measurements to determine the residual stress distribution in weldments. In view of the problems mentioned in section 4.2 with regard to the X-ray method, a clearer understanding of the method must be sought.

Principally the problem of directional dependence of tensile stress-strain relation obtained from hot-rolled steel plates must be investigated (see section 3.4.5). This anisotropy arises from internal stresses and crystallographic texture and is characterized by different elastic constants and flow strength in different directions in the metal.

The effect of surface preparations on the results of X-ray measurements must also be investigated (see section 6.3). Since the penetration of the soft X-ray is shallow, a stress free method of surface removal is required so that the prepared surface is representative of the remaining bulk material. An effective method of stress-free removal of metal is by electropolishing[78]. This procedure of surface preparation is fairly standard as has already been indicated in most recently published papers[27,29]. However, much detail is lacking, and some preliminary works must be conducted in the present study (see Appendix 3).

Finally, from a survey of the various methods of analysis of the X-ray data, the resolution of the composite $K\alpha$ line profile into its $K\alpha_1$ and $K\alpha_2$ components is important. The overlapping of the $K\alpha_1$ and $K\alpha_2$ line profiles together with the convolution of the experimental distributions like those due to geometrical or instrumental and physical aberrations formed the obscured scattering distribution observed

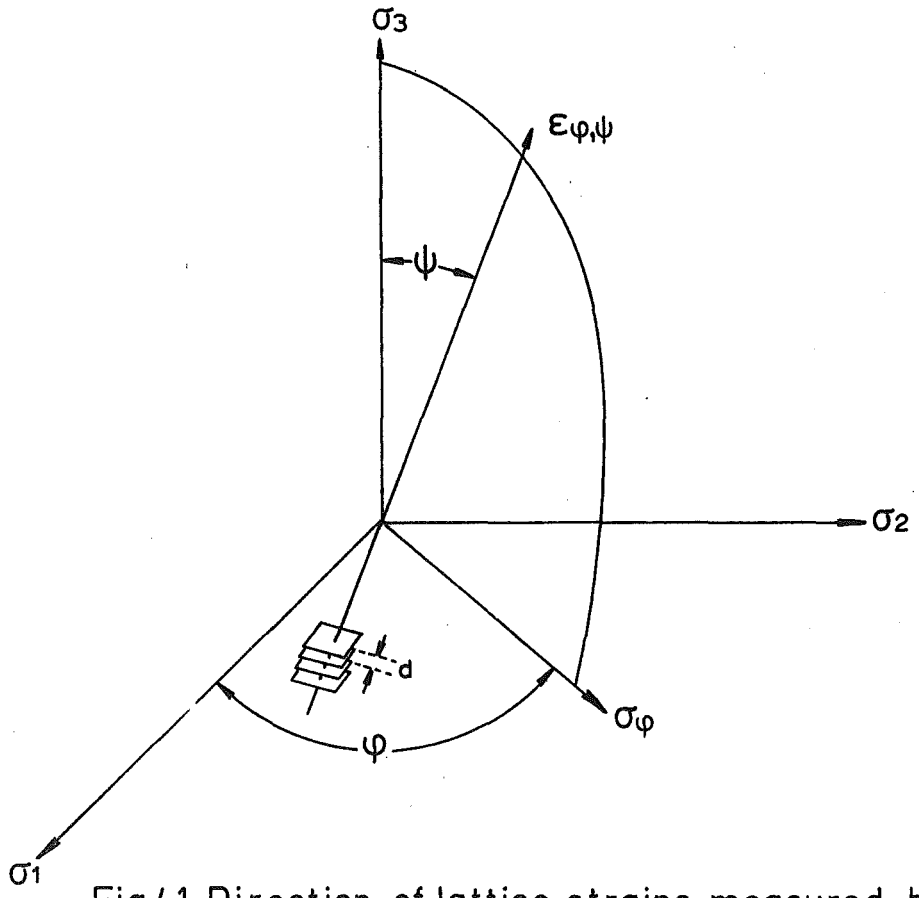

Fig.4·1 Direction of lattice strains measured by X-rays.

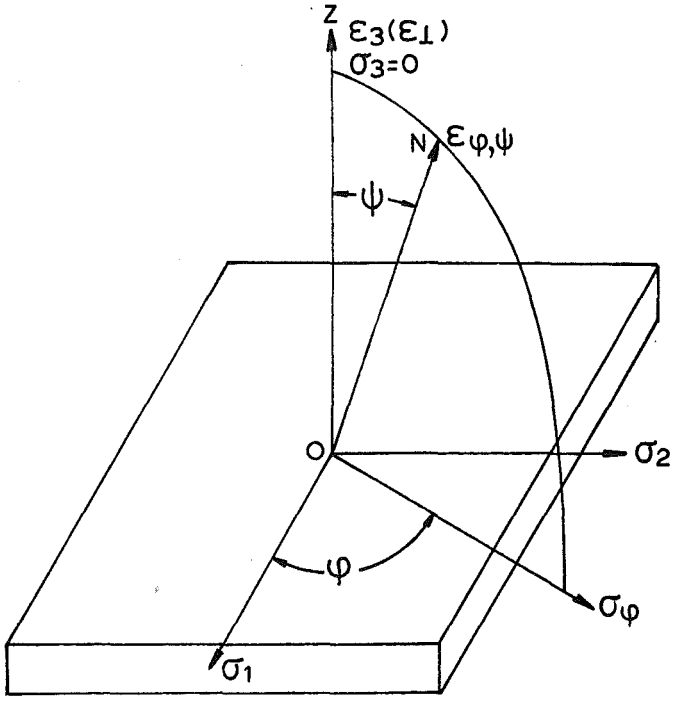

Fig.4·2 Biaxial stress system.

experimentally. To correct for these aberration effects, various methods have been proposed and this is discussed in section 5.2.

4.4 Basic Principles

In X-ray diffraction studies, the use of a point source emitting a monochromatic X-ray of wavelength λ, a specimen with diffracting planes having lattice spacing d and a point detector is generally assumed. Also assumed to hold in the diffraction condition is the general Bragg law as expressed by equation (4.1).

By differentiating the Bragg equation, we have:

$$\varepsilon \equiv \frac{\Delta d}{d} = - \cot \theta \, \Delta\theta \tag{4.3}$$

where ε is the lattice strain.

Since the diffraction angle is measured in terms of 2θ angle, equation (4.3) can be conveniently expressed as follows:

$$\frac{\Delta d}{d} = - \frac{\cot \theta \, \Delta 2\theta}{2} \tag{4.4}$$

or alternatively as

$$\frac{\Delta d}{d} = - \frac{\cot \theta \, \Delta \tan 2\theta}{2 \sec^2 2\theta} \tag{4.5}$$

$$\text{i.e. } \varepsilon = - \frac{\cot \theta (1 - 2 \sin^2\theta)^2 . \Delta \tan 2\theta}{2}$$

Consider a set of planes whose normal is inclined to the specimen surface normal by the angle ψ (see Fig. 4.1), the lattice strain, ε_ψ, can be expressed by the expression

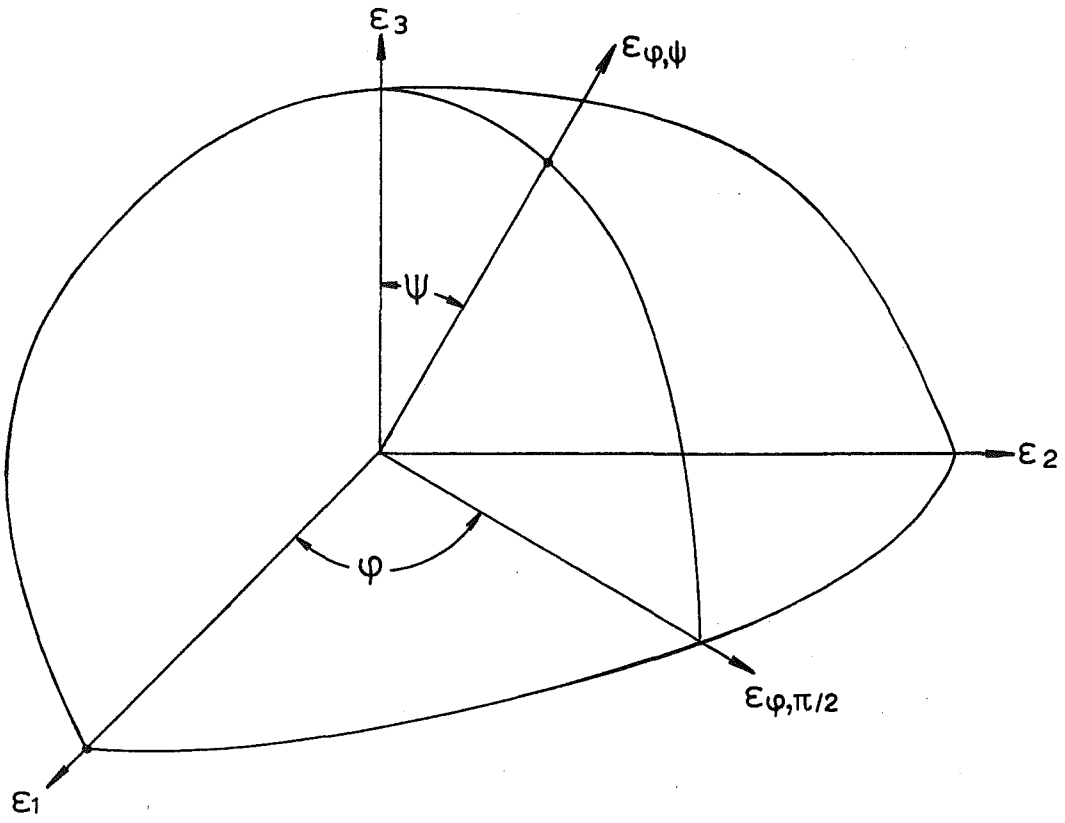

Fig.4-3 Strain ellipsoid.

$$\varepsilon_\psi \equiv \frac{d_\psi - d_0}{d_0}$$

$$= - \frac{\cot \theta_0 (1 - 2 \sin^2\theta_0)^2 (\tan 2\theta_\psi - \tan 2\theta_0)}{2} \qquad (4.6)$$

where θ_0 is the diffracted angle for the set of planes with lattice spacing d_0 in the stress free condition and respectively, θ_ψ and d_ψ in the strained condition.

In X-ray stress measurement, it is without exception that the lattice strain, $\varepsilon_{\psi,\phi}$, is measured and then related to the surface stress component, σ_ϕ (see Fig. 4.2), by stress-strain relations derived in the next section.

4.5 Equations for Analysis of Stress and Strain

For general three dimensional elastic and isotropic stress systems, the following principal stress-strain formulae hold:

$$\varepsilon_1 = \frac{1}{E} (\sigma_1 - \nu(\sigma_2 + \sigma_3))$$

$$\varepsilon_2 = \frac{1}{E} (\sigma_2 - \nu(\sigma_3 + \sigma_1)) \qquad (4.7)$$

$$\varepsilon_3 = \frac{1}{E} (\sigma_3 - \nu(\sigma_1 + \sigma_2))$$

where $\sigma_1, \sigma_2, \sigma_3$ are the principal stresses

$\varepsilon_1, \varepsilon_2, \varepsilon_3$ are the corresponding principal strains.

From the general strain ellipsoid[80] (see Fig. 4.3), the normal strain $\varepsilon_{\phi,\psi}$, in any arbitrarily chosen direction is given by the approximate equation for ellipsoid of strain:

$$\varepsilon_{\phi,\psi} = a_1^2 \varepsilon_1 + a_2^2 \varepsilon_2 + a_3^2 \varepsilon_3 \qquad (4.8)$$

where a_1, a_2, a_3 are the direction cosines of the strain vector $\varepsilon_{\phi,\psi}$ with respect to the principal directions of the three principal strains defining the strain ellipsoid. Similarly, from the stress ellipsoid we have for the normal stress:

$$\sigma_{\phi,\psi} = a_1^2\sigma_1 + a_2^2\sigma_2 + a_3^2\sigma_3. \tag{4.9}$$

By substituting the principal strains from equation (4.7) into equation (4.8) we obtained:

$$\varepsilon_{\phi,\psi} = \frac{1+\nu}{E}(a_1^2\sigma_1 + a_2^2\sigma_2 + a_3^2\sigma_3) - \frac{\nu}{E}(\sigma_1+\sigma_2+\sigma_3) \tag{4.10}$$

Since the effective depth of penetration in X-ray measurements is shallow (about 10 μm), only the surface stresses will be revealed. The stress system (see Fig. 4.2) measured can be approximated by a biaxial stress system with the stress component normal to the surface assumed zero; that is $\sigma_3 = 0$.

From equation (4.10) we have

$$\varepsilon_{\phi,\psi} = \frac{1+\nu}{E}(a_1^2\sigma_1 + a_2^2\sigma_2) - \frac{\nu}{E}(\sigma_1+\sigma_2) \tag{4.11}$$

where
$$\begin{aligned} a_1 &= \cos\phi \sin\psi \\ a_2 &= \sin\phi \sin\psi \\ a_3 &= \cos\phi. \end{aligned} \tag{4.12}$$

Furthermore, from equation (4.9), the surface stress component, σ_ϕ, can be expressed as

$$\sigma_\phi = \cos^2\phi\sigma_1 + \sin^2\phi\sigma_2 \tag{4.13}$$

where $\psi = 90^\circ$.

Therefore, by substituting σ_ϕ into equation (4.11), the lattice strain $\varepsilon_{\phi,\psi}$ is expressed as

$$\varepsilon_{\phi,\psi} = \frac{1+\nu}{E} \sin^2\psi \, \sigma_\phi - \frac{\nu}{E} (\sigma_1+\sigma_2) \tag{4.14}$$

which is the basic equation used in X-ray stress measurements. It must be noted that equation (4.14) is based on the assumptions that each crystal in the aggregate of a poly-crystalline metal is isotropic and homogeneous.

4.6 The $\sin^2\psi$ and Double-Exposure Methods of Surface Stress Measurements

The double exposure and $\sin^2\psi$ methods of surface stress measurements are based on the basic relation for the X-ray stress analysis (c.f. equation (4.14)). By differentiating equation (4.14) with respect to $\sin^2\psi$, we have:

$$\frac{\Delta\varepsilon_{\phi,\psi}}{\Delta\sin^2\psi} = \frac{1+\nu}{E} \sigma_\phi \tag{4.15}$$

From equations (4.6) and (4.15) we have

$$\frac{\Delta \tan 2\theta_\psi}{\Delta \sin^2\psi} = - \frac{(1+\nu)}{E} \cdot \frac{2}{\cot \theta_0 (1 - 2 \sin^2\theta_0)^2} \cdot \sigma_\phi \tag{4.16}$$

Hence the surface stress σ_ϕ can be expressed as

$$\sigma_\phi = - \frac{E}{1+\nu} \cdot \frac{\cot \theta_0 (1 - 2 \sin^2\theta_0)^2}{2} \cdot \frac{\Delta \tan 2\theta_\psi}{\Delta \sin^2 \psi} \tag{4.17}$$

This equation (4.17) forms the basis of the so-called $\sin^2\psi$ method so commonly referred to in X-ray stress analysis.

By rewriting equation (4.17), the standard expression for double-exposure method can be expressed as:

Rigaku Dengki Strainflex Unit (Showing Ratemeter, Recorder and X-rays Controller).

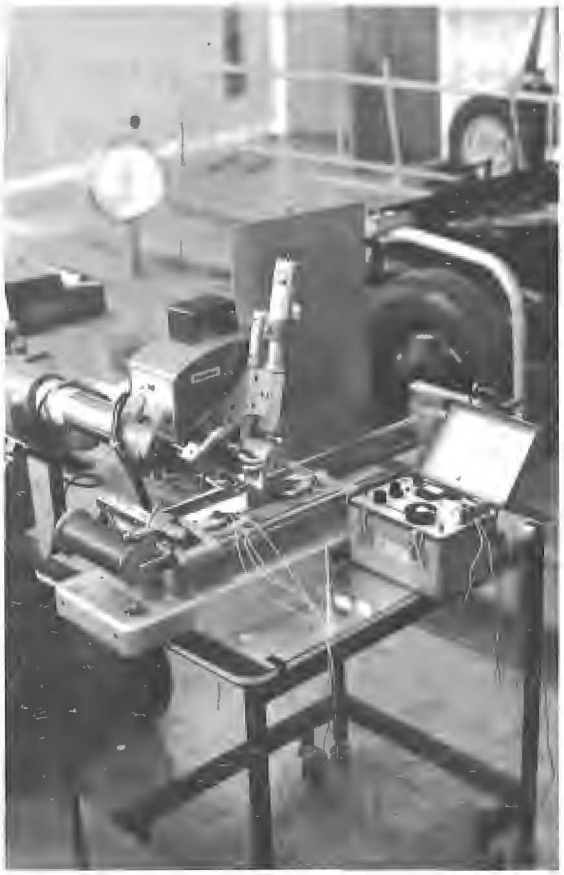

Calibration Set-up (Showing Goniometer, G.M. Counter, Hounsfield Tensometer and Budd Strain Bridge).

Fig.4·4 X-rays unit and calibration set-up.

$$\sigma_{\phi} = \frac{K(\tan 2\theta_{\psi_2} - \tan 2\theta_{\psi_1})}{(\sin^2\psi_2 - \sin^2\psi_1)} \qquad (4.18)$$

where

$$K = -\frac{E}{1+\nu} \cdot \frac{\cot \theta_0 (1 - 2 \sin^2\theta_0)^2}{2} \qquad (4.19)$$

When using the $Sin^2\psi$ method, four or more values of lattice strain at different ψ inclinations, which are chosen such that the value of $\sin^2\psi$ assumes equal intervals are measured. From the slope of $\Delta \tan 2\theta_{\psi}/\Delta \sin^2\psi$, which is obtained by the least mean square line obtained from the plot of $\tan 2\theta_{\psi}$ as a function of $\sin^2\psi$, together with the X-ray stress constant, the value of the surface stress, σ_{ϕ}, can be computed. It is not imperative that the lattice strains be measured at equal intervals of $\sin^2\psi$ value because the least mean square line can still be drawn with unequal intervals of $\sin^2\psi$ values.

The $Sin^2\psi$ method is time consuming and the tedium is often obviated by resolving to the quicker and simpler double-exposure method when large numbers of stress measurements are to be taken as required in the present work. The stress constant K must be obtained by substituting appropriate values of the X-ray elastic constants into equation (4.19). The X-ray elastic constants are known to be different from the bulk mechanical elastic constants for anisotropic material like steel. So the stress constant K was obtained experimentally as described in section 6.5.

TABLE 4-1: Conditions of X-ray stress measurements.

Method	Parallel Beam Method
X-ray	CoKα radiation
Diffraction Planes	(310)
Soller Slit	0.26
Mask	4mm width
Filter	Fe
Detector	G.M. counter
Scanning Speed	$\frac{1}{4}$deg./min.
Chart Speed	10mm/min.
Count Full Scale	1000cps
Time Constant	8sec
Tube Voltage	29kV
Tube Current	8.5mA.
Incident Angle	$\psi_o=0^\circ, 35^\circ$

4.7 Diffractometer Measurements

4.7.1 Equipment

A portable X-ray stress analyser (Rigaku Dengki Strainflex unit) was employed in the determination of surface stress in flat specimens. The unit, which is shown in Fig. 4.4, incorporates the non-focussing Debye-Scherrer geometry in the design of the goniometer. This is a much simpler design in comparison to the parafocussing Bragg-Brentano geometry[59c,70] which incorporates many moving parts and suffers from misalignment problems. However, with the parafocussing geometry and using the 2θ scanning method[59d,79,81] higher intensity and resolution of the X-ray can be obtained.

Parallel beam for diffraction was provided by fitting soller slits on the source and detector ends. With this feature, specimen setting is made easy and any slight shift of the specimen setting position has no adverse influence upon the detection of X-ray diffraction angle. Furthermore, distance setting is simplified by the provision of a setting jig on the goniometer head.

The line profiles of the samples were recorded continuously using a Geiger Mueller Counter probe in conjunction with a ratemeter and recorder.

4.7.2 Conditions and Method of X-ray Stress Measurements

The conditions of X-ray stress measurements are shown in Table 4-1.

The double-exposure method was employed in the measurement of surface stress. Inclination angles of the X-ray beam with respect to the surface normal used were $\psi_0 = 0$ deg. and $\psi_0 = 35$ deg. This is shown schematically in Fig. 4.5. The

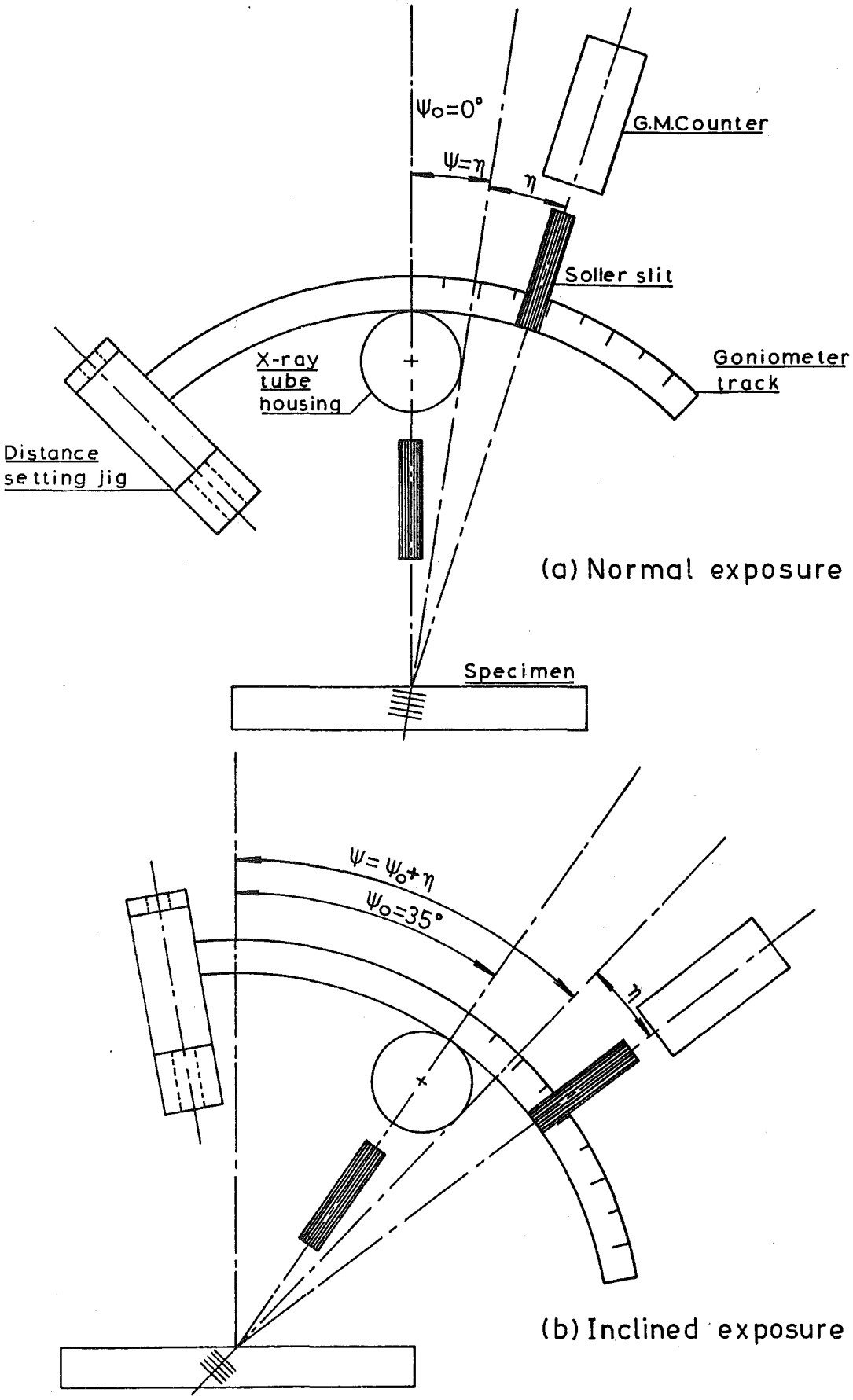

Fig.4·5 Diffraction geometry(schematic).

nominal inclination angle of ψ_0 = 35 deg. was employed in the double-exposure method mainly because during the calibration ex periment to obtain the X-ray elastic constants, the Hounsfield tensometer used for straining the tensile specimens permits a maximum inclination angle of ψ_0 = 40 deg. only (see Fig. 4.4).

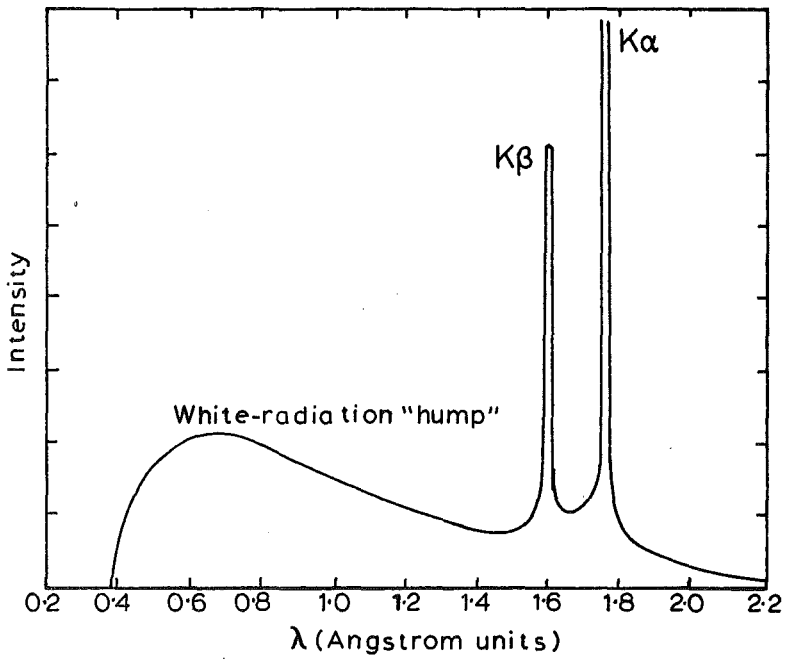

Fig.5·1 Spectrum of X-rays from Cobalt.

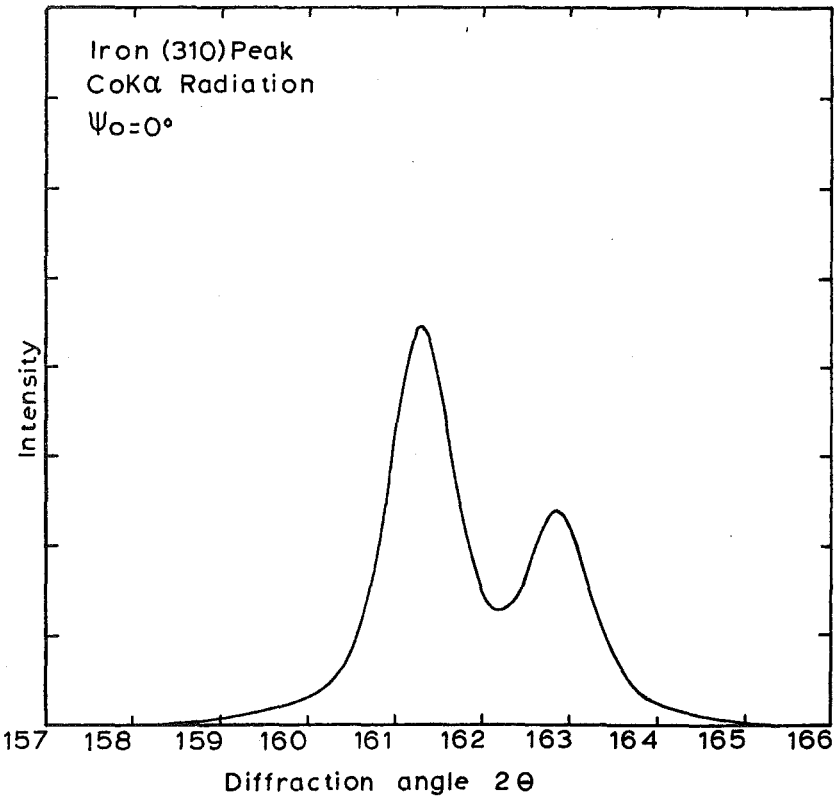

Fig.5·2 Typical diffraction profile of the $K\alpha_1$-α_2 peak.

CHAPTER 5

ANALYSIS OF X-RAY DATA

5.1 Introduction

In X-ray diffraction studies, the use of a point source emitting monochromatic X-ray of wavelength λ, a specimen with diffracting planes having lattice spacing d and the planes are of negligible physical dimensions, and a point detector is generally assumed. Under such ideal diffraction conditions, and for specific λ and d used, the diffracted X-ray will take the form of a line profile of negligible width at diffracted angle, θ, which satisfies Bragg law (c.f. equation (4.1)).

In reality, the source and detector have finite size, the emission line has a spread of wavelength, the specimen may be strained with imperfect or distorted lattice, and the diffracting planes have definite variable dimensions. The output of a crystallographic X-ray tube can be regarded as consisting of the so-called white or continuous radiation, with a wide wavelength range, and the characteristic line spectrum of the target of the tube (see Fig. 5.1).

In the present work, CoKα radiation was chosen for diffraction and a Fe-filter was used to attenuate the Kβ and background radiations. The resulting experimental line profile from the (310) planes of iron exhibits a double peaked profile (see Fig. 5.2). This was due to the not truly monochromatic Kα radiation which consisted of the $K\alpha_1$ and $K\alpha_2$ lines of the intensity ratio of $K\alpha_1 : K\alpha_2 = 1 : 2$ and separated by about 0.004 $\mathring{A}$. Furthermore, the experimental line profile is not symmetrical and it is asymmetrically broadened and possibly

shifted by various aberrations inherent in the geometry of the X-ray stress analyser. Physical aberrations[58c] will also contribute significantly to the breadth and asymmetry of the experimental line profile.

In diffractometry, measures of the peak position and line breadth of the experimental line profile are sought. In view of the broadened and unresolved Kα line profile observed experimentally, it is desirable to obtain measures of the peak position and line breadth of the resolved $K\alpha_1$ line, so that changes in peak position and line breadth brought about by the overlapping of the $K\alpha_1$ and $K\alpha_2$ line profiles can be corrected. So the aim of this chapter is to find a standard method of analysis of the observed line profiles and obtain from it the relevant peak positions and line breadths of the $K\alpha_1$ components.

5.2 Review of Literature

Several methods have been proposed in literature[82-87] for resolving the experimental composite Kα line profile into its $K\alpha_1$ and $K\alpha_2$ components. The various methods proposed can be classified under (a) 'Unfolding' method, and (b) Rachinger method.

(a) 'Unfolding' method

The 'Unfolding' method, can be attributed to Stokes, who measured from an annealed specimen which exhibits no diffraction broadening the aberration profile, g(x), which is formed by the fold of the instrumental aberrations and emission-line profile and using the function, g(x), to unfold the diffraction profile, f(x), from the broadened experimental line profile, h(x) as follows:

$$f(x) = \int \left\{\frac{H(t)}{G(t)}\right\} \exp(-2\pi ixt)dt \qquad (5.1)$$

where H(t) and G(t) are the Fourier transforms of the functions h(x) and g(x).

This practical method of Stokes is used by many investigators[70] in their analysis of the line shape of the pure diffraction profile; hence obtaining the measure of the pure integral breadth. It must be noted that Stokes' method has inherent instability problem when the line broadening due to the instrument is small compared to the required line width[90]. Furthermore, Stokes' method neglects the dispersion effects which are significant for $2\theta > 120^{o}$ [59e].

(b) Rachinger method

The Rachinger method[84] of separation of the $K\alpha_1$ and $K\alpha_2$ line profiles from the composite $K\alpha$ line profile takes the following assumptions:

1. $$I_{K\alpha}(2\theta) = I_{K\alpha_1}(2\theta) + I_{K\alpha_2}(2\theta) \qquad (5.2)$$

2. $$I_{K\alpha_2}(2\theta) = I_{K\alpha_1}(2\theta - \Delta 2\theta)/2 \qquad (5.3)$$

where $I_{K\alpha}(2\theta)$, $I_{K\alpha_1}(2\theta)$ and $I_{K\alpha_2}(2\theta)$ are the intensities at diffraction angle 2θ,

$\Delta 2\theta$ is the doublet separation,

$I_{K\alpha_2}(2\theta)_{max}/I_{K\alpha_1}(2\theta)_{max} = 0.5$.

In application, Rachinger assumed that the two $K\alpha_1$ and $K\alpha_2$ components have rigidly symmetrical profiles about their centroidal positions and enforced that the measured intensities of $I_{K\alpha}(2\theta)$ be recorded at a regular 2θ interval such that the doublet separation is an integral number of coordinates. These requirements are made to simplify the original graphical procedure.

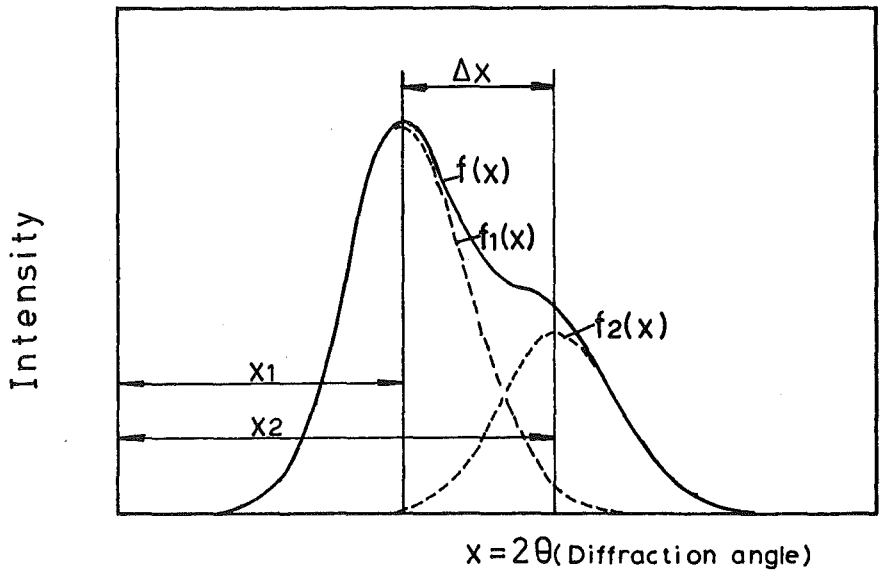

Fig. 5·3 Resolution of Kα doublet.

In 1960, Taira et al.[85] used Fourier series to represent the line profiles. With this modification, the Rachinger method can be applied to separate asymmetrical line profiles of the $K\alpha_1$ and $K\alpha_2$ components from the experimental $K\alpha$ line profile. Moreover, the observed intensity pattern needs only to be measured at arbitrary regular intervals of 2θ. Furthermore, Taira et al. corrected the resolved $K\alpha_1$ line profile for the effects of Lorentz-polarization factor and the specimen absorption factor. It is in the far back reflection region ($2\theta \geqslant 140^{o}$) where contributions to the line breadth and position of all the aberrations except axial divergence becomes less important whilst the Lorentz-polarization factor and dispersion increases.

5.3 Selected Method of Analysis of X-ray Data

5.3.1 Introduction

In the present study, a computer programme was written in a similar line as proposed by Taira et al.[85]. The assumptions made are as follows:

1. $f(x) = f_1(x) + f_2(x)$ (5.4)

where: $x = 2\theta$ angle,

$f(x)$ is the intensity distribution function of the experimental $K\alpha$ line profile,

$f_1(x)$ and $f_2(x)$ are the intensity distribution functions of the $K\alpha_1$ and $K\alpha_2$ component respectively (see Fig. 5.3).

2. $f_2(x) = k.f_1(x-\Delta x)$ (5.5)

where: $k = I_{K\alpha_2(max)}/I_{K\alpha_1(max)}$,

Δx is the doublet separation in 2θ angle.

Substituting equation (5.5) into equation (5.4), we have

$$f(x) = f_1(x) + kf_1(x-\Delta x) \tag{5.6}$$

The value of k used by Taira and others was taken as 0.5. Actual measurement of the relative intensity of the $K\alpha_2$ and $K\alpha_1$ characteristic lines by William[89] showed that $I_{K\alpha_2(max)}/I_{K\alpha_1(max)}$ ratio for CoKα radiations was 0.497. In fact, Williams measured the relative intensity of various target elements with atomic number from 24 to 52 and found the relative intensity varied only very slightly from element to element and the average relative intensity ratio of the $K\alpha_2$ and $K\alpha_1$ characteristic lines was 0.5003. It must be noted that William uses a calcite crystal to diffract the X-ray in the above measurements.

True doublet separation, Δx, can be obtained by considering Bragg equation. From the Bragg equation (c.f. equation (4.1)), we have:

$$\lambda_1 = 2d \sin x_1/2$$
$$\lambda_2 = 2d \sin x_2/2 \tag{5.7}$$

and $\Delta x = x_2 - x_1$

where: λ_1, λ_2 and x_1, x_2 are the characteristic wavelengths and peak positions of the $K\alpha_1$ and $K\alpha_2$ lines respectively.

5.3.2 Mathematical Analysis

The experimental Kα line profile, f(x), and the $K\alpha_1$ line profile, $f_1(x)$, can be represented by the following Fourier series:

$$f(x) = \sum_{p=0}^{N/2} \left(A_p \cdot \cos \frac{2\pi px}{L} + B_p \cdot \sin \frac{2\pi px}{L}\right) \qquad (5.8)$$

$$f_1(x) = \sum_{p=0}^{N/2} \left(a_p \cdot \cos \frac{2\pi px}{L} + b_p \cdot \sin \frac{2\pi px}{L}\right) \qquad (5.9)$$

where: $0 \leqslant x \leqslant L$,

A_p, B_p, a_p and b_p are the Fourier coefficients,

and N is the number of intervals over which the Kα line profile was measured to represent f(x).

Substituting equation (5.9) into equation (5.5), we have:

$$f_2(x) = k \sum_{p=0}^{N/2} \left\{a_p.\cos \frac{2\pi p(x-\Delta x)}{L} + b_p.\sin \frac{2\pi p(x-\Delta x)}{L}\right\} \qquad (5.10)$$

and on expanding equation (5.10),

$$f_2(x) = \sum_{p=0}^{N/2} \left\{k\left(a_p.\cos \frac{2\pi p\Delta x}{L} - b_p.\sin \frac{2\pi p\Delta x}{L}\right) \cos \frac{2\pi px}{L}\right\}$$

$$+ \sum_{p=0}^{N/2} \left\{k\left(a_p.\sin \frac{2\pi p\Delta x}{L} + b_p.\cos \frac{2\pi p\Delta x}{L}\right) \sin \frac{2\pi px}{L}\right\} \qquad (5.11)$$

From equations (5.4), (5.8), (5.9) and (5.10) we have by comparison of coefficients,

$$\begin{aligned} A_p &= a_p + k\left(a_p.\cos \frac{2\pi p\Delta x}{L} - b_p.\sin \frac{2\pi p\Delta x}{L}\right) \\ B_p &= b_p + k\left(a_p.\sin \frac{2\pi p\Delta x}{L} + b_p.\cos \frac{2\pi p\Delta x}{L}\right) \end{aligned} \qquad (5.12)$$

Let us define

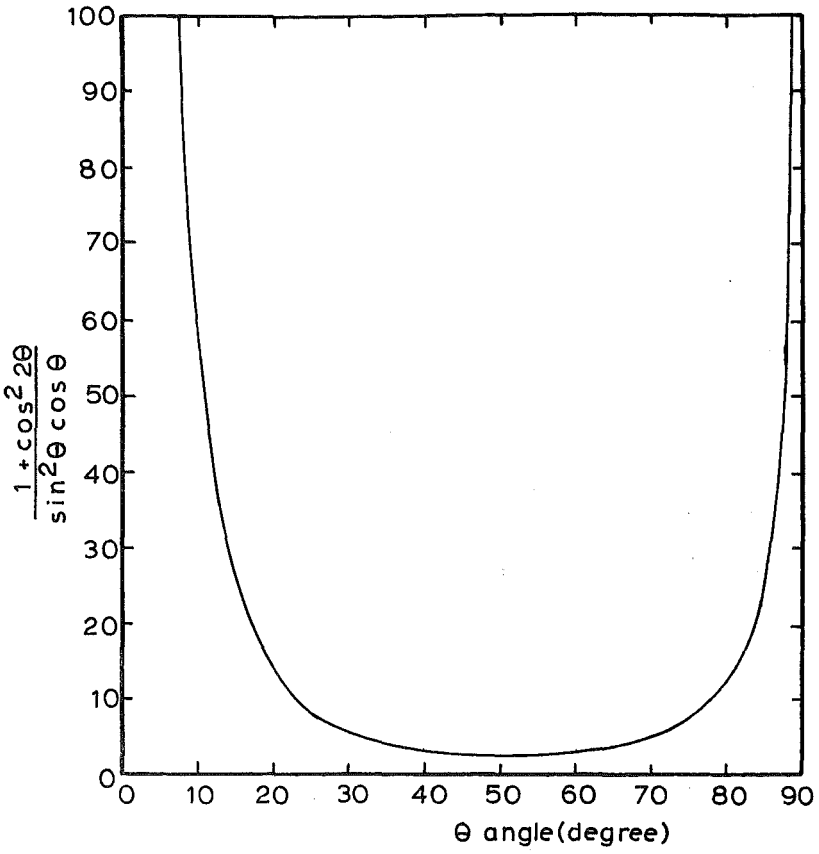

Fig.5.4 Lorentz-polarization factor.

$$C_p = 1 + k \cos \frac{2\pi p \Delta x}{L}$$

$$\text{and} \quad D_p = k \sin \frac{2\pi p \Delta x}{L} \tag{5.13}$$

Substituting equation (5.13) into (5.12), we have

$$a_p = \frac{A_p C_p + B_p D_p}{C_p^2 + D_p^2}$$

$$b_p = \frac{B_p C_p - A_p D_p}{C_p^2 + D_p^2} \tag{5.14}$$

Hence, when the Fourier coefficients of f(x) are obtained from the experimental Kα line profile, the Fourier coefficients of the $K\alpha_1$ component can be obtained from equation (5.14).

5.3.3 Correction of the $K\alpha_1$ Line Profile

Since the Lorentz-polarization factor[88] affects significantly the line breadth and peak position of line profiles in the far back reflection region ($2\theta \geqslant 140^{\circ}$) where Bragg reflections are used in X-ray stress analysis, correction for Lorentz-polarization factor is necessary. The Lorentz-polarization factor, LP, can be expressed as:

$$LP(x) = 1 + \cos^2 x/(\sin^2 x/2 \,.\, \cos\, x/2) \tag{5.15}$$

and its variation as a function of Bragg angle θ is shown in Fig. 5.4.

At the same time, correction for specimen absorption is necessary. The absorption factor A(x) as derived in Appendix 4 is expressed as follows:

$$A(x) = 1 - \tan\,(\psi_0 + \eta)\, \cot\, x/2 \tag{5.16}$$

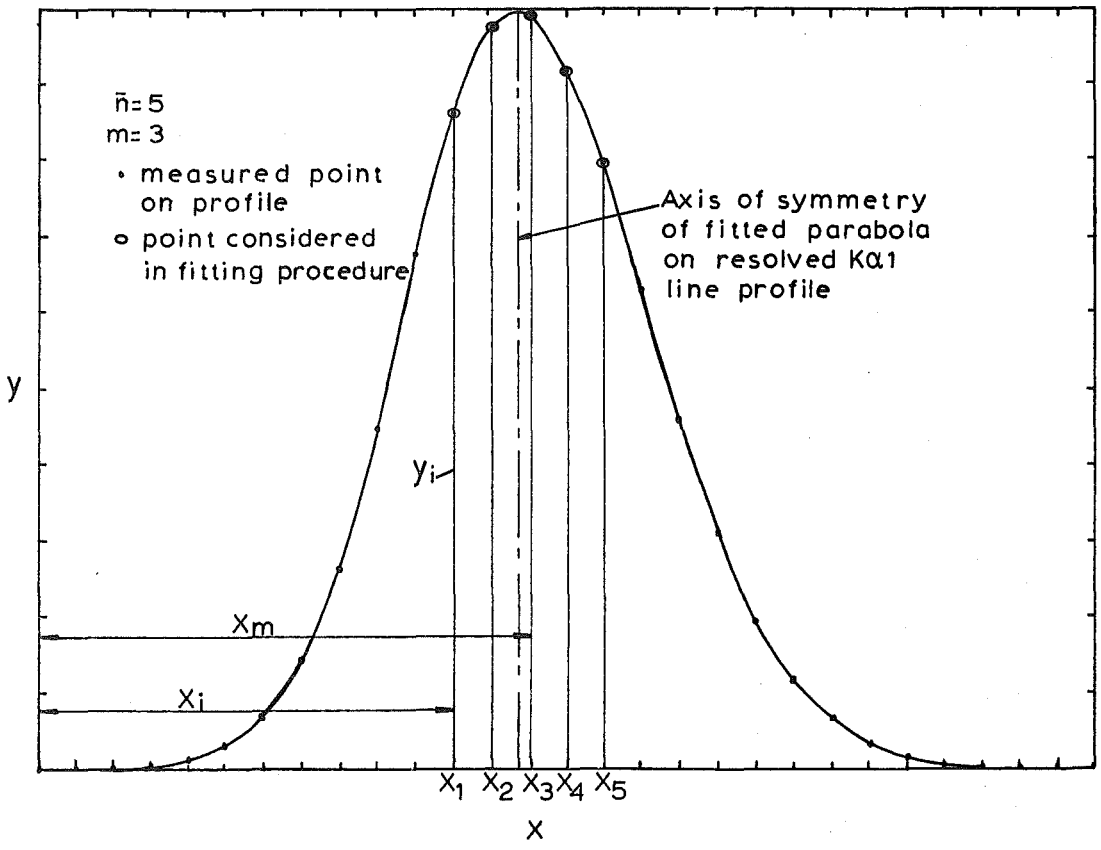

Fig.5·5 Least squares parabolic fit.

By combining these three physical aberration factors into one, LPA(x) say, the resolved $K\alpha_1$ line profile can be corrected as follows:

$$f_1(x)_{corrected} = f_1(x)/LPA(x) \tag{5.17}$$

where

$$LPA(x) = \frac{1 + \cos^2 x}{\sin^2 \frac{x}{2} \cdot \cos \frac{x}{2}} \left(1 - \tan(\psi_0+\eta) \cot \frac{x}{2}\right) \tag{5.18}$$

In fact, the observed $K\alpha$ line profile, f(x), can be corrected for LPA(x) prior to the separation process. Results showed the effect is the same as making the correction after the separation process.

5.3.4 Determination of the Peak Position of the $K\alpha_1$ Line Profile

With the resolved $K\alpha_1$ line profile, $f_1(x)$, the position of the $K\alpha_1$ peak can be determined by using a least squares parabolic curve fitting procedure. The procedure is described in Appendix 5 and the peak position X is expressed as:

$$X = x_m - \tfrac{1}{2} \frac{\begin{vmatrix} \Sigma(x_i-x_m)^4 & \Sigma y_i(x_i-x_m)^2 & \Sigma(x_i-x_m)^2 \\ \Sigma(x_i-x_m)^3 & \Sigma y_i(x_i-x_m) & \Sigma(x_i-x_m) \\ \Sigma(x_i-x_m)^2 & \Sigma y_i & 2m-1 \end{vmatrix}}{\begin{vmatrix} \Sigma y_i(x_i-x_m)^2 & \Sigma(x_i-x_m)^3 & \Sigma(x_i-x_m)^2 \\ \Sigma y_i(x_i-x_m) & \Sigma(x_i-x_m)^2 & \Sigma(x_i-x_m) \\ \Sigma y_i & \Sigma(x_i-x_m) & 2m-1 \end{vmatrix}} \tag{5.19}$$

where: x_m is the coordinate at the apparent peak position of the $K\alpha_1$ profile as scanned by the computer, x_i are equally spaced coordinates on each of x_m where their coordinates y_i are fitted with the parabolic curve,

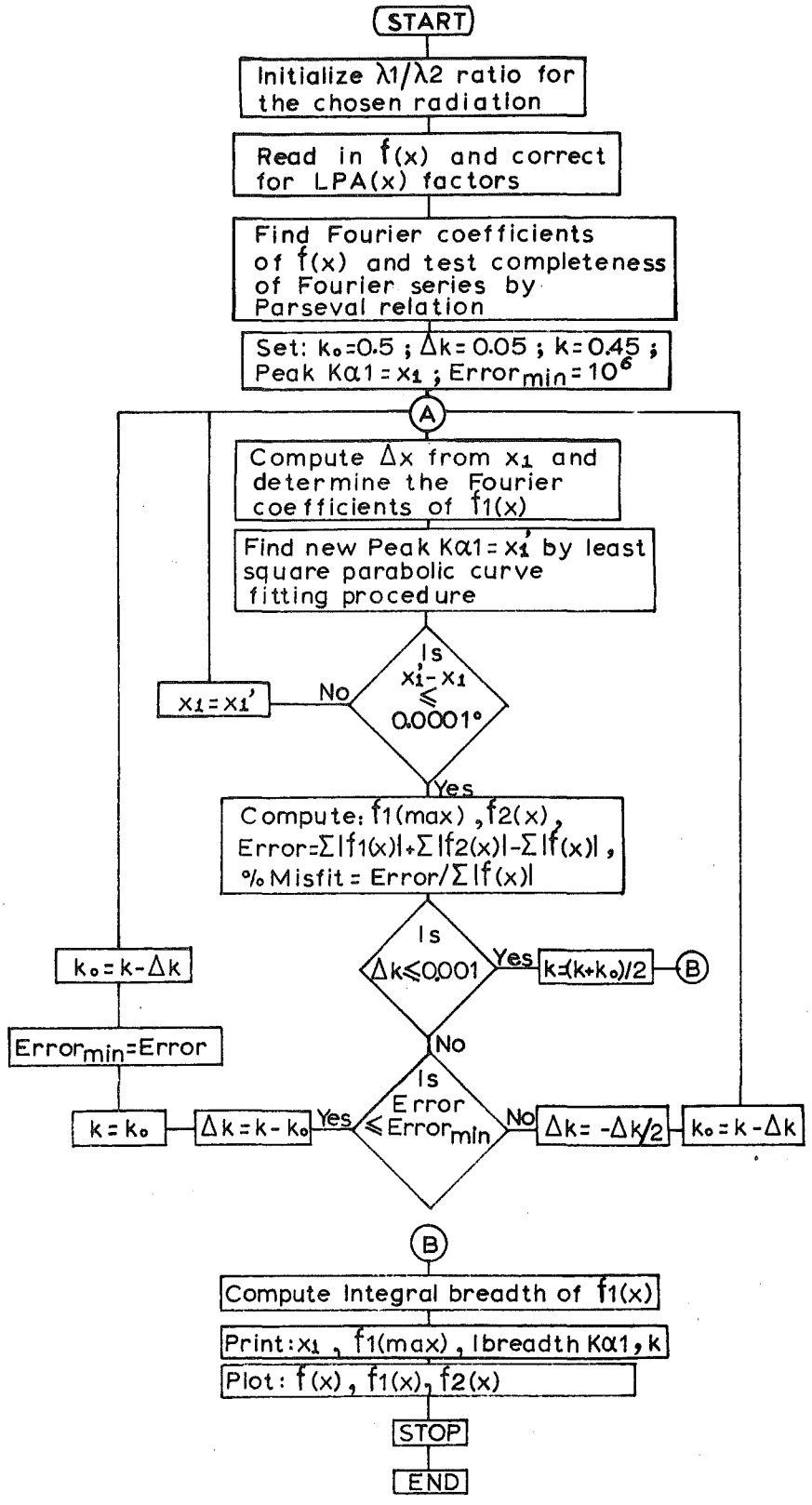

Fig.5·6 Flow chart for computer programme seeking optimum value of $K\alpha_2/K\alpha_1$ ratio.

and $m = (\tilde{n}+1)/2$, where $\tilde{n}$ is the number of points considered in the fitting procedure (see Fig. 5.5).

Wallace[83] suggests that the intensity values at these chosen points should not be less than 85% of the $K\alpha_1$ peak intensity.

5.3.5 Misfit Error

To check the correctness of the separation process, a quantity defined as the residue was used as θ check of misfit error. The residue was expressed as follows:

$$\text{Residue} = \Sigma(|f_1(x)|) + \Sigma(|f_2(x)|) - \Sigma|f(x)| \qquad (5.20)$$

It is a measure of the difference in bounded area about the datum line between the total bounded area of $f_1(x)$ and $f_2(x)$, and the bounded area of $f(x)$. If the separation of $f(x)$ into its component $f_1(x)$ and $f_2(x)$ has been performed correctly, then the residue should be ideally zero. (It should be noted that the differential increment dx has been removed in equation (5.20) because regular interval was chosen for the numerical solution). Otherwise, a positive finite value of residue exists when the separation was not done correctly, because $f(x)$ has a lower bound value than the separated $f_1(x)$ and $f_2(x)$. In other words, $f(x)$ was treated as the true observed intensity distribution and $f_1(x)$ and $f_2(x)$ are arbitrary separated components which are subjected to error due to the assumptions used in the separation process.

When using the computer programme to analyse some of the data obtained from tensile calibration experiment to obtain the X-ray elastic constants (see Tables 5-2(a),(c) in Appendix 6) the results show significant error of misfit; that is taking the assumption that $k = 0.5$. The plotted results of

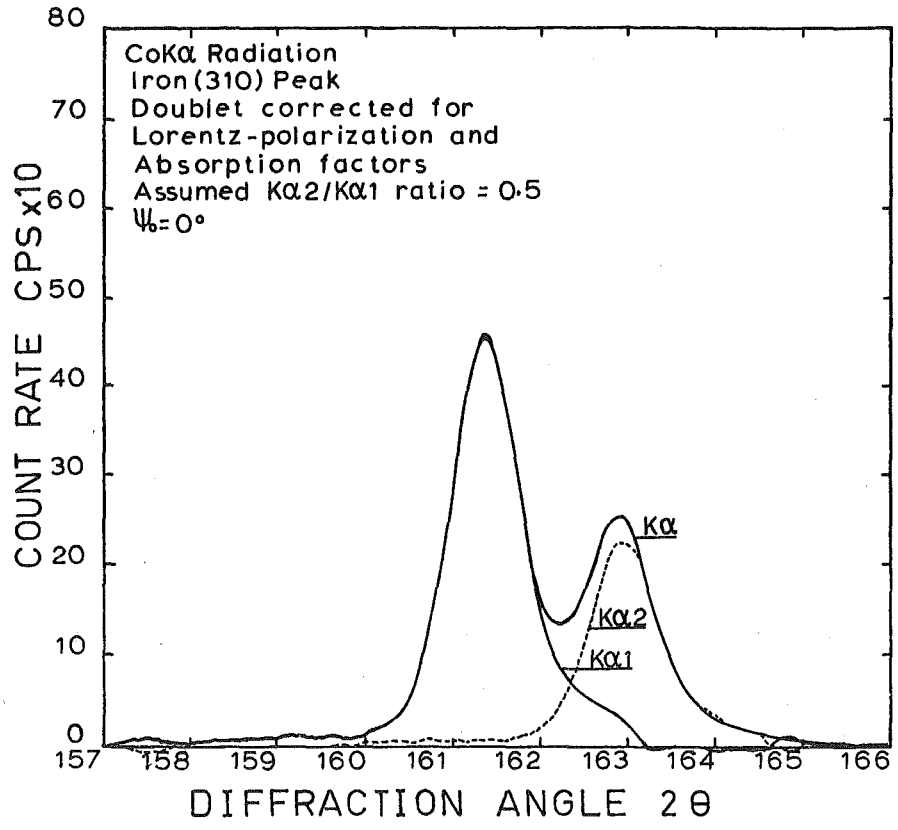

(a)

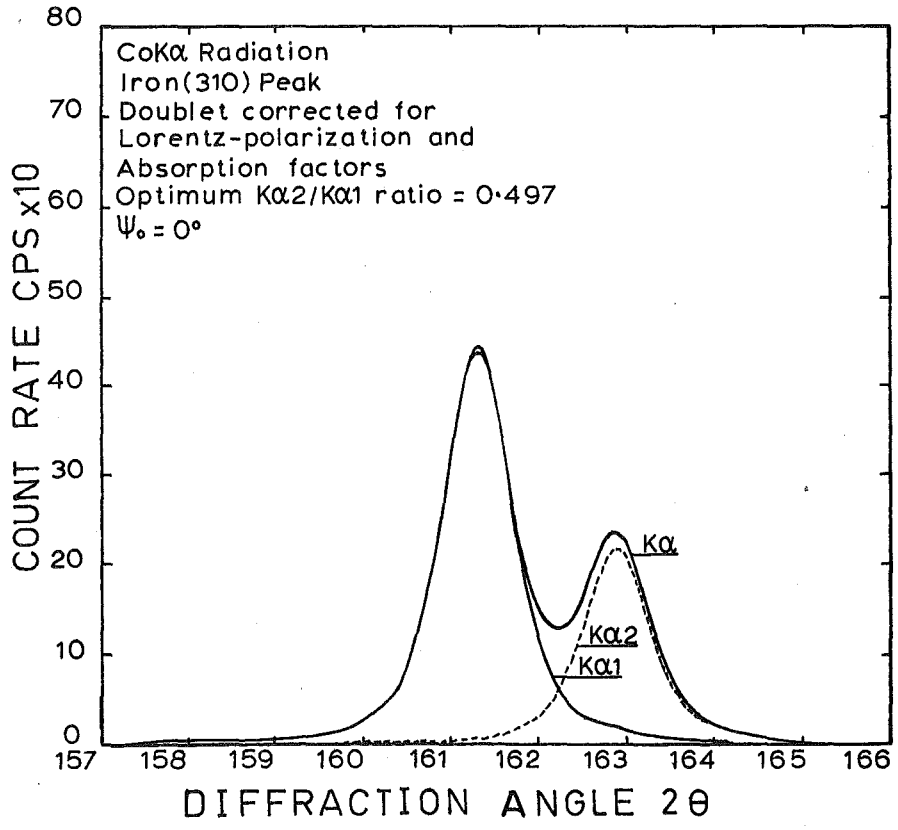

(b)

Fig.5·7 Analysed ditfraction line profiles.

the resolved $K\alpha_1$ line profile showed large fluctuations at the tail end of the line profile. It would appear that the assumed $I_{K\alpha_2(max)}/I_{K\alpha_1(max)}$ ratio of 0.5 was incorrect. Moreover, when k was assumed to take the value of 0.4 and 0.6 respectively, even larger fluctuations at the tail end of the resolved $K\alpha_1$ profile appeared. At this stage, it would clearly indicate that an optimised value of k must be sought so as to reduce the error of misfit and to approach the true condition existing in the set of data measured from the observed $K\alpha$ line profile.

5.4 Determination of the Optimum $K\alpha_2/K\alpha_1$ Ratio

Let us denote the ratio $I_{K\alpha_2(max)}/I_{K\alpha_1(max)}$ as $K\alpha_2/K\alpha_1$ ratio. The computer programme was modified so that it can seek the optimum $K\alpha_2/K\alpha_1$ ratio for each set of data presented to it for analysis. An iterative approach in predicting the optimum $K\alpha_2/K\alpha_1$ ratio was used. The programme will determine the changes in residue value with changes in $K\alpha_2/K\alpha_1$ ratio. Hence the $K\alpha_2/K\alpha_1$ ratio which gives the minimum residue is taken as the optimum value or the true value for the given set of data.

A flow chart for the programme is presented in Fig. 5.6 and to show the effectiveness of the programme, samples of plotted output for a given set of data which was analysed by taking a value of k = 0.5 and by taking an optimised value of k are presented in Fig. 5.7.

The main drawback when using the optimum $K\alpha_2/K\alpha_1$ ratio is computer process time. When using an assumed constant of $K\alpha_2/K\alpha_1$ ratio of 0.5, the process time for each set of data is about 30 seconds. This process time can be increased many-

TABLE 5-1

Actual values of the intensity functions $f(x)$, $f_1(x)$ and $f_2(x)$ along with synthesised values of the function $f_1(x)$.

x	Actual f(x)	Actual $f_1(x)$	Actual $f_2(x)$	Synthesised $f_1(x)$
0	0.0	0.0	0.0	-0.002
1	0.0	0.0	0.0	0.003
2	0.0	0.0	0.0	0.001
3	0.001	0.001	0.0	0.004
4	0.005	0.005	0.0	0.007
5	0.022	0.022	0.0	0.025
6	0.089	0.089	0.0	0.089
7	0.315	0.315	0.0	0.317
8	0.983	0.983	0.0	0.982
9	2.705	2.705	0.0	2.703
10	6.572	6.571	0.001	6.568
11	14.092	14.086	0.006	14.086
12	26.672	26.647	0.025	26.643
13	44.579	44.486	0.093	44.489
14	65.845	65.541	0.304	65.537
15	86.093	85.214	0.879	85.217
16	100.020	97.775	2.245	97.768
17	104.421	99.362	5.059	99.364
18	102.520	92.459	10.061	92.442
19	97.080	79.422	17.658	79.413
20	90.327	62.977	27.350	62.938
21	83.480	46.098	37.382	46.078
22	76.241	31.149	45.092	31.079
23	67.429	19.429	48.000	19.400
24	57.305	11.187	46.118	11.164
25	46.849	5.946	40.903	5.897
26	36.406	2.918	33.488	2.910
27	26.632	1.322	25.310	1.303
28	18.211	0.553	17.658	0.562
29	11.586	0 213	11.373	0.226
30	6.837	0.076	6.761	0.075
31	3.736	0.025	3.711	0.046
32	1.888	0.008	1.880	0.019
33	0.881	0.002	0.879	0.006
34	0.381	0.001	0.380	0.003
35	0.151	0.0	0.151	-0.008
36	0.056	0.0	0.056	0.0
37	0.019	0.0	0.019	-0.006
38	0.006	0.0	0.006	-0.009
39	0.002	0.0	0.002	-0.001
40	0.0	0.0	0.0	-0.002

fold when seeking an optimum for $K\alpha_2/K\alpha_1$ ratio which deviates significantly from the value of 0.5.

5.5 Test Programme

To illustrate the capability of the programme, a hypothetical experimental intensity distribution f(x) was generated from its components $f_1(x)$ and $f_2(x)$ where $f_1(x)$ and $f_2(x)$ are generated from a Gaussian function, $I = C \exp(-\gamma^2(x-x_0)^2)$ (see Fig. 5.8). Asymmetry in the profiles was deliberately introduced by taking $\gamma = 0.25$ and $\gamma = 0.20$ on the left and right side of the peak maximum of the component profiles respectively. The $f_{2(max)}/f_{1(max)}$ ratio was taken as 0.48 in this particular case and the maximum intensity of $f_1(x)$ is 100 unit. All numerical intensity values were calculated on a Hewlett-Packard calculator (model 9100A) and their values are presented in Table 5-1. The peak position of $f_1(x)$ was chosen at $X_0 =$ 16.6 and $f_2(x)$ peak position was at $X_0 = 23.0$ so that their separation, Δx, was 6.4. The total range of x considered was 40.

The synthesised values of $f_1(x)$ are shown in Table 5-1 along with the actual values. Other measures of $f_1(x)$ are also presented as follows:

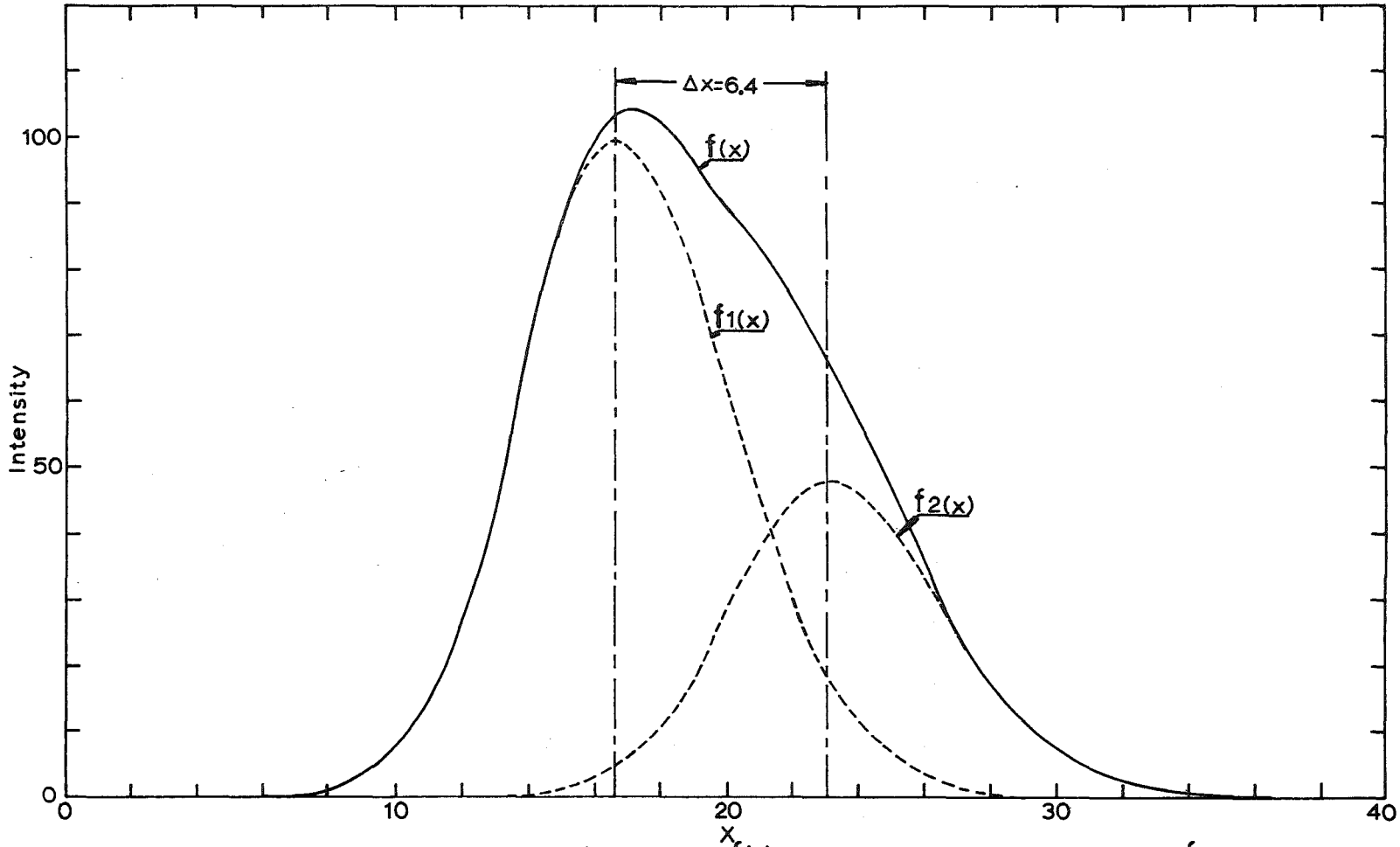

Fig. 5.8 A hypothetical diffraction line profile $f(x)$, along with its $\alpha 1$ component $f_1(x)$ and $\alpha 2$ component $f_2(x)$.

Parameter	Computed Value	Actual Value
$K\alpha_2/K\alpha_1$	0.4801	0.48
$I_{1(max)}$	99.9715	100.
Peak position of $f_1(x)$	16.6535	16.6000
Integral breadth of $f_1(x)$*	7.9756	7.9860
% misfit**	0.0071	0.0

* the integral breadth is defined as follows:

$$I_{breadth} = \text{Area under } f_1(x)/f_{1(max)}$$

** the % misfit = Residue/$\Sigma f(x)$.

5.6 Discussion

The capability of the present programme has been demonstrated in section 5.5. It shows that it is possible to separate a composite $K\alpha_1\alpha_2$ experimental diffraction profile into its $K\alpha_1$ and $K\alpha_2$ components without prior assumption of a $K\alpha_2/K\alpha_1$ ratio. Diffraction line profiles of any shape may be resolved into their components using the present method. However, true diffraction line profiles are difficult to obtain because observed experimental line profiles are displaced and broadened by physical and geometrical aberrations[58].

In general, Stokes method is used for shape analysis[70] and the present modified Rachinger method for peak position determination. However, in the present work, lack of high temperature vacuum annealing facilities prevents the author from using the Stokes method. Recapitulating on the objectives of the present analysis, it is the measure of the peak angle of the resolved $K\alpha_1$ line profile which is required for the double-exposure method of stress measurement. A

measure of the $K\alpha_1$ line width can be obtained by the present programme, but it must be noted that the LPA correction made on the line profile is only a partial correction. Other aberration functions have been described in text[58], but it can vary with ditferent instruments.

When the present work on optimising the $K\alpha_2/K\alpha_1$ ratio was completed, literature by Taira et al.[86] from Japan showed similar work has been attempted. From Taira et al. papers, another reference given showed that Gangulee[87] has used the Fourier method and has attempted the optimum $K\alpha_2/K\alpha_1$ ratio solution. Taira et al. and Gangulee used similar test programmes as described in section 5.5, and have obtained satisfactory results.

5.7 Statistical Investigation of Sampling and Analysing Methods

5.7.1 Introduction

In this section of the work, the objectives were to establish the method of sampling of the chart outputs and the difference in precision of the two proposed methods of separation of the composite Kα line profile into its components.

The problems of acquiring data from experimental diffraction profiles as recorded on paper and feeding this data into a digital computer for analysis of the peak position and integral breadth of the resolved $K\alpha_1$ line profile were studied. With the present computer programme, it is possible to feed data taken at regular intervals of arbitrary size from the experimental diffraction intensity patterns. In view

TABLE 5-3: Data for Analysis of Variance

Peak angle of sample (minus 160°)

Batch	SAMPLE 1		SAMPLE 2	
	Method A	Method B	Method A	Method B
1	1.0429	1.0395	1.0501	1.0470
2	1.2293	1.2277	1.2239	1.2223
3	1.0579	1.0522	1.0531	1.0491
4	1.1849	1.1826	1.1800	1.1777
5	1.1224	1.1180	1.1236	1.1192
6	1.1823	1.1795	1.1828	1.1802
7	1.1318	1.1254	1.1322	1.1244
8	1.1303	1.1287	1.1257	1.1249
9	1.1486	1.1422	1.1497	1.1443
10	1.0699	1.0633	1.0782	1.0744
11	1.1936	1.1870	1.1871	1.1821
12	1.0459	1.0440	1.0351	1.0337
13	1.1939	1.1860	1.1844	1.1762
14	0.9864	0.9842	1.0011	0.9994
Total	15.7201	15.6603	15.7070	15.6549

TABLE 5-4: Analysis of Variance

Source of Variation	Sum of Squares	Degree of Freedom	Mean Squares	Expectation of Mean Squares
Between batches	0.25366674	13	0.01951283	$\bar{\sigma}_o^2 + 2\bar{\sigma}_1^2 + \bar{\sigma}_2^2 + B$
Bias between methods	0.00022360	1	0.00022360	$\bar{\sigma}_o^2 + \bar{\sigma}_2^2 + Q$
Interaction of batches and methods	0.00006365	13	0.00000490	$\bar{\sigma}_o^2 + \bar{\sigma}_2^2$
Between samples	0.00069939	14	0.00004996	$\bar{\sigma}_o^2 + 2\bar{\sigma}_1^2$
Analytical error (=remainder)	0.00000443	14	0.00000032	$\bar{\sigma}_o^2$
Total	0.25465781	55		

$\bar{\sigma}_o^2 = 0.00000032$ $\qquad$ $\bar{\sigma}_o = 0.00056569°$

$\bar{\sigma}_1^2 = 0.00002552$ $\qquad$ $\bar{\sigma}_1 = 0.00505124°$

$\bar{\sigma}_2^2 = 0.00000482$ $\qquad$ $\bar{\sigma}_2 = 0.00219545°$

$Q = 0.00021246$

$B = 0.01686347$ $\qquad$ $\sqrt{B} = 0.12985942°$

$D^2 = Q/14 = 0.00001518$ $\qquad$ $D = 0.00389560°$

of the large quantity of charts to be analysed in subsequent measurements of residual stresses in welded plates, a method involving the minimum number of intervals at which data are taken and still giving reproducible results was sought.

5.7.2 Procedure

In this work, chart outputs for an experiment in determining the X-ray elastic constants were used for analysis. These analysed data are presented in Table 5.2, (see Appendix 6). For each measured diffraction intensity pattern, two samples of data were taken, one at regular intervals of 0.1 deg. and the other at 0.25 deg. Both samples of data were analysed by using an assumed $K\alpha_2/K\alpha_1$ ratio of 0.5 and by using an optimised value of $K\alpha_2/K\alpha_1$ ratio as computed for each set of data.

Let us define the following:

Sample 1: data acquired at 0.25 deg. intervals

Sample 2: data acquired at 0.10 deg. intervals

Method A: Fourier method using an optimised $K\alpha_2/K\alpha_1$ ratio

Method B: Fourier method using an assumed $K\alpha_2/K\alpha_1$ ratio of 0.5.

The analysed results of the peak position of the $K\alpha_1$ line profiles from the various samples and methods of analysis are tabulated in Table 5.3. The data was treated by analysis of variance method, leading to the following table of analysis of variance as shown in Table 5.4. Actual computations involved in the analysis of variance are too lengthy to be presented, however, it follows an example presented explicitly by Davies[91]. Notations used here follow the same as used by Davies.

5.7.3 Results

From the analysis of variance the following estimates were obtained:

Variance	Standard error
$\tilde{\sigma}_0^2 = 0.00000032$	$\tilde{\sigma}_0 = 0.00056569°$
$\tilde{\sigma}_1^2 = 0.00002552$	$\tilde{\sigma}_1 = 0.00505124°$
$\tilde{\sigma}_2^2 = 0.00000482$	$\tilde{\sigma}_2 = 0.00219545°$

where: $\tilde{\sigma}_0^2$ is the reproducibility variance which was assumed to be the same for both methods,

$\tilde{\sigma}_1^2$ is the sampling error variance,

$\tilde{\sigma}_2^2$ is a measure of the variance represented by the variability in bias in method B because method A was assumed to be free of bias.

The sampling standard error of 0.005° is not significant when compared with the readability of the goniometer which is 0.01 deg. However, this sampling error actually represents the difference between samples of data taken at 0.10 deg. intervals and at 0.25 deg. intervals. The small standard error in reproducibility of both methods shows that the methods can yield closely concordant results in replicate analyses. The small standard error in variability of bias in method B shows that the bias between method A and method B varies insignificantly when compared to the readability of the goniometer of 0.01 deg. However, the constant bias between method A and method B is about 0.004° as represented by $\sqrt{\frac{Q}{14}}$ in Table 5.4.

5.7.4 Conclusion

It can be concluded that there is a constant bias between method A and method B. This is obvious in view of the assumptions used in method A and method B. The variation in bias between both methods is about half the constant bias. The sampling error is not significant from the viewpoint that accuracy of data taken from the chart output is not expected to be better than ±0.01 deg. This is mainly due to errors in data being evenly distributed over the profile. Last of all, the reproducibility of both methods is good. Therefore, by taking data at 0.25 deg. intervals, the peak angle as analysed by method B; that is assuming a constant $K\alpha_2/K\alpha_1$ value of 0.5, is consistent enough for the present work where relative changes in peak angle are used in the double-exposure method. Hence much computer process time and manual efforts can be saved by taking this option. Moreover, it should be noted that the results from the particular method of analysis can at most only be as good as the experimental data.

5.8 Comparison of Peak Angles Determined by Computer Method and Graphical Methods

In Appendix 7, two sets of graphical outputs were analysed by computer method and graphical methods. In one set of outputs, the diffraction profiles were well resolved and the line breadths were uniform. In the other set of outputs, some of the diffraction profiles were unresolved and the line breadths were not uniform.

The results from this study showed that under the condition where the diffraction profiles were well resolved; that is the $K\alpha_1$ and $K\alpha_2$ peaks were resolved, the graphical methods and computer method both showed reasonable agreement.

However, under the conditions where the diffraction profiles were broad and the $K\alpha_1$ and $K\alpha_2$ peaks were unresolved, uncertainties were experienced with the graphical method. In some instances, significant differences were found between the two methods. Hence there is much to recommend the computer method when determining the peak angles from diffused diffraction profiles. When diffraction profiles are well resolved and the sides of the diffraction profiles are linear, the triangular method can be used advantageously because of the saving in effort in preparing data for computer analysis.

To be consistent, all the data in the present work was analysed by the computer method as described in section 5.3.

CHAPTER 6

EFFECTS OF SURFACE PREPARATION AND PREFERRED ORIENTATION ON X-RAY STRESS MEASUREMENTS

6.1 Introduction

This section describes some of the effects of surface preparation on (a) surface layer of a polycrystalline material; (b) residual stress measurement; and (c) X-ray elastic constants. Further on, the effect of preferred orientation on the X-ray elastic constants was investigated.

The nature of mechanically polished metal surfaces and the deformation produced during abrasion and machining have been studied by Samuels et al.[92]. It is generally accepted that mechanical preparation leads to a severely deformed zone near the surface whereas electropolishing will remove surface metal without deforming the surface revealed. This deformed zone produced by abrasion or machining has different properties to those of the bulk metal. Hence results obtained on mechanically polished surfaces are not characteristic of the bulk metal. In view of the aim of present study; that is measuring the residual stresses of weldments, it is imperative that the X-ray measurements taken on the surface of the welded plates are characteristic of the bulk metal. Hence, electropolishing is required to remove existing deformed layer and surface blemishes on the welded plate prior to X-ray measurements.

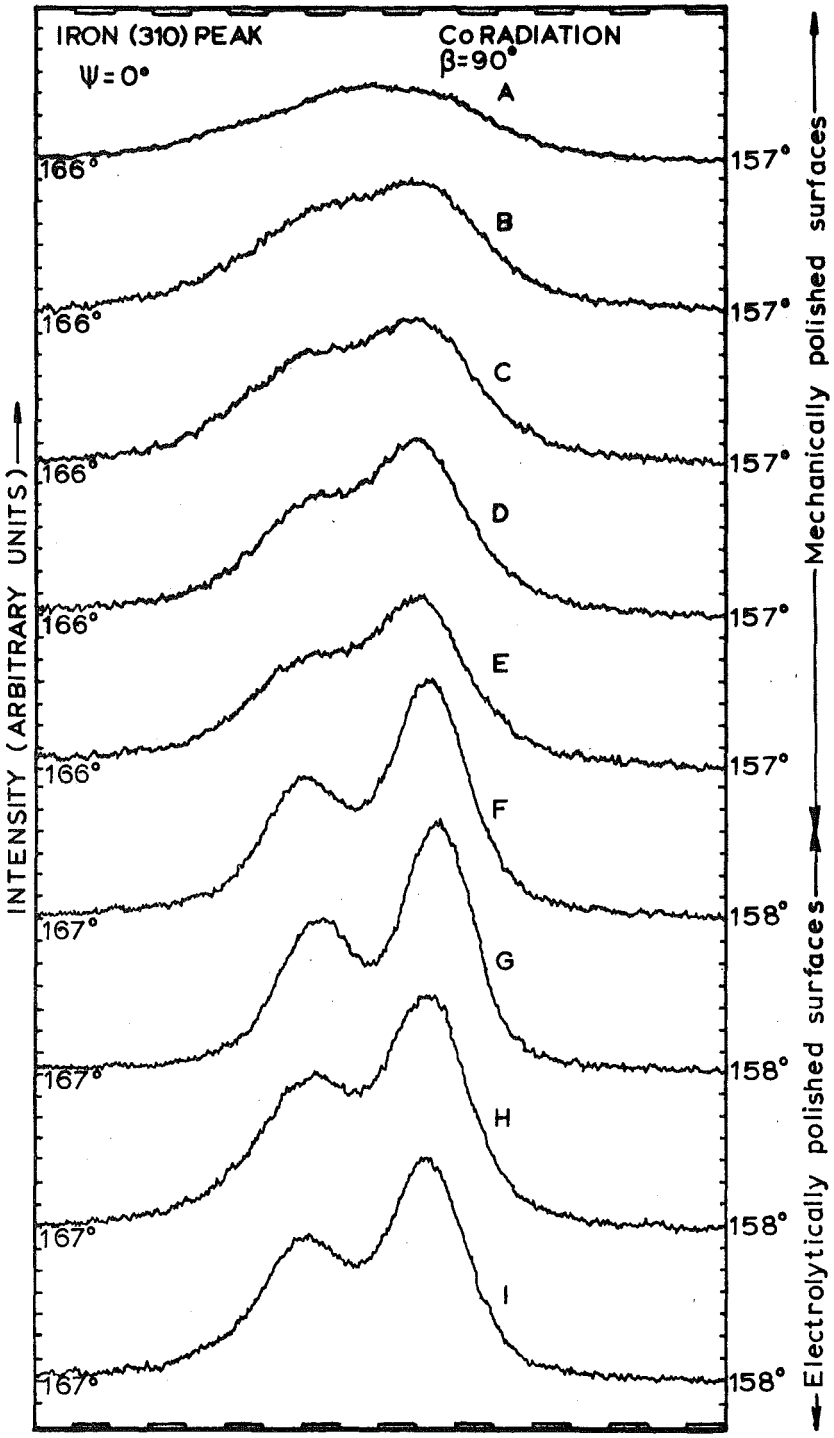

Initial specimen machine surface ground t=.124"

A. M/C ground t=.124"; B. Abraded with 240paper t=.123";

C. Abraded with 640paper t=.122"; D. Abraded with emery paper followed by lap polishing with fine diamond dust t=.120"; E. As in case D t=.118";

F. Electropolished t=.116"; G. Electropolished t=.114";

H. A similar specimen as in A-G, Electropolished to remove .002" from M/C ground surface; I. As in case H, Electropolished to remove .004" from M/C ground surface.

Fig.6·1 Variation of line profiles with surface preparation.

6.2 Effect of Surface Preparation on the Surface Layer of a Polycrystalline Material

The variation of residual stress and line width caused by surface preparation was studied on samples which were recovery annealed at 650°C for ½ hr. prior to surface grinding. Various methods of polishing were used and X-ray measurements were taken from the immediate exposed surface annealed by each method of preparation.

The results of the X-ray measurements are shown in Table 6-1 (see Appendix 8). The effect of surface preparation on the experimental line profiles is shown in Fig. 6.1. The variation of residual stress and line width with depth is shown in Fig. 6.2. The appropriate X-ray stress constant as obtained from calibration (section 6.4.3) was used in the stress calculation.

6.2.1 Conclusion

Since X-ray stress measurements are sensitive to surface effects, the preparation of specimen-surface is important. Especially when the surface has been previously machined, the deformed layer produces very diffused reflection as evidenced in Fig. 6.1. The diffused intensity pattern makes peak measurements difficult and likely to be subjected to inaccuracies.

Mechanical polishing was shown to be unsatisfactory in removing the deformed layer because in itself, mechanical polishing did produce a deformed layer, but the deformed layer produced is not as thick as that produced in machining[92]. A combination of mechanical polishing and etching with nital solution has been suggested, but the metal removal rate is slow. However, electropolishing (see Appendix 3) did improve

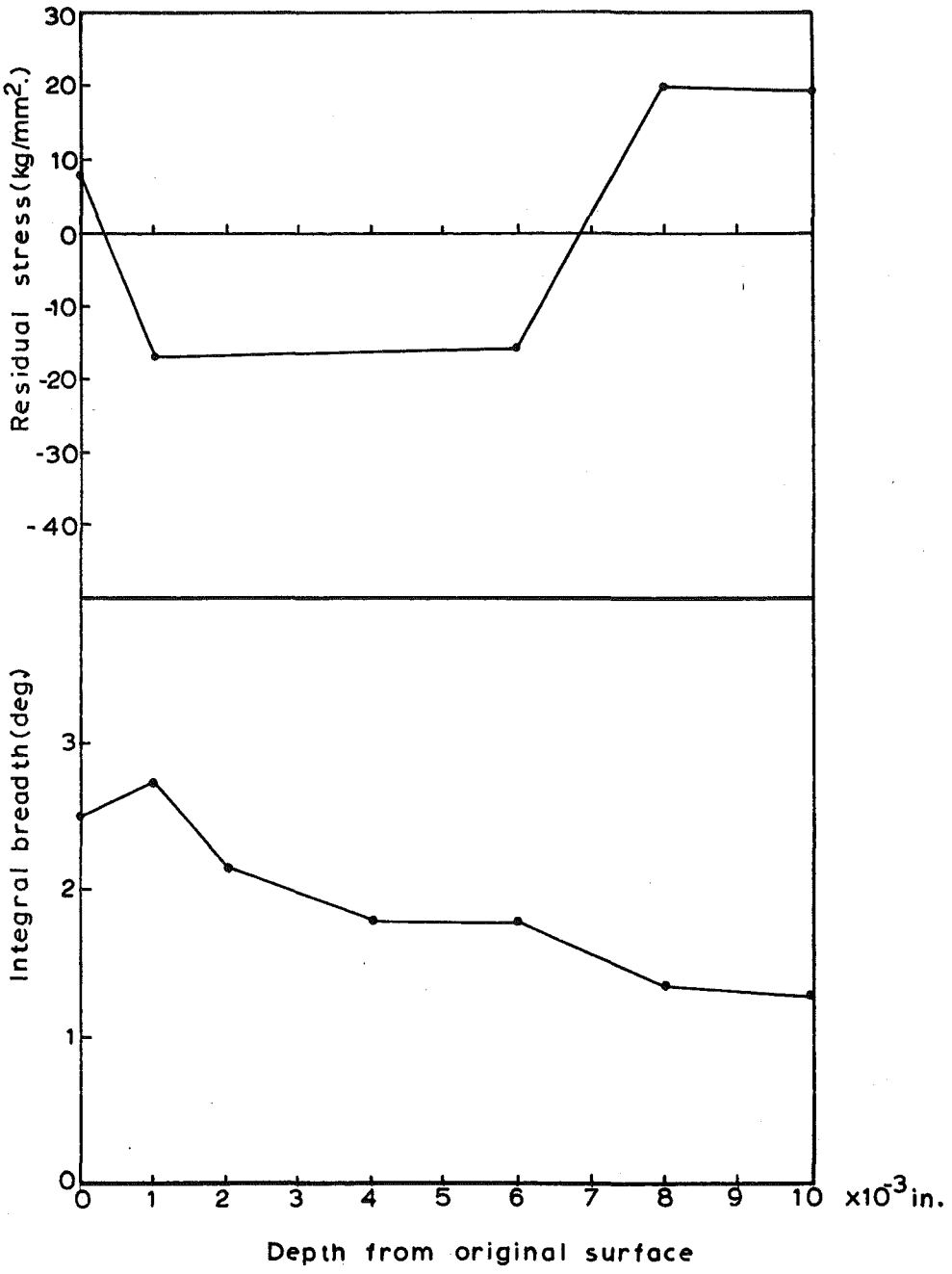

Fig. 6·2 Variation of residual stress and line breadth with depth.

reflection from the electropolished surface. This is due to strain-free methods of metal removal characteristic of the electropolishing method.

The variation of residual stress induced by the various methods of surface preparation (Fig. 6.2) confirms that mechanical polishing did induce compressive residual stress in the surface layer. However, it is interesting to note from the present analysis that surface grinding induces a moderate tensile residual stress as opposed to the high compressive stress found by Hayashi[69] and French et al.[27]. This could be due to error in peak measurements because the intensity pattern obtained in the machine ground condition is very diffused. Hence emphasis must be placed on getting sharp reflections so as to improve the accuracies of the X-ray stress measurements. The broadening of the line width is due to the deformed layer produced in mechanical abrasion and machining processes. From the experiment, it is evident that a single electropolishing operation is sufficient to remove the deformed layer due to surface grinding (Fig. 6.1).

6.3 Effect of Surface Preparation on X-ray Stress Measurements

Since the effective depth of penetration of the CoKα radiation in iron is small (about 10^{-4} inch), specimen-surface preparation is important. The removal of deformed layer due to previous treatment and oxide films or scales formed during hot-rolling or the recovery annealing process is essential.

In this investigation, two methods of surface preparation were studied. In the first method, the surface was abraded with medium emery paper and then etched with 10% Nital. The second method was by electropolishing the surface concerned.

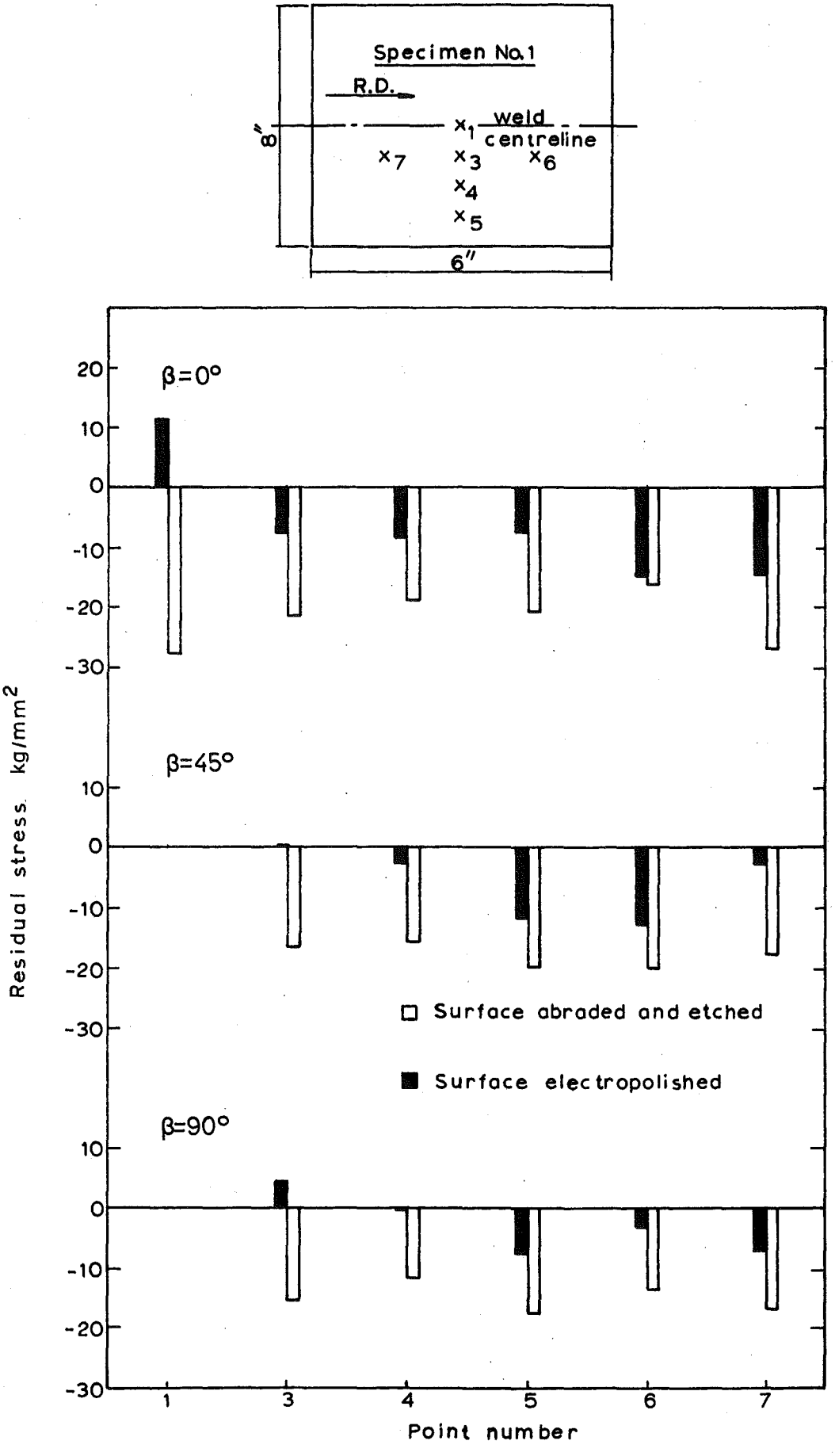

Fig.6·3 Effect of surface preparation on stress values.

The electropolishing procedure is described in Appendix 3.

A welded specimen was used as a sample with residual stresses present in it. In this case, specimen No. 1 (see Table 3-5) was used. Two plates 6" long x 4" wide x 3/8" thick with single-vee edge preparation was welded by the short-circuiting arc technique. The results of the X-ray stress measurements from both methods of surface preparation are shown in Fig. 6.3.

6.3.1 Discussion and Conclusion

From the results presented in Fig. 6.3 it can be seen that high compressive residual stresses were present in the surfaces exposed by abrasion and etching. In contrast, the residual stresses were of lower magnitude after electropolishing. In fact, there is a reversal from compressive to tensile residual stress at point 3 (Fig. 6.3). It would appear that abrading followed by etching with 10% Nital solution is insufficient to remove surface effects such as deformed layer due to previous working. The abrasion process in itself produces a thin layer of deformed metal beneath the surface and thus contributes to the high compressive residual stresses found in the first case.

The etching produced by 10% Nital solution can be considered to be insufficiently vigorous. Stronger acid must be used. However, electropolishing did provide a rapid method of strain-free metal removal. Many investigators[27,69] have used the electropolishing method of removing deformed metals due to machining of the specimens, but small specimens were involved in these cases. In the present work, larger specimens are involved. The largest welded plate was 14" long x 8" wide and the author found difficulty in obtaining suitable form of

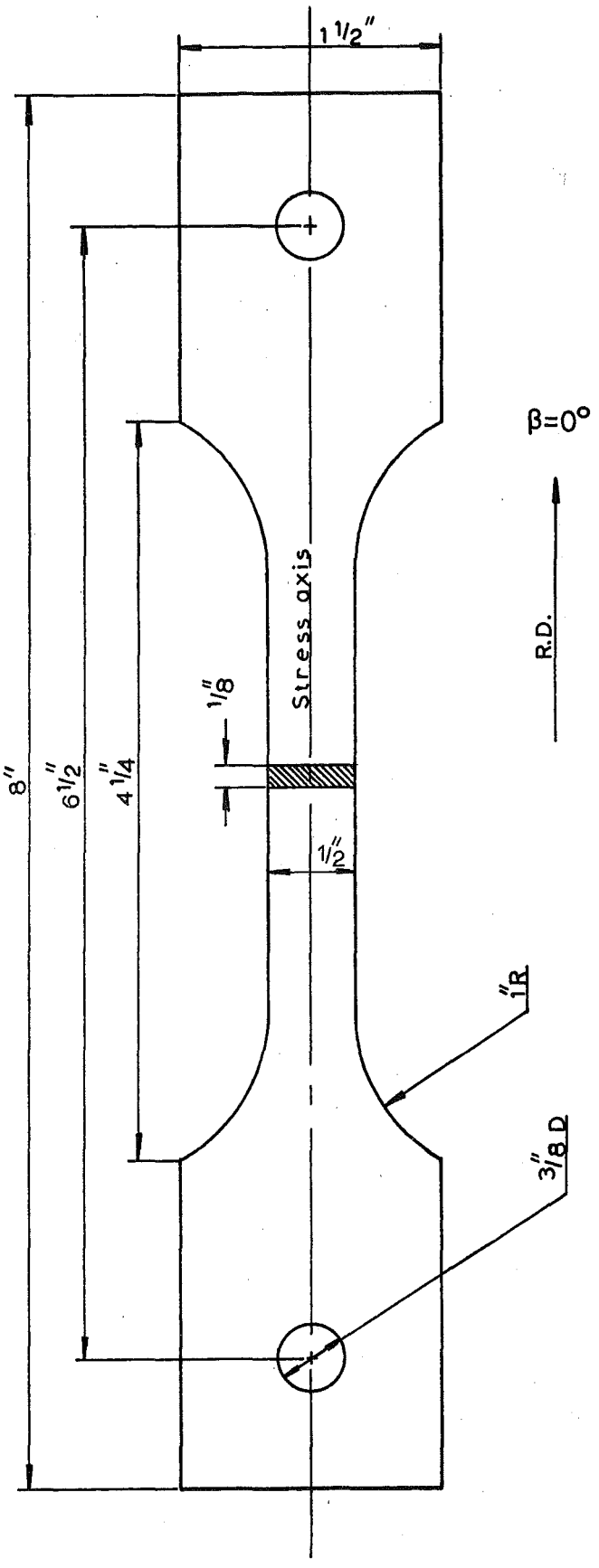

Fig.6·4 Tensile specimen for X-ray calibration.

electropolishing equipment which could accommodate specimens of this size. Anyway, these problems are discussed in Appendix 3.

It must be noted that no compensation was allowed for the relief of stress due to metal removal in this study. What X-ray stress measurements have revealed following the electropolishing process is the apparent stress in the exposed surface. The true stress at that level of depth is changed following metal removal to exposere the surrace at that depth. However, the thickness of metal removed in the present procedure is small (0.002") as compared to the thickness (0.375") of the specimen. Hence, changes in true stress in the bulk material are insignificant. Moreover, the changes in stress value as revealed in this study are due to the removal of deformed layer which exhibits high stress gradient near the surface. Many studies have revealed high stress gradient in the surface layer due to machining processes[69,27], heat treatment processes[19] and mechanical treatment[27]. These stresses are not of interest in the present study. Only the residual stresses in the bulk material are investigated. In-depth variation of stress such as those existing in triaxial stress system was not considered because many results[8,53] have shown that plates of thickness less than ½ inch exhibit biaxial residual stress system after welding. However, in cases where the initial stress distribution is required, the underlying residual stress profile can be calculated using the methods of Moore and Evans[93].

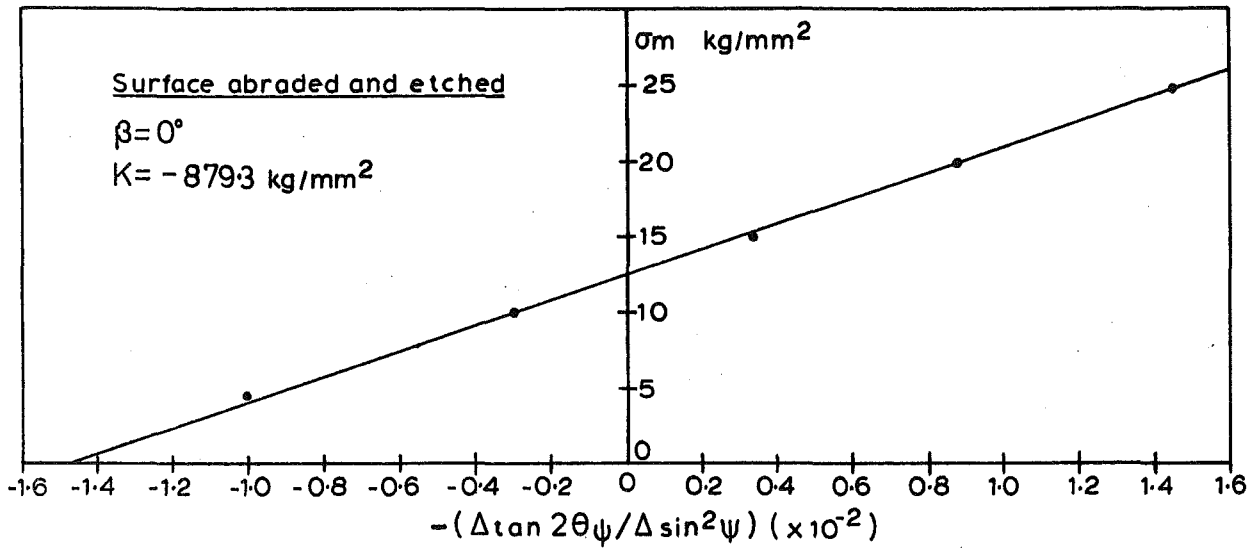

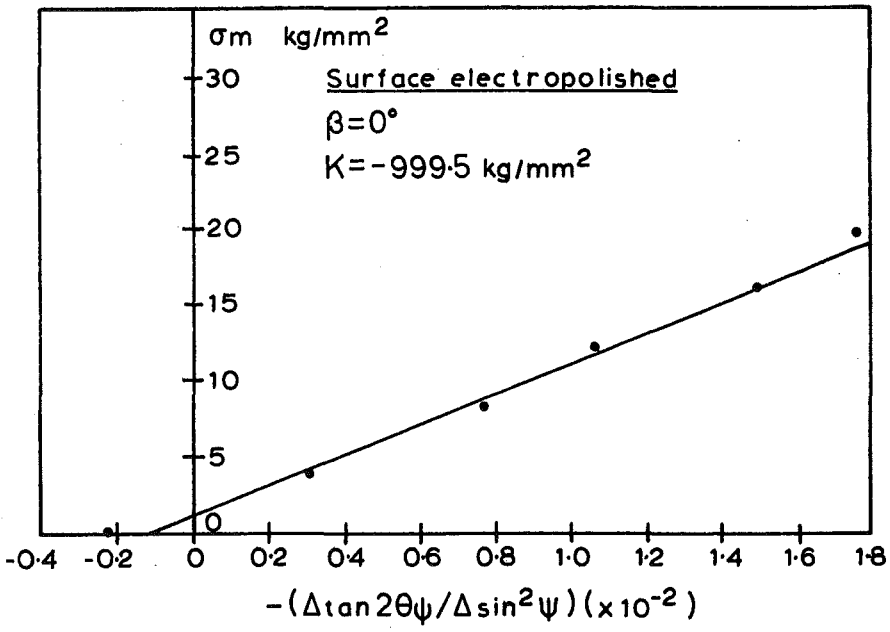

Fig. 6.5 σ_m vs $-\Delta \tan 2\theta_\psi / \Delta \sin^2\psi$ (Effect of surface preparation on X-ray stress constants).

6.4 Effect of Surface Preparation on X-Ray Elastic Constants

6.4.1 Introduction

In X-ray stress measurements, the appropriate value of the stress constant K must be used for the calculation of stress value (c.f. equation (4.18)). The stress constant K as given by equation (4.19) is:

$$K = -\frac{E}{1+\nu} \cdot \cot\theta_0 \frac{(1 - 2\sin^2\theta_0)^2}{2}$$

The value of K can be obtained by calibration where step loadings are applied to a specimen in uniaxial tension and X-ray measurements taken for two or more values of ψ at each load. From the slope of $\sigma_m/(\Delta \tan 2\theta_\psi/\Delta \sin^2\psi)$ (where σ_m is the applied stress), K is obtained. Loading within the elastic range is normally used and the X-ray measurements must be taken from specimen surface which is representative of the material in which subsequent X-ray stress measurements are to be taken.

6.4.2 Experimental Procedure

In this investigation, tensile specimens of the dimensions as shown in Fig. 6.4 were used. The specimens have been previously machined and subsequently recovery annealed at 650°C for 1½ hours. Two methods of surface preparation were investigated. The first method was to abrade the surface and then etch with 10% Nital, and the second method by electropolishing. A Hounsfield tensometer was used to strain the specimen (see Fig. 4.4) in uniaxial tension. The results of the X-ray measurements are shown in Table 6-2(a),(b) (see Appendix 9). The results of σ_m versus $-\Delta \tan 2\theta_\psi/\Delta \sin^2\psi$ are shown in Fig. 6.5.

6.4.3 Discussion and Conclusion

The good linearity between the applied stress σ_m and the slope of $\Delta \tan 2\theta_\psi / \Delta \sin^2\psi$ shows accurate measurement. Actual calculations of the X-ray elastic constants are shown in Appendix 9 which serves as a sample calculation for all subsequent computations.

From the abraded and etched conditions, the following results were obtained:

Young's modulus	E	= 14802 kg/mm^2
Poisson's ratio	ν	= 0.25
X-ray stress constant	K	= -879.3 kg/mm^2

From the electropolished condition, the following results were obtained:

Young's modulus	E	= 17912 kg/mm^2
Poisson's ratio	ν	= 0.32
X-ray stress constant	K	= -999.5 kg/mm^2.

Hence it can be seen that the behaviour of the surface layer affects the macroscopic value of the X-ray elastic constants. Even though the bulk material and the stress axis which is parallel to the rolling direction, are the same in both specimens, it is the behaviour of the surface layer during calibration which is measured.

Therefore the X-ray elastic constants obtained in the electro-polished condition are taken as representative values of the material in the direction parallel to rolling direction where $\beta = 0^\circ$.

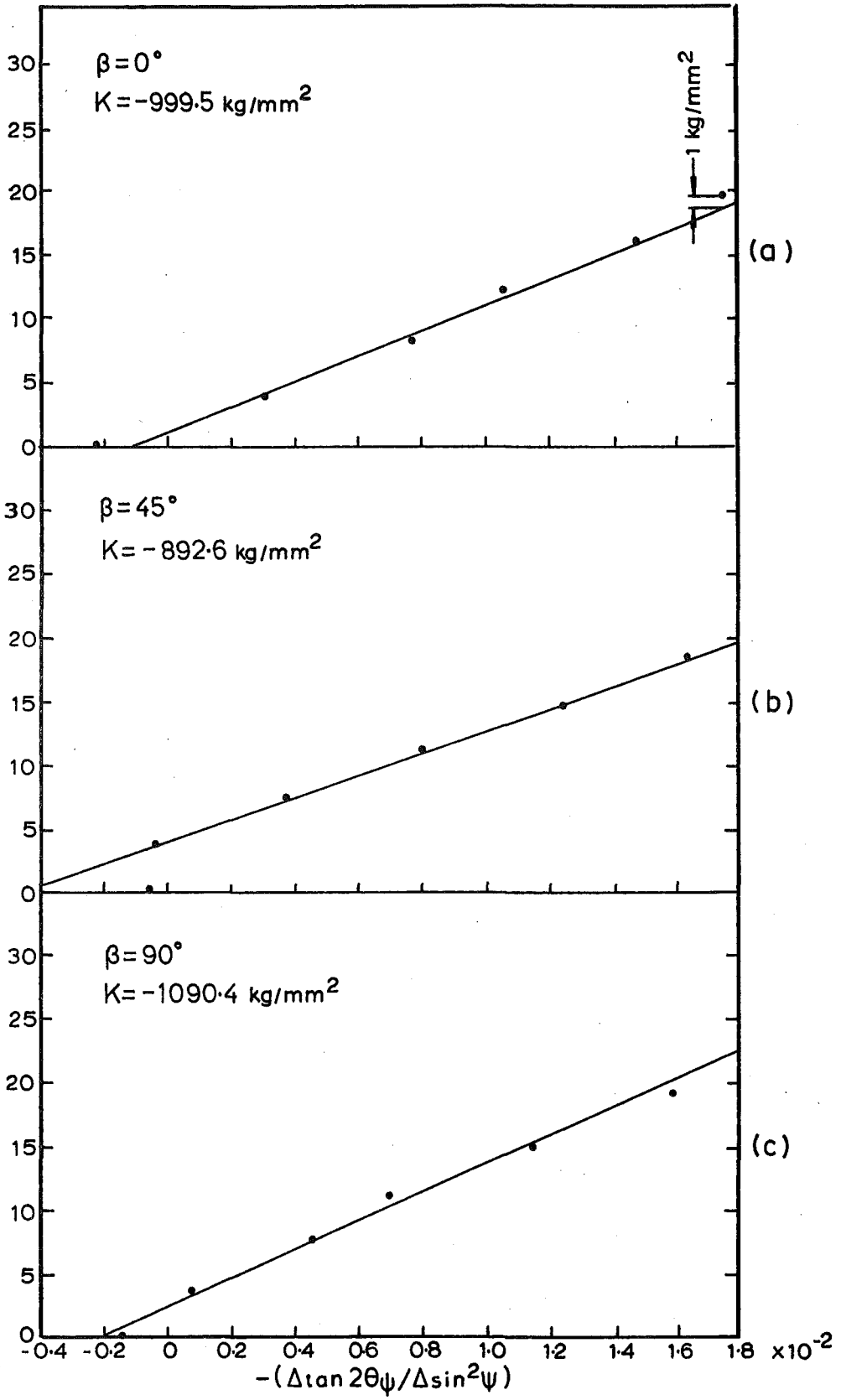

Fig.6·6 σm vs $-\Delta\tan 2\theta_\psi/\Delta\sin^2\psi$ (Effect of preferred orientation on X-ray stress constants).

6.5 The Effect of Preferred Orientation on X-ray Elastic Constants

6.5.1 Introduction

The main features of anisotropy of a polycrystalline aggregate are the directional variation of strength, ductility, elastic moduli and other mechanical properties. The directional properties in polycrystalline metals are attributable to the effect of preferred orientation and anisotropic properties of single crystals.

Anisotropy was found in the hot-rolled steel plates used in the present study. The strength and ductility of the metal were found to vary with direction of measurement (see section 3.4.5). Back reflection diffraction patterns also indicated the presence of small degrees of preferred orientations (see section 3.4). Even after the recovery annealing, the initial crystallographic texture remains barely altered. In view of the presence of preferred orientations and the high anisotropy of simple crystals of iron, the X-ray elastic constants are expected to vary with direction of measurement.

The variation of X-ray elastic moduli has been confirmed by the results of Rutledge[26] and Donachie and Norton[94]. Hayashi[69] has found that the X-ray elastic constants of steel are affected by grain size, carbon content, mechanical fibering, preferred orientations and anisotropy of single crystals of iron. In view of the large variety of factors affecting the X-ray elastic constants, it would be best to obtain the actual X-ray elastic constants by calibration with specimens of identical condition and composition to that prevailing in the material examined under X-ray stress analysis.

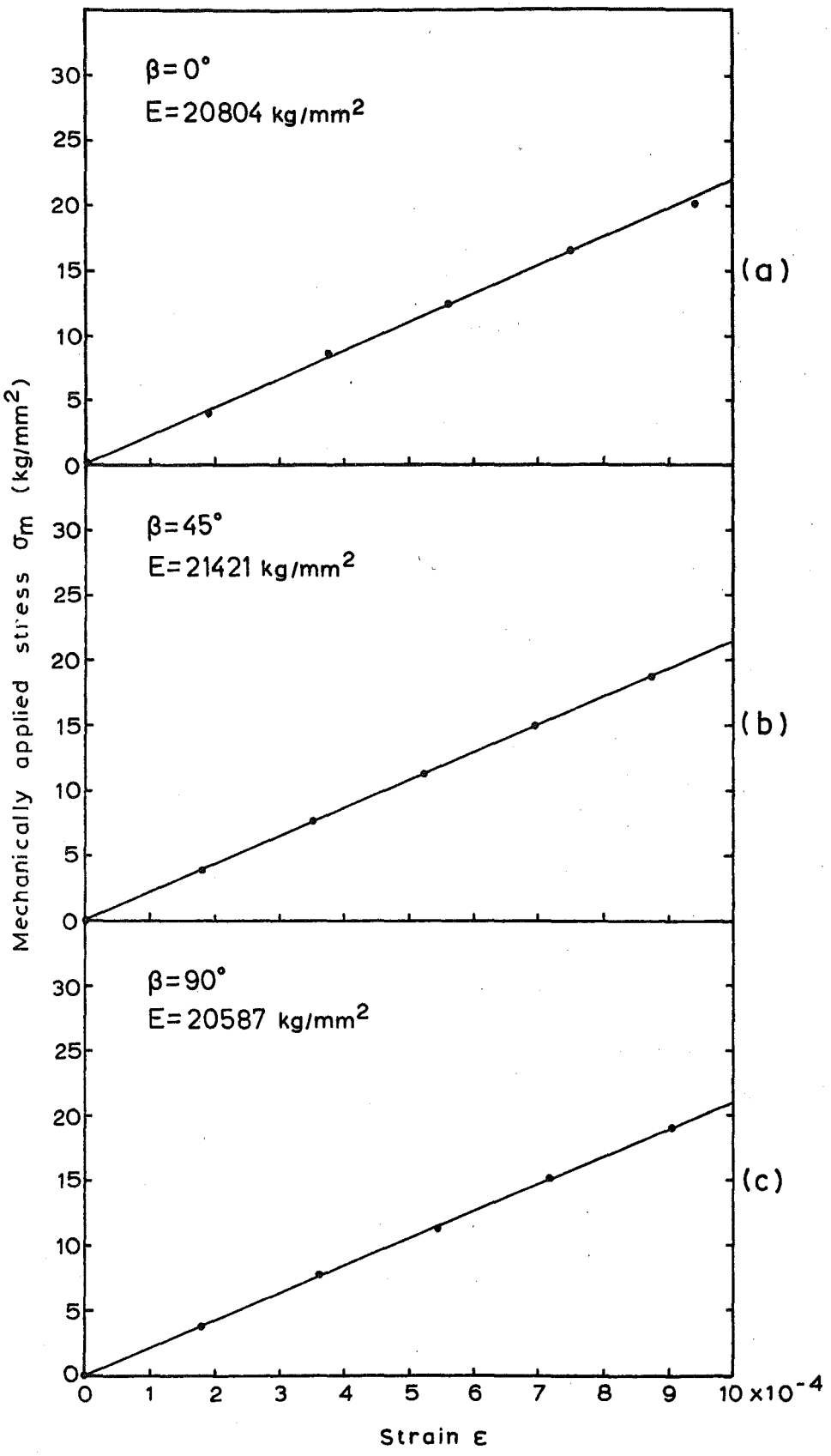

Fig.6·7 Mechanical stress-strain curves.

6.5.2 Experimental Procedure

In section 6.4, the X-ray elastic constants were determined by calibration with a specimen which was electropolished. The stress axis of that specimen was parallel to the rolling direction ($\beta = 0^{o}$). Since the X-ray stress constants are also required for directions at $\beta = 45$ deg. and $\beta = 90$ deg. to the rolling direction, two more specimens of dimensions shown in Fig. 6.4 were made with their stress axes in these directions. Hence, with the X-ray stress constants known in all these directions, X-ray stress measurements can be taken in these directions and from the results, the principal stresses can be computed.

These two specimens with stress axes at $\beta = 45$ deg. and $\beta = 90$ deg. were electropolished and X-ray stress measurements were taken at various step loadings in unaxial tension for $\psi_0 = 0$ deg. and $\psi_0 = 35$ deg. The results of the X-ray stress measurements are shown in Table 6-2(c),(d) (see Appendix 9) and the variation of applied stress σ_m with $\Delta \tan 2\theta_\psi / \Delta \sin^2\psi$ for all three specimens is plotted in Fig. 6.6. At the same time, the strains were measured during calibration experiments by electric strain gauges to obtain the mechanical E values. These results are presented in Fig. 6.7.

6.5.3 Results and Conclusion

The calculation involved in obtaining the X-ray elastic constant follows the example shown in Appendix 9. From the relation between σ_m and $\Delta \tan 2\theta_\psi / \Delta \sin^2\psi$, the linearity is good for the case where $\beta = 45$ deg., but in cases where $\beta = 90$ deg. and $\beta = 0$ deg., there is more scatter in the results (see Fig. 6.5). Since only two exposures were taken at each

TABLE 6-3: Variation of elastic properties with direction

β	$E_{X\text{-ray}}$ kg/mm^2	$\nu_{X\text{-ray}}$	K kg/mm^2	E_{mech} kg/mm^2
0°	17912	0.32	-999.5	20804
45°	16420	0.36	-892.6	21421
90°	19992	0.35	-1090.4	20587

step loading, inaccuracy is higher than when using the $Sin^2\psi$ method where four or more exposures at different inclination ψ_0 are taken. However, since all subsequent stress measurements on the welded plates were taken with the double-exposure method, the same method was used in the calibration experiment.

The experimental points at zero load prove unreliable as they deviate significantly from the least square line of σ_m versus $\Delta \tan 2\theta_\psi / \Delta \sin^2\psi$. This may be due to initial bending of the tensile specimens which were straightened out on application of load. These experimental points were neglected during the fitting of the least squaresline through the rest of the experimental points.

The variations in X-ray stress constants and elastic moduli are shown in Table 6-3. It can be seen that there is significant variation with β angle to rolling direction. In comparison, the bulk mechanical values of E did not vary by any significant amount. Hence the results confirm that anisotropy and preferred orientation have significant effects on the X-ray elastic constants and these constants differ significantly from bulk mechanical values.

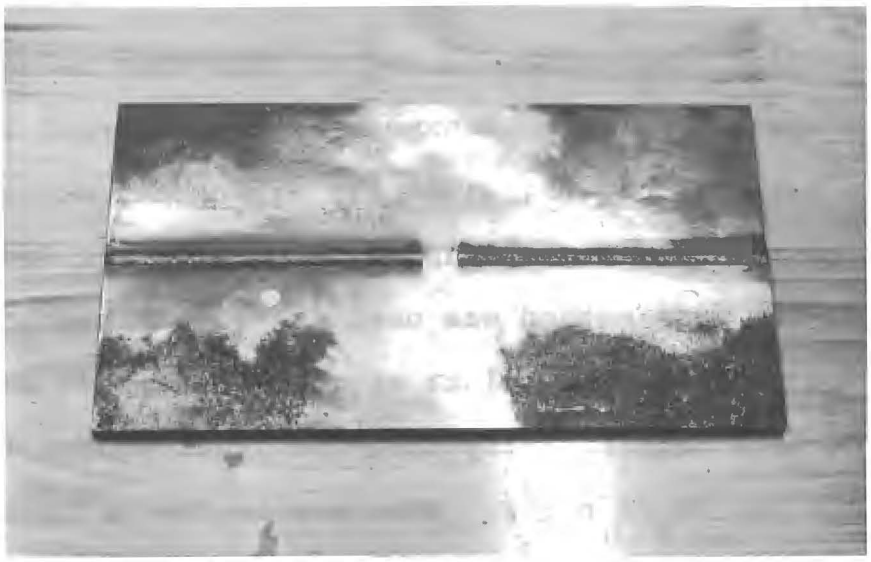

Photo showing specimen No.6
spot electropolished

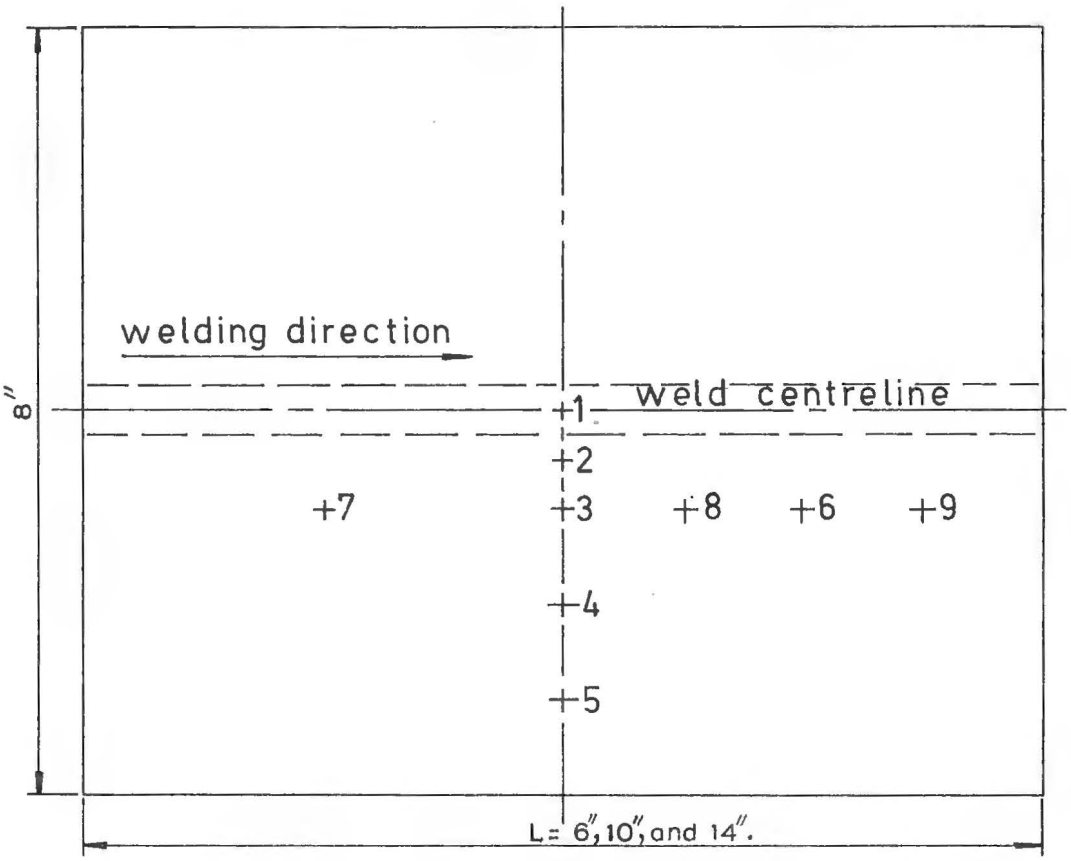

Fig.7·1 Surface preparation of welded plate.

CHAPTER 7

MEASUREMENT OF RESIDUAL STRESSES IN LOW CARBON STEEL BUTT WELDS

7.1 Introduction

In section 3.5.4, six specimens (see Table 3-5) were welded with the gas metal-arc welding process. Factors like weld length, mode of metal transfer and edge preparation were varied in the welding and their effects on the residual stress patterns are being studied as described in this chapter.

The specimens were all welded under restraint applied by clamping bars which prevent any out-of-plane distortion during welding. After welding had been completed, the specimens were freed from the restraining jig and hopefully, all the reaction stresses due to restraint would be released too. The residual welding stresses which remained after welding had completed and the weld had reached room temperature are concerned in this study.

7.2 Experimental Procedure

The specimens were electropolished at nine points on each welded plate as shown in Fig. 7.1. About 0.002 inch. in depth of metals were removed from each circular spot of 1 cm in diameter by the electropolishing process as described in Appendix 3.

X-ray measurements were taken at each point under the conditions described in section 4.7.2. The double-exposure method was applied with one normal exposure with ψ_o = 0 deg. and the other inclined exposure with ψ_o = 35 deg. The stress measurements were taken in three directions at each point in the form of a rectangular rosette. One of the measured

directions is parallel to the weld, one at 45 deg. to the weld and the other perpendicular to the weld. Hence, six exposures were required to determine the principal stresses as well as the longitudinal and transverse residual stresses at each point.

The graphical outputs from the recorder were analysed by the computer programme described in section 5.3; that is using an assumed $K\alpha_2/K\alpha_1$ ratio of 0.5. Measures of peak angle and line breadth of the resolved $K\alpha_1$ line profile were obtained. The two peak angles obtained from each direction of measurement were then substituted into equation 4.18 and together with the appropriate stress constants as obtained by calibration (see section 6.5) the surface stress in that direction was obtained.

7.3 Results

The results of the X-ray stress measurements of the residual stresses are tabulated in Tables (7-1), (7-2), (7-3), (7-4), (7-5) and (7-6) and the corresponding residual stress patterns are plotted in Fig. (7.2), (7.3), (7.4), (7.5), (7.6) and (7.7) as shown in Appendix 10. As can be seen from these plotted results, the principal stress patterns are complicated and there is marked variation in principal directions.

7.4 Effects of Mode of Metal Transfer and Edge Preparation on The Residual Stress Patterns

In this investigation, specimens No. 1, 2, 3 and 4 were studied. They were of the same dimensions; that is 2 x 4" wide x 6" long x 3/8" thick. The conditions of welding are shown in Table 3-4 and the descriptions of each specimen are shown in Table 3-5.

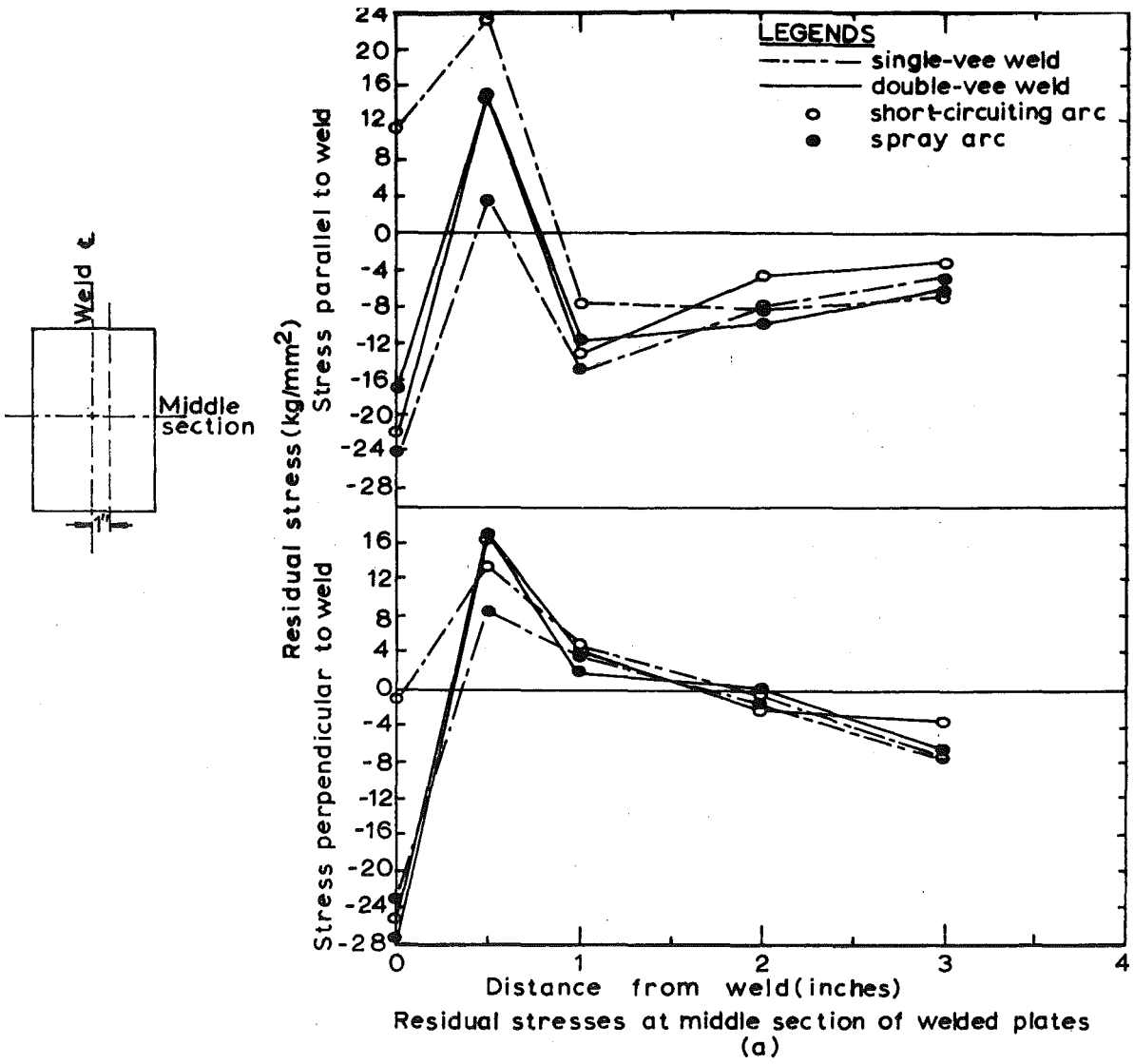

Residual stresses at middle section of welded plates

(a)

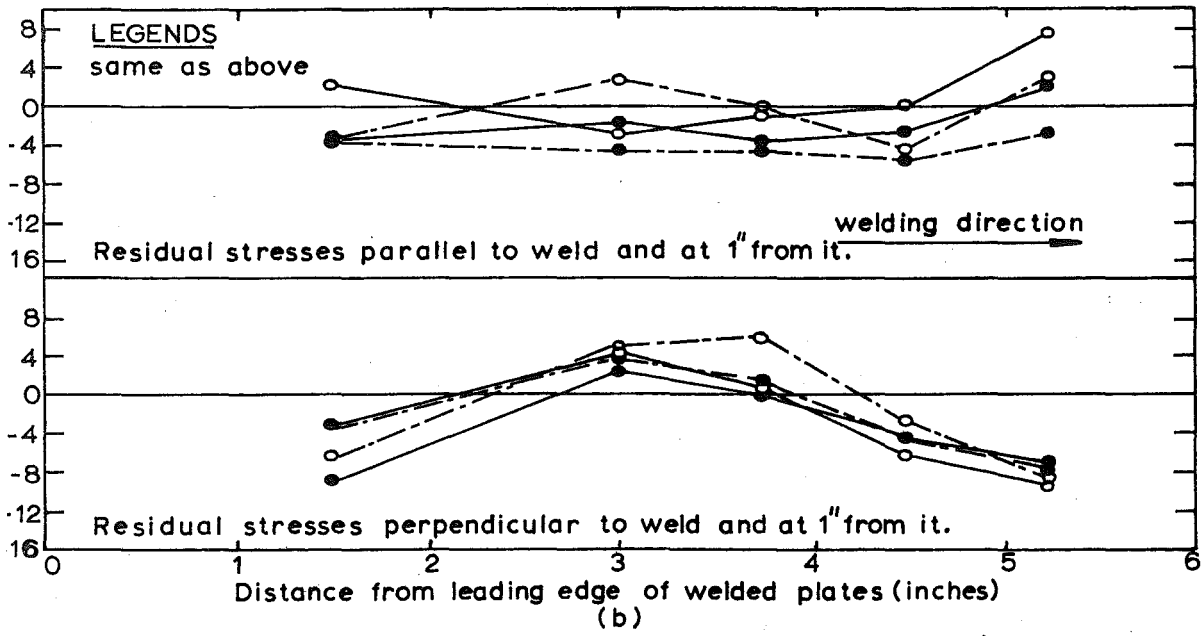

(b)

Fig.7.8 Variation of residual stress patterns with edge preparation and mode of metal transfer.

From the X-ray stress measurements (see Tables (7-2), (7-3), (7-4) and (7-5) in Appendix 10), the variation of residual stress patterns with edge preparation and mode of metal transfer is shown in Fig. 7.8. From Fig. 7.8(a), the variation of residual stresses as a function of distance from the weld at the middle section of the welded plates is shown.

It would appear that the mode of metal transfer has no significant effect on joints of double-vee design. However, for joints of single-vee design, the mode of metal transfer has significant effect on the transverse and longitudinal residual stresses. At distance 1 inch therefrom the weld, both components of residual stresses are higher in tension and lower in compression for the short-circuiting arc method. Further away from the weld the residual stresses attain moderately compressive values.

At 1 inch from the weld, it appears that edge preparation and mode of metal transfer have no effect on the residual stress patterns as shown in Fig. 7-8(b).

7.4.1 Conclusion

As can be seen in Fig. 7.8, the residual stress patterns are complicated. The scatter of experimental points for the longitudinal stresses at 1 inch from the weld seems quite random. However, the transverse stresses showed a definite pattern for all four specimens (Fig. 7.8(b)).

Similarly, the residual stresses at the middle section of the welded plates showed a definite pattern, but again the scatter of experimental points amongst the specimens provides no indication of any significant effect except for welds of single-vee design.

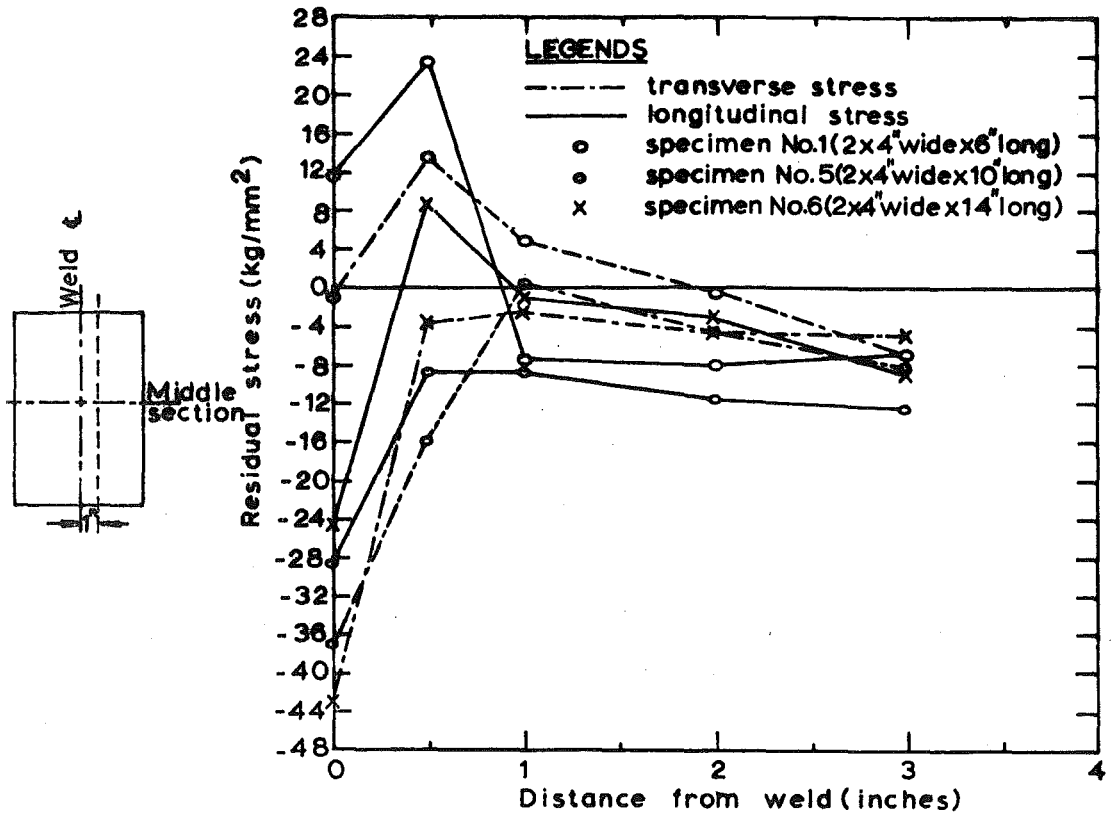

Residual stresses at middle section of welded plates

(a)

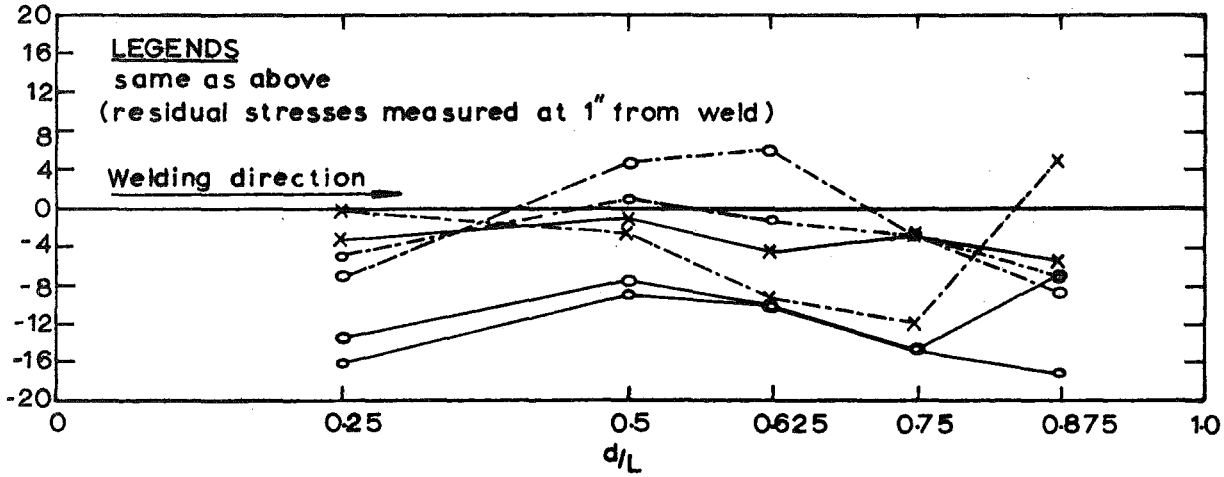

(d is the distance from leading edge of welded plate of length L)

(b)

Fig.7.9 Variation of residual stress patterns with weld length.

Hence, no real conclusive results can be reported in this section of the work except (a) mode of metal transfer has no significant effect on joints of double-vee design, but has significant effect on joints of single-vee design, (b) further away from the weld ($\geq$ 1") no significant effects were observed.

7.5 Effect of Weld Length upon Residual Stress Patterns

In this part of the investigation, specimens No. 1, 5 and 6 were studied. Welding conditions and description of the specimens are shown in Table (3-4) and (3-5) respectively. All three specimens were of the same width, edge preparation (single-vee notched) and welded with the short-circuiting arc method. The lengths of the specimens were of 6 inch, 10 inch and 14 inch.

The results of the X-ray measurements are shown in Table (7-1), (7-5) and (7-6) (see Appendix 10). The variation of residual stress patterns with weld length is plotted in Fig. 7.9. From Fig. 7.9(a) it would appear that weld length has significant effect on the residual stresses close to the weld. However, the effect is complicated to describe and the large difference in magnitudes only indicates significant effect is present. It is interesting to note that the longitudinal stresses at the middle section of specimen No. 5 are totally compressive. All other specimens exhibit at least tensile longitudinal stress at ½ inch from the weld. Similarly, the transverse residual stresses for specimen No. 6 were totally compressive along the middle section of the plate.

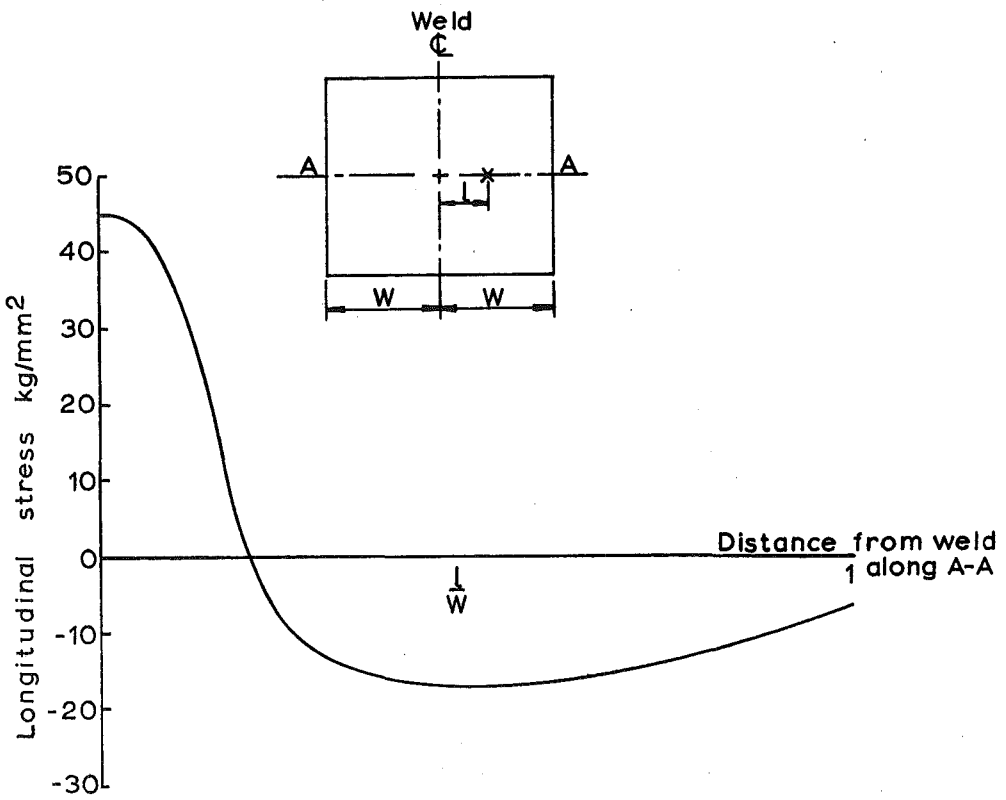

Fig.7·10 Longitudinal stress pattern obtained by mechanical methods[7,52,53] (Schematic).

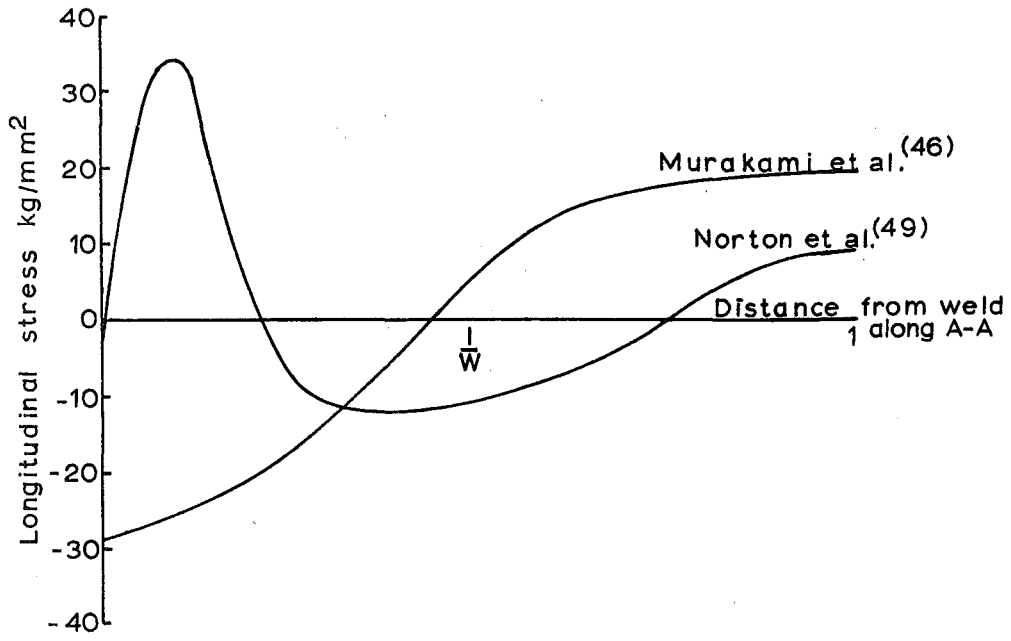

Fig.7·11 Longitudinal stress pattern obtained by X-ray method (Schematic).

From Fig. 7.9(b) the variation of residual stresses at 1 inch from the weld is shown. The distribution of transverse residual stresses at the central position indicated that increasing weld lengths depress the transverse residual stresses towards more compressive values. The longitudinal residual stresses showed a more complicated picture and they are all compressive at 1 inch from the weld.

7.5.1 Conclusion

From Fig. 7.9, it shows that weld length has significant effect on the residual stress patterns. However, the effect is complicated to describe and the results showed inconclusive indication of the effect.

7.6 Comparison of Results with Published Experimental Results

As described in section 2.4, residual stress patterns in low carbon steel butt welds measured by X-ray methods differ with workers (c.f. Murakami et al.[46] and Norton et al.[49]). Furthermore, the X-ray results differ with those obtained by mechanical methods (c.f. Gunnert[52], Greene[7], Meriam[45a] and Tall[53]).

Mechanical methods have shown consistent longitudinal residual stress patterns in the middle section of low carbon steel butt welds (Fig. 7.10). However, X-ray results of Norton et al. and Murakami et al. differ from this as shown in Fig. 7.11.

From the present investigation the longitudinal residual stress pattern at the middle section is shown schematically in Fig. 7.12. Hence it can be seen that the present results agree with that of Norton et al. Even though Norton et al. obtained the residual stress patterns from a edge-welded plate,

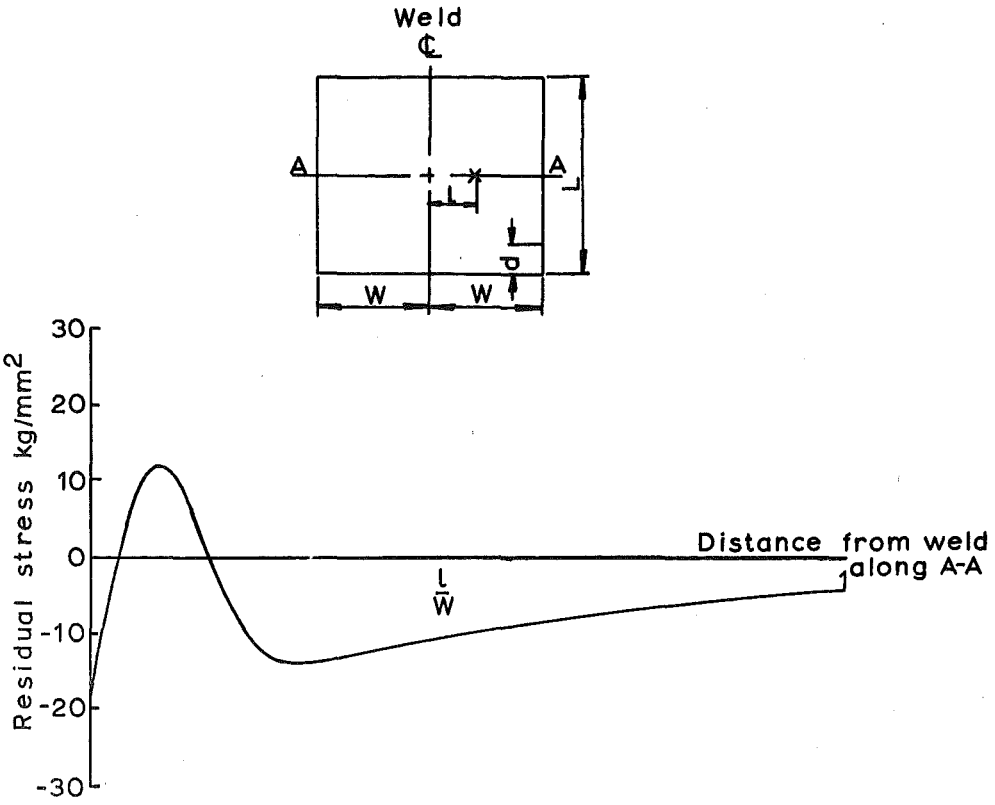

Fig.7·12 Longitudinal stress pattern obtained in present work (Schematic).

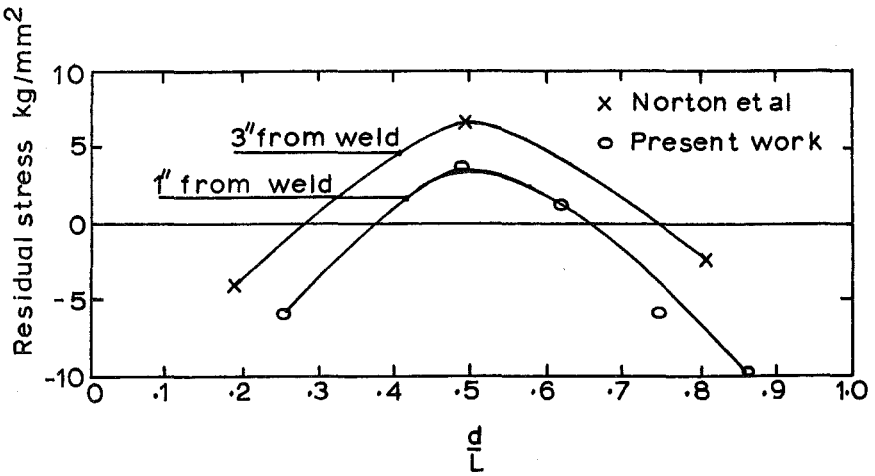

(d is the distance from leading edge of welded plate as shown above)

Fig.7·13 Transverse stress pattern at a constant distance from weld.

it has been shown by Tall that the residual stress patterns are similar for both centre-welded and edge-welded plates.

Furthermore, from a plot of transverse residual stresses at a constant distance from the weld, Norton et al.'s results fall in place with those obtained in the present study as shown in Fig. 7.13. Hence it can be concluded that the present results are similar to that of Norton et al.

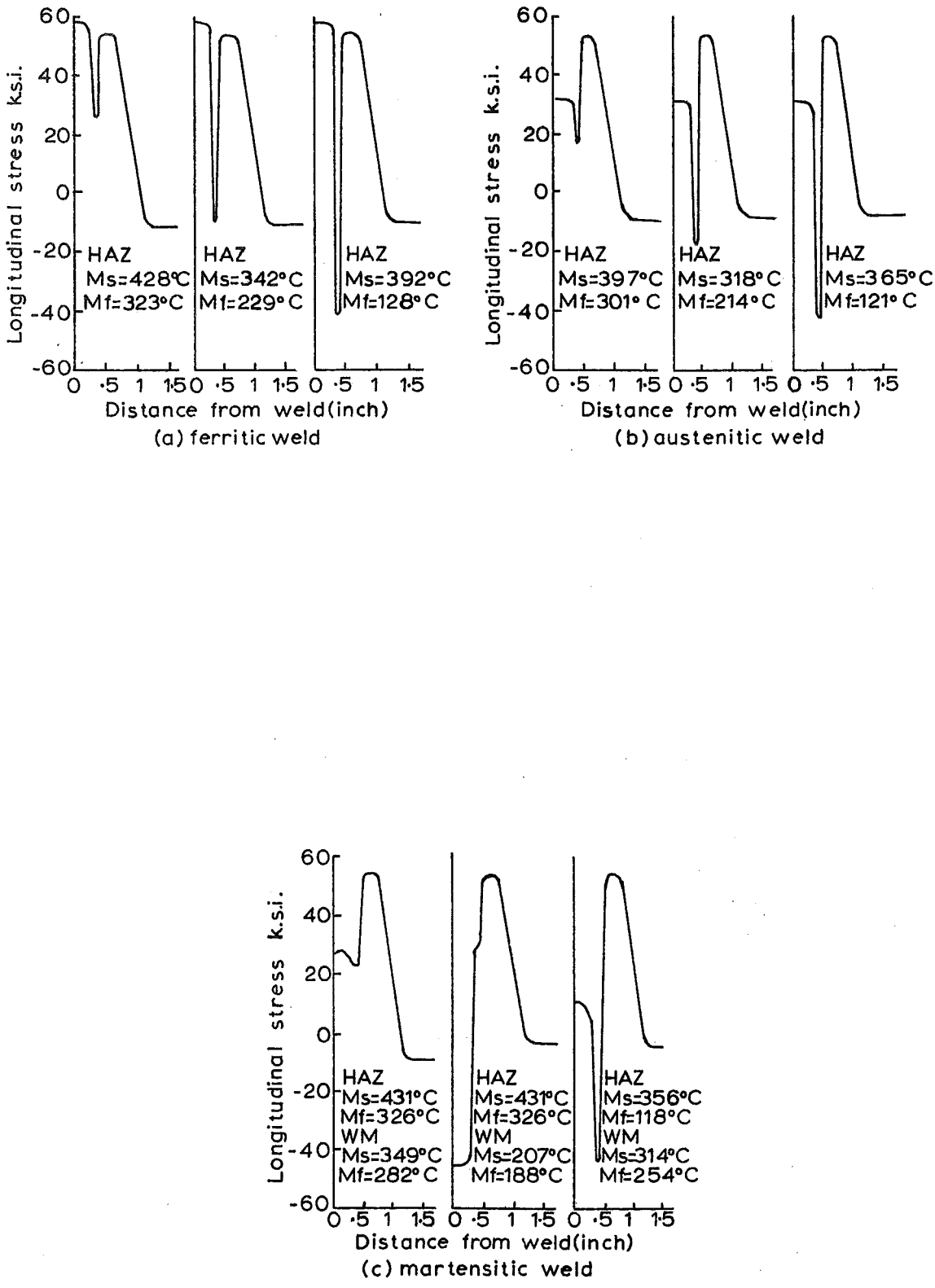

Fig.8·1 Theoretical stress profiles calculated on the basis of three different transformation ranges for the weld metal and HAZ.[48]

CHAPTER 8

MECHANICAL TESTING OF WELDED SPECIMENS AND GENERAL CONCLUSION

8.1 Introduction

This section of the work describes an effort to establish the cause of compressive residual stress on the weld bead as revealed by the X-ray measurements in the present study. At the same time, mechanical testing of the welded plates for strength and macro- and micro-examinations of the weld for defects were made.

Recently, Wilson et al.[48] revealed that martensitic transformation[95a] in the weld bead can induce high compressive residual stresses in the weld bead and also in the fusion zone. In his work he showed typical residual stress patterns in medium carbon steel caused by ferritic weld deposit, austenitic weld deposit and martensitic weld deposit as shown in Fig. 8.1.

It would appear that martensitic transformation could plausibly induce high compressive stresses in the weld bead and thus prompted the author to make an investigation into the welds.

8.2 Macro- and Micro-Examination and Hardness Survey of Welds

Blocks containing the weld bead were machined from each welded plate as shown in Fig. 8.2. Macro-specimens were prepared from these blocks by etching with 10% Nital solution. From this the following macrographs were obtained as shown in Fig. 8.3.

From the macrographs, all spray arc welded specimens showed complete penetration and the absence of porosity.

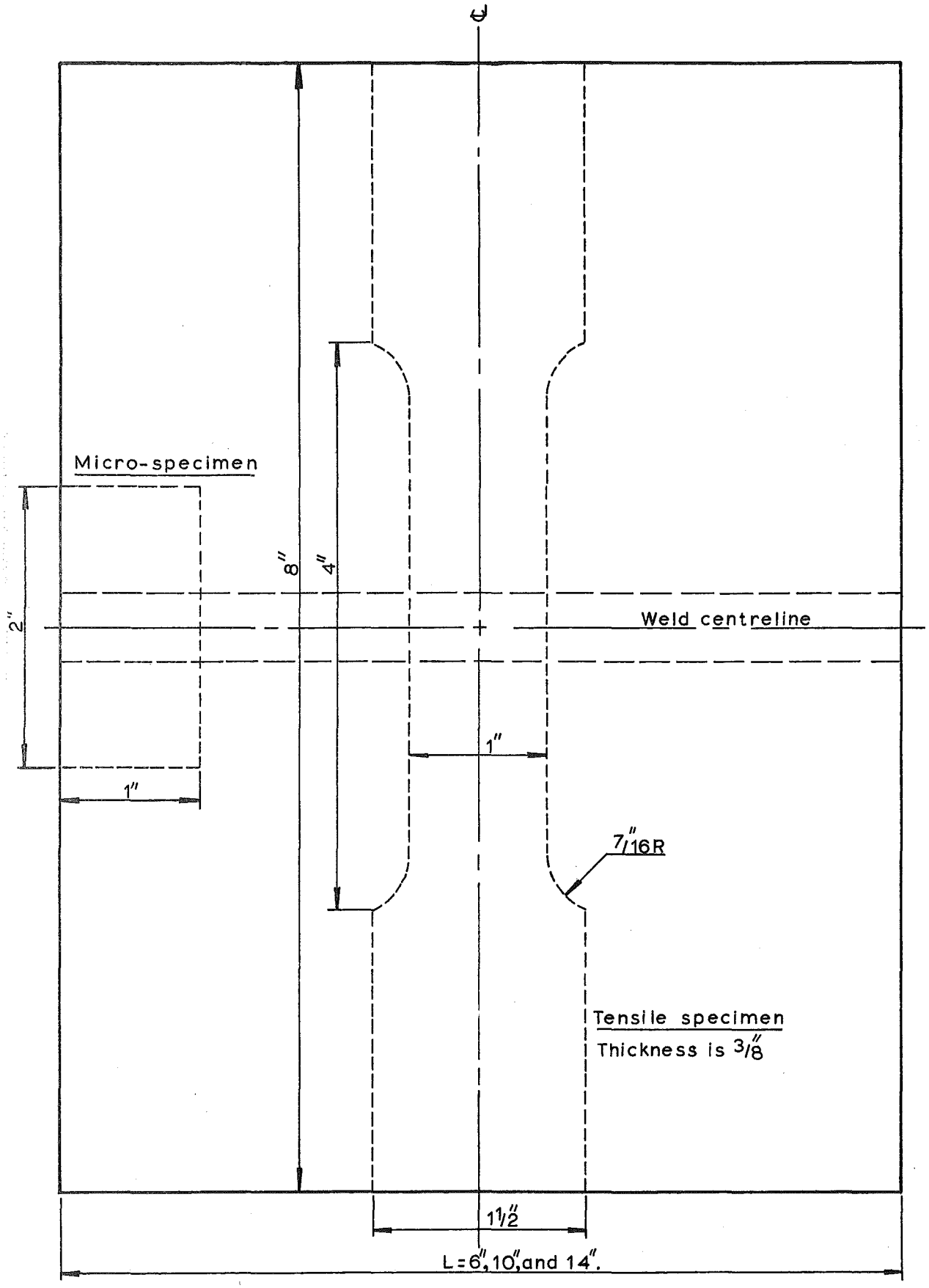

Fig. 8·2 Tensile and micro-specimens from welded plate.

However, for welds produced by the short-circuiting arc, some porosity was observed during the polishing stage. Complete penetration was suspect in specimen No. 1.

From these specimens, two single-vee welded specimens were selected for micro-examination and hardness survey. They were chosen from specimen No. 1 and 2; that is one was welded by the short-circuiting arc method and the other by the spray arc method. These specimens were repolished for micro-examination. Widmanstatten structures were observed in both welds. Martensite was not observed, however some intermediate structures were observed on the fusion zone.

From a survey of hardness across the weld beads (see Fig. 8.4), there is evidence to support the presence of martensite in the fusion zone which lies between the weld bead and the heat-affected zone. A maximum hardness of 300 VPN was observed in specimen No. 1. This is about the hardness of martensite of low carbon content[95b]. Further testing on the fusion zone revealed similar hardness of 300 VPN. A close examination of the microstructure around the indentation revealed some sign of martensite in the matrix of ferrite and pearlite.

It ought to be noted that the hardness tests performed in the above survey did not conform to BS427: Part 1: 1961, Method of Test, which specified that the distance between centre of indent must be not less than 2.5 * d (d is the mean diagonal length of the indent) whereas in the above test, they were closer than this.

TABLE 8-1: Tensile test on welded specimens

Specimen No. (same as welded plate specimen No.)	Yield stress kg/mm^2	Ultimate tensile stress kg/mm^2
1	30.89	46.87
2	29.83	46.66
3	30.90	46.14
4	29.72	46.70
5	29.74	46.84
6	29.76	46.24

8.2.1 Conclusion

Even though the hardness tests did not conform to BS427, the presence of martensite was confirmed by observation. However, the narrow strip of martensite in the underbead region is deemed to be insufficient to create a totally compressive zone in the weld bead. Especially in the spray arc welded specimen, no martensite was observed, but X-ray results indicated high compressive residual stresses on the weld bead. Hence the reliability of the present X-ray results on the weld bead must be questioned.

8.3 Mechanical Testing of Welded Plates

Tensile specimens of the dimensions as shown in Fig. 8.2 were machined from each welded plate. They were tested on the STE (Southwark Tate Emery) tensile testing machine and the results of the tests are shown in Table 8-1.

From the results obtained the yield strength and ultimate tensile strength of the welded specimens were higher than the corresponding parent metal before welding (c.f. Table 3-3). Furthermore, all the specimens failed in the parent metal and not in the weld (Fig. 8.5). Therefore, it can be concluded that the welds are sound in strength.

8.4 Conclusion

The present investigation has revealed that surface preparation and preferred orientation have significant effect on the X-ray stress measurements. Electropolishing must be recommended as the method of surface preparation because it is an efficient method of stress-free removal of metals. However, suitable equipment for practical applications on large

Specimen No.1

Specimen No. 2

Specimen No.3

Specimen No. 4

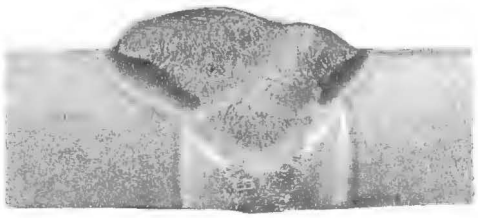

Specimen No.5

Specimen No.6

Fig.8·3 Macrographs

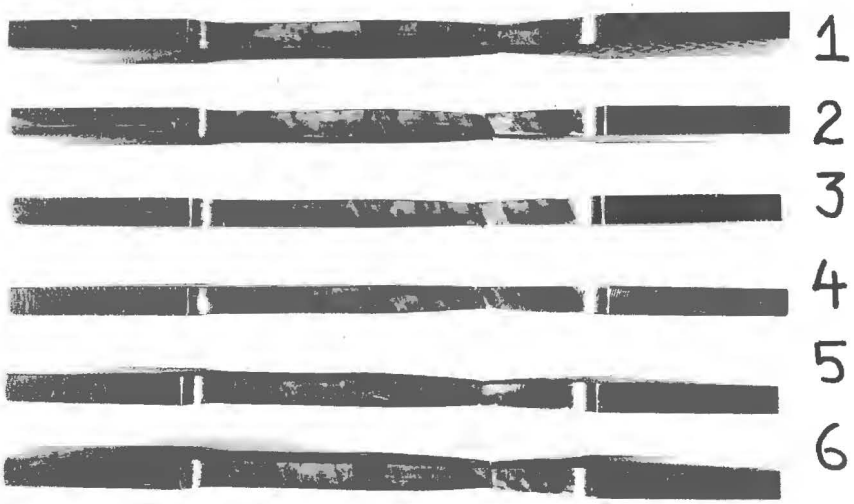

Fig.8·5 Tensile failures of welded specimens.

specimens poses a problem. A promising method proposed by Jacquet appears to be the obvious solution; that is the tampon method as described in Appendix 3. This type of portable electropolishing set-up seems most suitable for electropolishing small areas of interest in large specimens.

The effect of preferred orientation on the X-ray stress constant is significant and it is imperative that the appropriate stress constant be used in X-ray stress measurements.

The reliability of X-ray method of residual stress measurements must be studied in greater detail. Present results showed unusual residual stress patterns in low carbon steel butt welds. The scatter of experimental points on the stress patterns seem too great to be accounted for by normal experimental error. From calibration experiments (see Fig. 6.5) the largest deviation from the least mean square line is about 1 kg/mm^2 as found in the case where the stress axis coincides with the rolling direction (β = 0 deg.).

The author would suggest that the large scatter could be due to local variation of initial stresses present in the parent plates after the recovery annealing process. From a measurement of initial stresses in the recovery annealed plate before welding, the initial stress field obtained is shown in Fig. 8.6. It must be noted that the method of surface preparation was by abrading the surface with medium emery paper followed by etching with 10% Nital. Hence higher compressive stresses are computed (see section 6.3). The magnitudes of the initial stresses vary between -20.4 kg/mm^2 to -12.1 kg/mm^2.

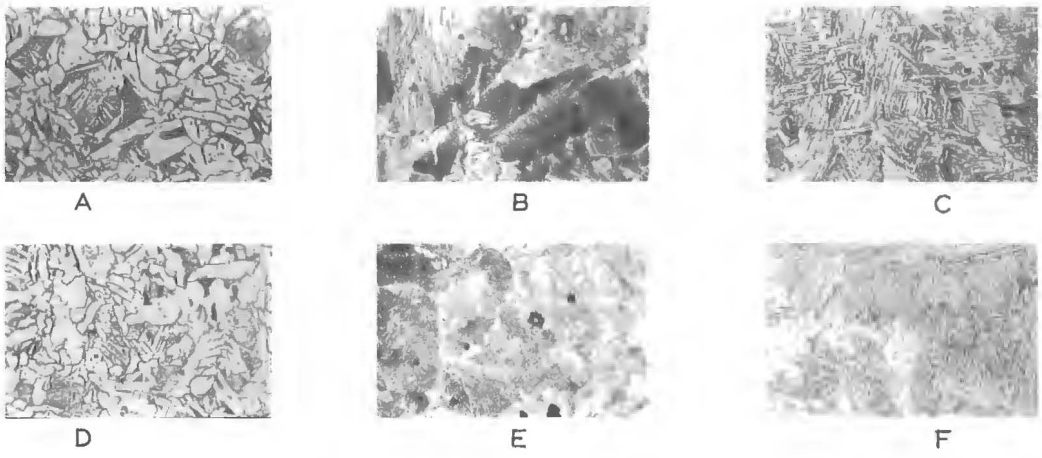

Fig.8·4(b) Micrographs (600 x)

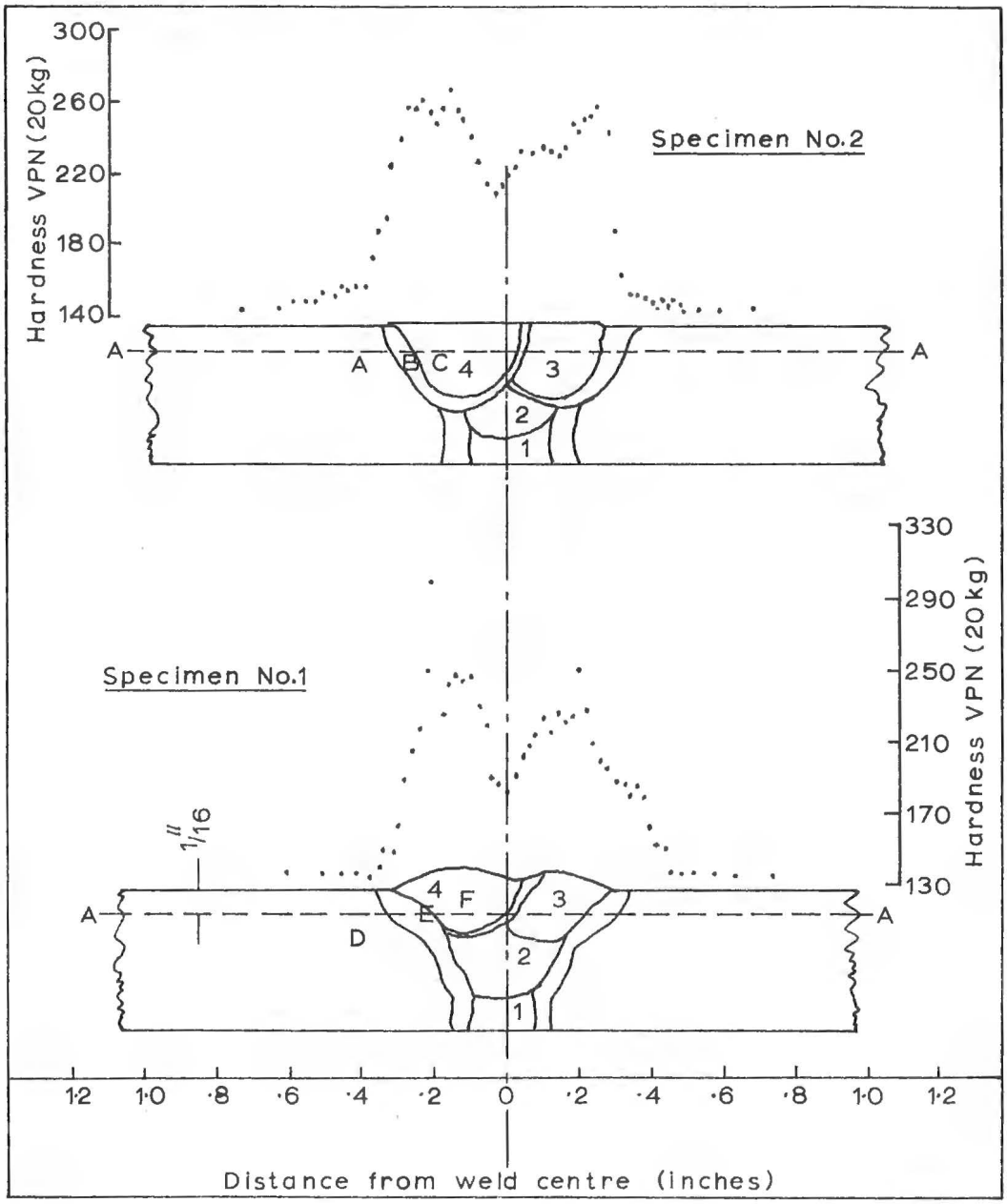

Fig.8·4(a) Hardness survey across section A-A for joints welded under Carbon dioxide atmospheres. Microstructures at points A-F are shown in Fig.8·4(b).

Hence the immediate question of how the initial stresses combine with subsequent residual welding stresses arising from the welding process poses a real problem. With large local variation in initial stresses in the parent plates, the residual welding stress patterns could plausibly be obscured.

A probable solution would be to stress-relieve the parent plates completely to ensure a homogeneous and uniform initial stress field prior to welding. However, this may not be easy to achieve in aggregate of polycrystalline metals. This is due to the anisotropic thermal behaviour of single crystals of iron together with constituents which have different thermal properties again. Unless the metals are in powder form or filings where the grains are free to expand or contract, full annealing may ensure a stress-free sample as used by Stokes in his 'unfolding' method of obtaining true diffraction profiles (section 5.2).

Finally it can be concluded that the present results on residual stress pattern in low carbon steel butt welds are inconclusive in view of the large scatter of experimental points. Other than the few observations made in sections 7.4, 7.5 and 7.6, no further comments can be added.

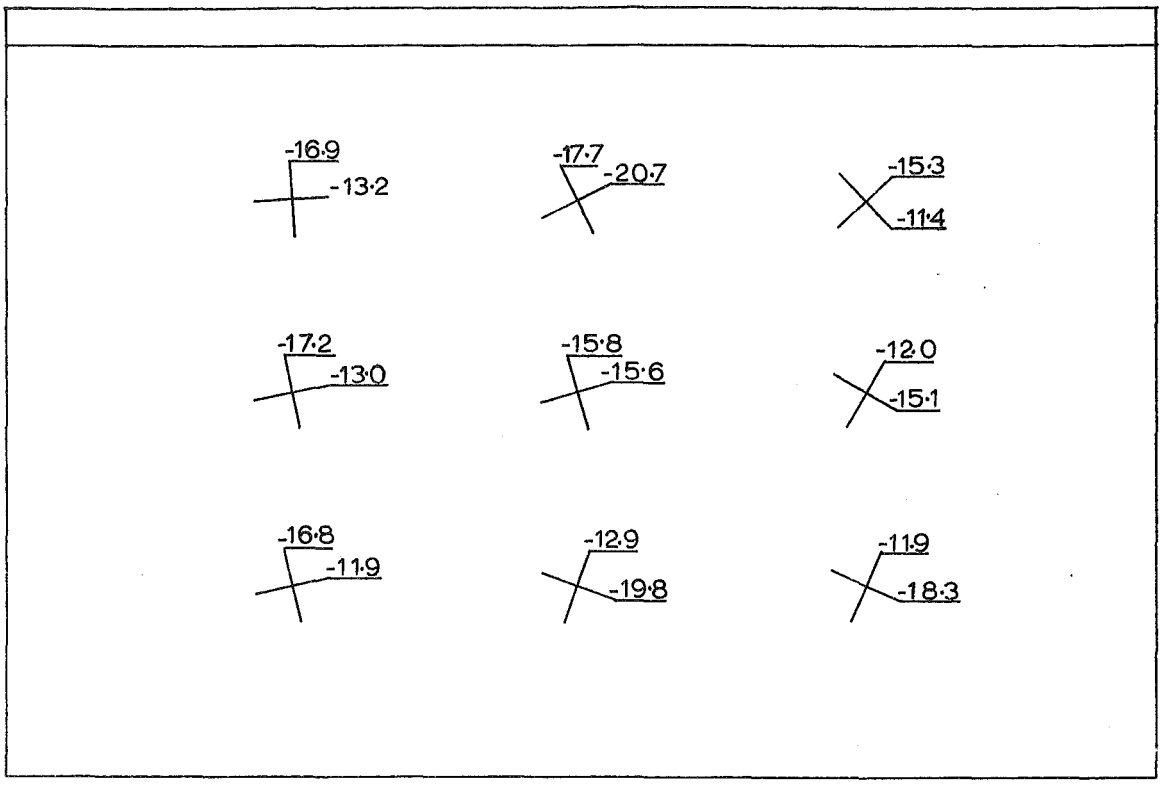

Principal stresses in recovery annealed parent plate before welding.

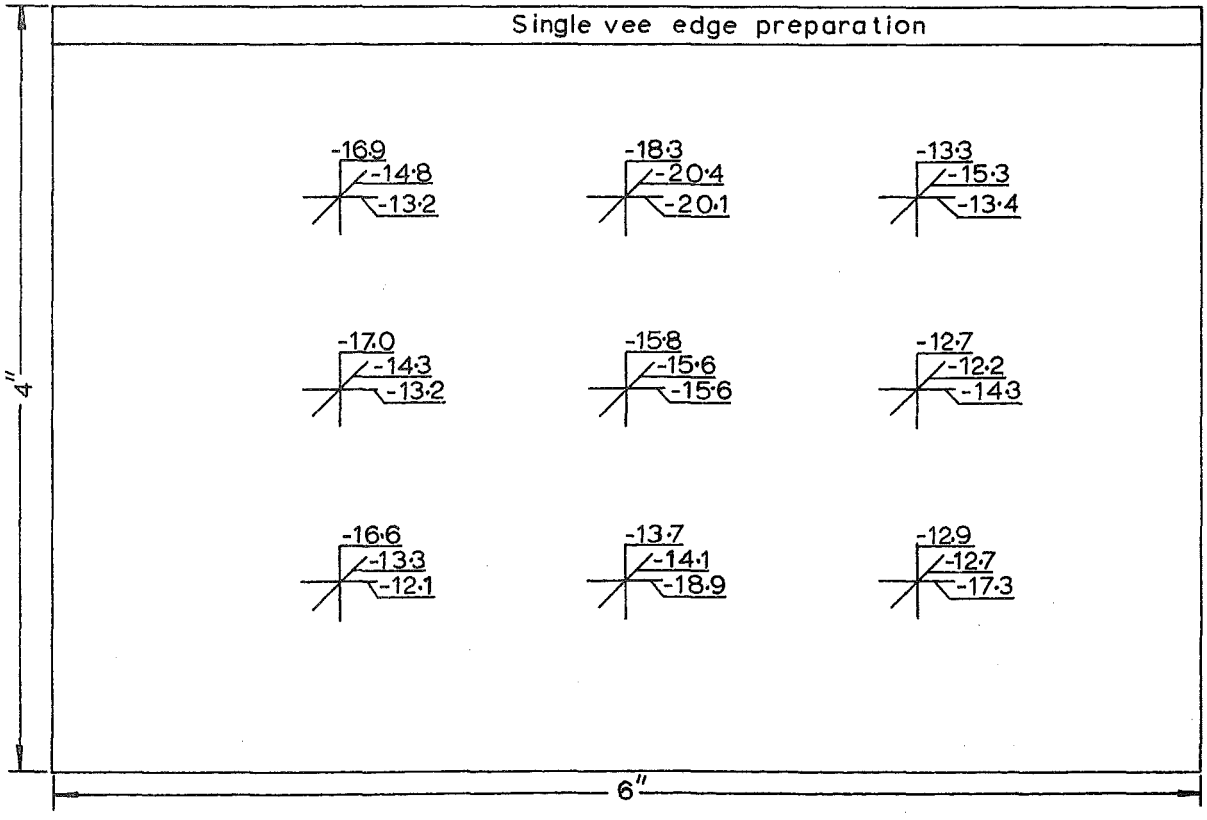

Fig.8·6 Initial stresses in recovery annealed parent plate before welding.(plate was part of specimen No.1)

BIBLIOGRAPHY

1. Symposium on Stress Corrosion Cracking of Metals (ASTM-AIMME), (1944).
2. F.H. Keating, Symposium on Internal Stresses in Metals and Alloys, Inst. of Metals, London, 318-321 (1947).
3. A.G. Warren, Ibid, 209-220 (1947).
4. M.J. Donachie and J.T. Norton, Proc. Soc. Exp. Stress Analysis, Vol. 19, No. 2, 222-224 (1962).
5. W.W. Wilson and C.C. Hao, Residual Stresses in Welded Structures, Bulletin No. 361, University of Illinois, (Feb. 1946).
6. A.G. Cepolina and D.A. Canonico, Weld. J., 31s-38s (Jan. 1971).
7. T.W. Greene and A.A. Holzbaur, Ibid, 171s- (March 1946).
8. W. Spraragen and G.E. Claussen, Ibid, 16, 2s-61s (1937).
9. R. Weck, Symposium on Internal Stresses in Metals and Alloys, Inst. of Metals, London, 119-129 (1947).
10. L.S. Beedle and L. Tall, Basic Column Strength, Trans. ASCE, Vol. 126, Part II, 138-179 (1962).

11a. J. Mathar, Determination of Initial Stresses by Measuring the Deformation around Drilled Holes, Trans. ASME, 56, 249-254 (1934).

11b. Goodier and Thimoshenko, Theory of Elasticity, McGraw-Hill Kogakusha, Tokyo, 466- (1970).

12. F.W. Barton and W.J. Hall, Weld. J., 39(9), 3792- (1960).
13. Hall, Kihara, Soete and Wells, Brittle Fracture of Welded Plates, Prentice-Hall, 54-55 (1967).
14. G.A. Alpsten and L. Tall, Weld, J., 93s-105s (1970).

15. W.A. Wood, Symposium on Internal Stresses in Metals and Alloys, Inst. of Metals, London, 31-34 (1947).

16. A. Taylor, X-ray Metallography, John Wiley, New York (1961): (a) 724; (b) 524; (c) 726; (d) 674; (e) 561; (f) 807; (g) 812; (h) 752-757; (i) 249; (j) 69.

17. Symposium on Internal Stresses in Metals and Alloys, Inst. of Metals, London, Section I (1947).

18. E. Orowan, Ibid, 47-60.

19. E. Macherauch, Exp. Mech., Vol. 6, 146- (March 1966).

20. R. King, Symposium on Internal Stresses in Metals and Alloys, Inst. of Metals. London, 13-22 (1947).

21. Heindlhofer, Evaluation of Residual Stress, McGraw-Hill, New York, 113-143 (1948).

22. D.E. Thomas, Symposium on Internal Stresses in Metals and Alloys, Inst. of Metals, London, 25-30 (1947).

23. G. Sachs, C.S. Smith, J.D. Lubahn, G.E. Davis and L.E. Ebert, Weld. J., 400s- (July 1946).

24. J.T. Norton and D. Rosenthal, Proc. SESA, Vol. V, No. 1, 71-77.

25. C.W. Tucker Jr and H.V. Anderson, Proc. SESA, Vol. IX, No. 2, 67-74.

26. A.L. Rutledge, M.E. thesis, University of Canterbury, NZ (1970).

27. D.N. French and B.A. MacDonald, Exp. Mech., Vol. 9, 456-462 (Oct. 1969).

28. F. Preisach, Physikal. Z., 33, 913- (1932), (cited by 20).

29. P.E. Cavanagh, Trans. Amer. Soc. Metals, 36, 137- (1946), (cited by 20).

30. Davis, Troxell and Wiskocil, Testing and Inspection of Engineering Materials, McGraw-Hill, 2nd Edn., New York, 83-86 (1955).

31. N.H. Rendler and I. Vigness, Exp. Mech., 577-586 (Dec. 1966).

32. R.A. Kelsey, Proc. SESA, Vol. XIV, No. 1, 181-194.

33. R.G. Bathgate, Strain J. of British Soc. for Strain Measurement, Vol. 4, No. 2, 20-29 (April 1968).

34. W. Soete and R. Vancombrugge, Proc. SESA, Vol. VIII, No. 1, 17-28.

35. High Ford, Symposium on Internal Stresses in Metals and Alloys, Inst. of Metals, London, 3-11 (1947).

36. Hall, Kihara, Soete and Wells, Brittle Fracture of Welded Plates, Prentice-Hall, 143-172.

37. S. Abuku and B.D. Cullity, Proc. SESA, Vol. XXVIII, No. 1, 217-223 (1971).

38. G.T. Hahn, P.N. Mincer and A.R. Rosenfield, Ibid, 248-253.

39. American Welding Society, Welding Handbook, Part 2, 5th Edn., Macmillan, London (1964): (a) 27.29-27.53; (b) 27.23; (c) 27.41-27.45.

40. Boulton and Lance Martin, Proc. Inst. Mech. Engrs (London), 133, 295-347 (1936).

41. Rodgers and Fetcher, Weld. J., 17(11), 4s-7s (1938).

42. J. Weiner, J. Appl. Mech., 23(3), (Sept. 1956).

43. D. Rosenthal, Weld. J., 20, 220- (1941).

44. D. Rosenthal and R. Schmerber, Ibid (April 1938).

45. J.L. Meriam, E. Paul Degarmo and Finn Johassen, Ibid, Research Suppl., (1946): (a) 697s-699s; (b) 485s-486s; (c) 340s-343s.

46. Y. Murakami, T. Kawabe and I. Iwasaki, J. Soc. Matl. Sci., Japan, 13, 984- (1964), (cited in 19).

47. R.A. Stephen, Trans. Inst. Welding, 1, 108-116 (1938).

48. M. Wilson, D.J.H. Corderoy and H. Muir, Uniciv Report No. R-79, (Feb. 1972), University of New South Wales, Australia.

49. J.T. Norton and B.M. Loring, Welding J., Research Suppl., (June 1941).

50. Seferian, The Metallurgy of Welding, Chapman and Hall, London, 11- (1962).

51. R. Weck, Welding J., 28(1), 9s-14s (1949).

52. R. Gunnert, Residual Welding Stresses, Almquist and Wiksell, Stockholm (1955).

53. N.R. Nagaraja Rao and Lambert Tall, Welding J., 468s-480s (1961).

54. P. Boughton and J.A. Lucey, British Welding J., Vol. 12, 159- (1965).

55. C.S. Barrett, Structure of Metal, McGraw-Hill, New York, (1943): (a) 416; (b) 448; (c) 375; (d) 432; (e) 420; (f) 431.

56. S. Taira, K. Hayashi and Z. Watase, Proc. 12th Jap. Cong. on Mat. Research, 1-7.

57. G.E. Linnert, Welding Metallurgy, 3rd Edn., Vol. 1 and 2, American Welding Society, (1967): (a) 159 (Vol. 2); (b) 106 (Vol. 1); (c) 398 (Vol. 1); (d) 200 (Vol. 2).

58. A.J.C. Wilson, Mathematical Theory of X-ray Powder Diffractometry, Philips Technical Library (1963): (a) 84; (b) 91-105; (c) 54-68.

59. F. Weinberg, Tools and Techniques in Physical Metallurgy, Marcel Dekker, Inc., New York, Vol. 1 (1970): (a) 292; (b) 231; (c) 127; (d) 142; (e) 149.

60. Clark, Applied X-rays, 4th Edn., McGraw-Hill (1955), 721-.

61. H.H. Lester and R.H. Aborn, Army Ordnance 6, 120-127, 200-207, 283-287, 364-369 (1925-6), (cited in 23).

62. G. Sachs and J. Weerts, Zeitschr. Phys. 64, 344-358 (1930); Metallurgist 8, 51- (1932), (cited in 23).

63. Karl E. Beu, ASTM Bulletin, 1282-1289 (1957).

64. H.R. Letner and S.R. Maloof, J. Appl. Phys., Vol. 25, 1440- (1954).

65. A.L. Christenson and E.S. Rowland, Trans. Amer. Soc. Metals, Vol. 45, 638-676 (1953).

66. Shuji Taira and Jyunichi Arima, Proc. of 6th Jap. Cong. on Testing Materials, 158-166.

67. M.J. Donachie Jr and J.T. Norton, Trans. AIME 221, 962- (1961).

68. E. Macherauch, Advan. X-ray Anal., 9, 103- (1965).

69. Kozaburo Hayashi, Doctor of Engineering thesis, University of Kyoto, Japan (1970).

70. H.A. Davies and C.N.J. Wagner, J. of Mat. Science 7, 105-114 (1972).

71. W.A. Wood, Proc. Roy. Soc. (London) (A), 192-218 (1948), (cited in 16h).

72. K. Kolb and E. Macherauch, Z. Metalk. 53, 108- (1962).

73. J.T. Fourie, Phil. Mag., 21, 173- (1970).

74. R.J. Block and R.M. Johnson, Scripta Metall. 3, 511- (1969).

75. I.R. Kramer and A. Kumar, Ibid, 3, 205- (1969).

76. W.T. Brydges, Ibid 2, 557- (1968).

77. S. Kitajima, H. Tanaka and H. Kaieda, Trans. J.I.M., 10, 10- (1969).

78. W.J. McG. Tegart, The Electrolytic and Chemical Polishing of Metals, Pergamon Press, Oxford, 2nd Edn (1959).

79. K. Honda, N. Hosokawa and J. Arima, Proc. of 14th Jap. Cong. on Mat. Research, 149-157 (1971).

80. S. Thimoshenko and J.N. Goodier, Theory of Elasticity, 213-227 (1951).

81. T. Shiraiwa and Y. Sakamoto, Proc. 13th Jap. Cong. on Mat. Research, 25-32 (1970).

82. A.R. Stokes, Proc. Phys. Soc. Lond., 61, 382-391 (1948).

83. W. Wallace and T. Terada, Metallography 4, 339-342 (1971).

84. W.A. Rachinger, J. Sci. Instr. 25, 254- (1948).

85. S. Taira, Y. Yoshioka and Y. Sakata, Proc. 9th Jap. Cong. Testing Mat., 48-53 (1966); Ibid, 10th, 166-170 (1967).

86. S. Taira, T. Goto and T. Ishihara, X-ray Study on Strength and Deformation of Metals, J. of the Soc. Mat. Sci., Japan, 125-134 (1971).

87. A. Gangulee, J. Appl. Cryst., 3, 272- (1970).

88. W. Parrish, Advances in X-ray Diffractometry and X-ray Spectrography, Centrex Publishing Co., 71- (1962).

89. J.H. Williams, Phys. Review 44, 146- (1933).

90. A. Guinier, X-ray Diffraction in crystals, imperfect crystals and amorphous bodies, W.H. Freeman and Co., 370- (1963).

91. O.L. Davies, Design and Analysis of Industrial Experiments, Oliver & Boyd, 2nd Edn, 124- (Example 4.4), (1971).

92. L.E. Samuels and G.R. Wallwork, J. Iron & Steel Inst., 186, 211- (1957).

93. M.G. Moore and W.P. Evans, SAE Trans., 66, 340- (1958).

94. M.J. Donachie and J.T. Norton, Trans. Amer. Soc. Metals, Vol. 55, 51-57 (1962).

95. Reed-Hill, Physical Metallurgy Principles, D-Van Nostrand, (1964): (a) 503; (b) 501.

96. K. Masabuchi and N.T. Ich, Welding J., 166s- (April 1970).

97. Zienkiewicz, The Finite Element Method, McGraw-Hill (1967).

98. P.A. Jacquet, Proc. ASTM, 57, 1290- (1957).

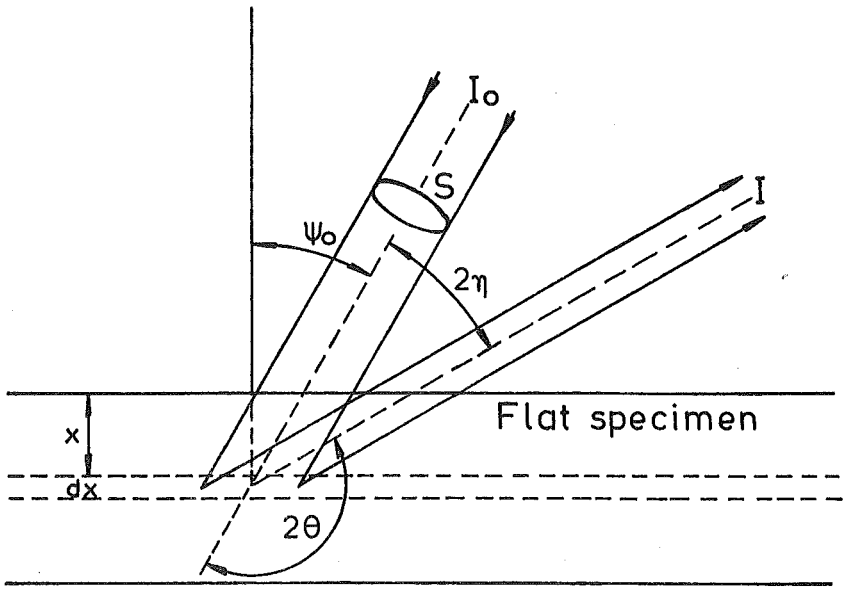

Fig.A1·1 Absorption of X-rays in the back reflection case.

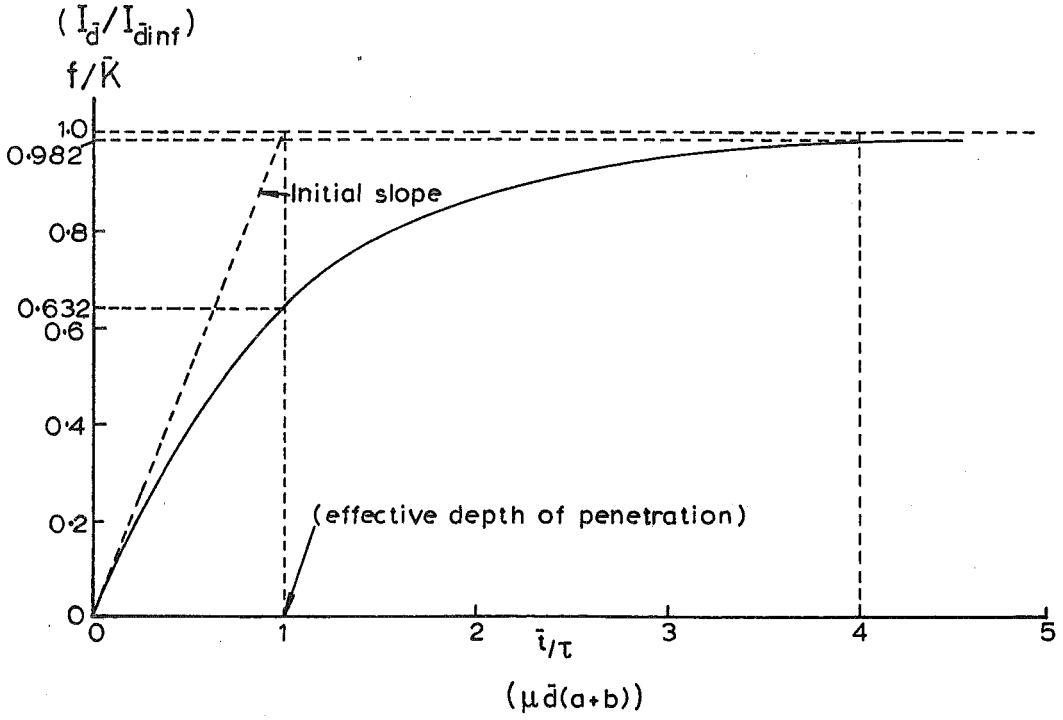

Fig.A1·2 Response of first-order systems with step inputs (which is analoguous to the variation in depth of penetration of the diffracted X-ray beam shown in parentheses).

APPENDIX 1

EFFECTIVE DEPTH OF PENETRATION

Consider the generalised Bragg case of absorption of K radiation as shown in Fig. A1.1. The total path length traversed by the X-ray beam for reflection from a volume $\frac{S\,dx}{\cos\psi_0}$ lying x cm below the surface is $\frac{x}{\cos\psi_0} + \frac{x}{\cos(\psi_0+2\eta)}$. The total energy reflected by the crystals down to a depth $\bar{d}$ cm can be expressed as follows[16i]:

$$I_{\bar{d}} = QI_0Sa \int_0^{\bar{d}} e^{-\mu x(a+b)} \cdot dx \qquad \text{(A1.1)}$$

where Q = factors like temperature factor, angular factor, and others which affect the reflected X-ray intensity.

$$a = \frac{1}{\cos\psi_0}$$

$$b = \frac{1}{\cos(\psi_0+2\eta)} \qquad \text{(A1.2)}$$

and μ = the linear coefficient of absorption of Kα radiation.

Thus from equation (A1.1) we have

$$I_{\bar{d}} = \frac{QI_0Sa}{\mu(a+b)}\left(1 - e^{-\mu\bar{d}(a+b)}\right)$$

When d is effectively infinite,

$$I_{\bar{d}inf} = \frac{QI_0Sa}{\mu(a+b)} \qquad \text{(A1.3)}$$

Hence we have

$$\frac{I_{\bar{d}}}{I_{\bar{d}inf}} = 1 - e^{-\mu\bar{d}(a+b)} \qquad \text{(A1.4)}$$

In this dimensionless form, it is analogous to a first order response equation:

$$f/\bar{K} = 1 - e^{-\bar{t}/\tau}, \qquad \text{(A1.5)}$$

where f is some function,

$\bar{K}$ is its steady-state value,

$\bar{t}$ time,

τ time constant.

The response of such first order system with step inputs is shown in Fig. A1.2. When $\bar{t} = \tau$ the output has reached $(1-e^{-1}) = 0.632$ of its final value, when $\bar{t} = 4\tau$, the output will have reached $(1-e^{-4}) = 0.982$ of its final value. Hence the constant τ influences the response of the system and thus gives useful estimate of the response time of a first order system.

In X-ray measurements, there is no general agreement on how the effective depth of penetration should be defined. Various investigators[26,27,69] have used different percentages of diffracted beam as a measure of the effective depth of penetration. In the present study, 63.2% of the diffracted beam was chosen because the absorption of X-rays follows the response of a first order system. Moreover, at four times this depth, the maximum depth of penetration of the X-ray beam is reached.

Hence for CoKα radiation on steel, the linear coefficient of absorption is 470 cm^{-1} [16j]. For normal exposure, $\psi_0 = 0$ deg. and 310 reflection is at $2\eta \simeq 18.74$ deg. The effective depth of penetration can be computed as follows:

$$a = \frac{1}{\cos \psi_0} = 1, \quad b = \frac{1}{\cos (\psi_0 + 2\eta)} = 1.058,$$

and $(a+b) = 2.058$.

From equation (A1.4) we have:

$$\frac{I_{\bar{d}}}{I_{\bar{d}inf}} = 1 - e^{-963\bar{d}} .$$

Therefore $0.632 = 1 - 3^{-963\bar{d}}$,

that is $\bar{d} = 10.3\ \mu m$,

$= 4.06 \times 10^{-4}$ in.

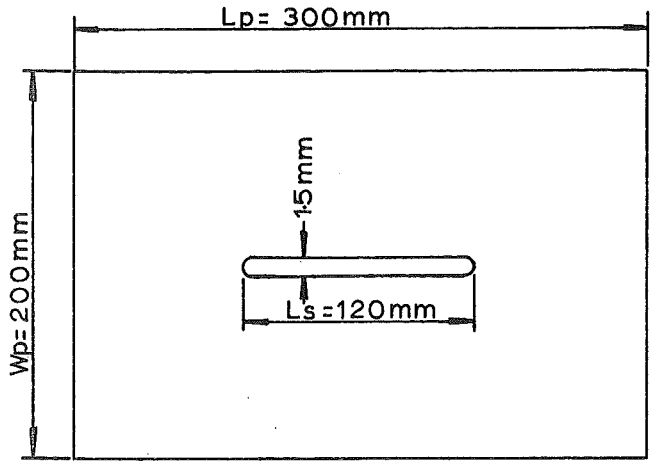

a. Straight Slit

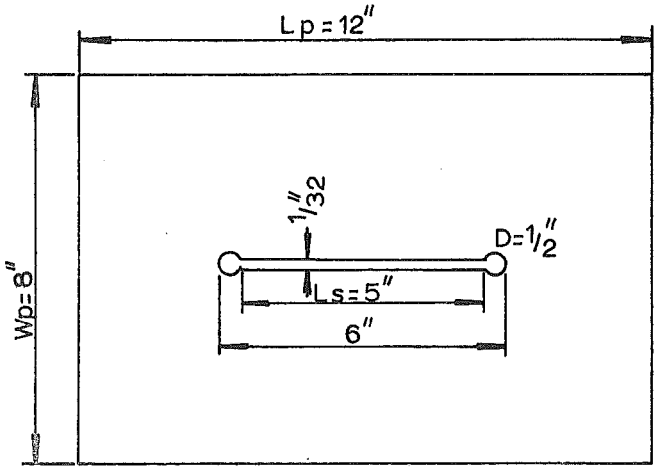

b. Straight Slit with Circular Holes at the Ends

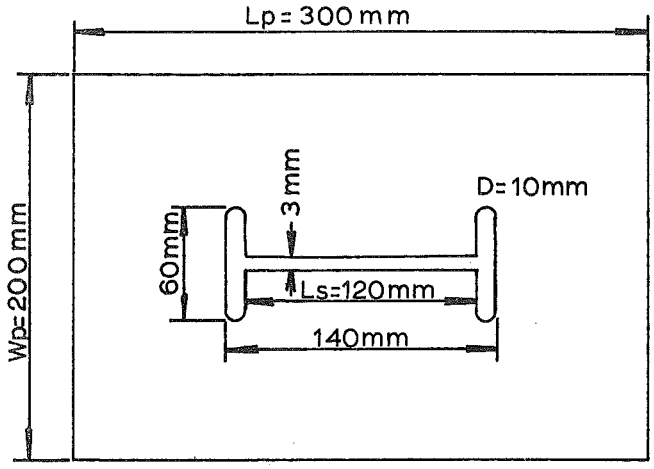

c. H-Type Slit

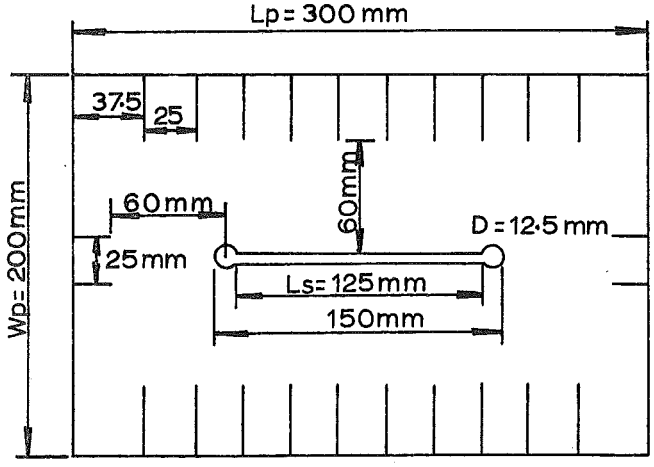

d. Lehigh-Type with Sawcuts(Sawcut width is 1mm)

Fig.A2·1 Self-restrained specimens[96].

APPENDIX 2

FINITE ELEMENT METHOD OF DEFINING THE DEGREE OF CONSTRAINT OF SELF-RESTRAINED BUTT JOINTS

In the present study, the restraining jig prevents out-of-plane distortion and locates the two parent plates in position during welding. However restraint against in-plane distortion is difficult to define with this set-up. Especially when the in-plane biaxial residual stress system is the main interest in plates of less than ½" thick, restraint applied in this plane is important.

The application of in-plane restraint can be effected in many ways. In some cases, in-plane distortion is restrained by welding the plates onto massive structures or backing plates prior to welding[8,9]. This method is rather wasteful and the in-plane degree of constraint is difficult to define. In other cases, self-restrained specimens are used. These self-restrained specimens can have various configurations as shown in Fig. A2.1. With these self-restrained specimens, considerable restraint in the plane of parent plates can be applied during welding. However, the measure of degree of constraint is difficult to obtain analytically in most cases.

In 1970, Masabuchi and Ich[96] successfully used the F.E.M. to obtain measure of degree of constraint of self-restrained plate of various configurations. Hence, it prompted the author to make similar study in the interest of future study on the effect of restraint on residual stress in weldments. By using such self-restrained specimens, positive restraint can be applied to the weld during welding and clamping is not

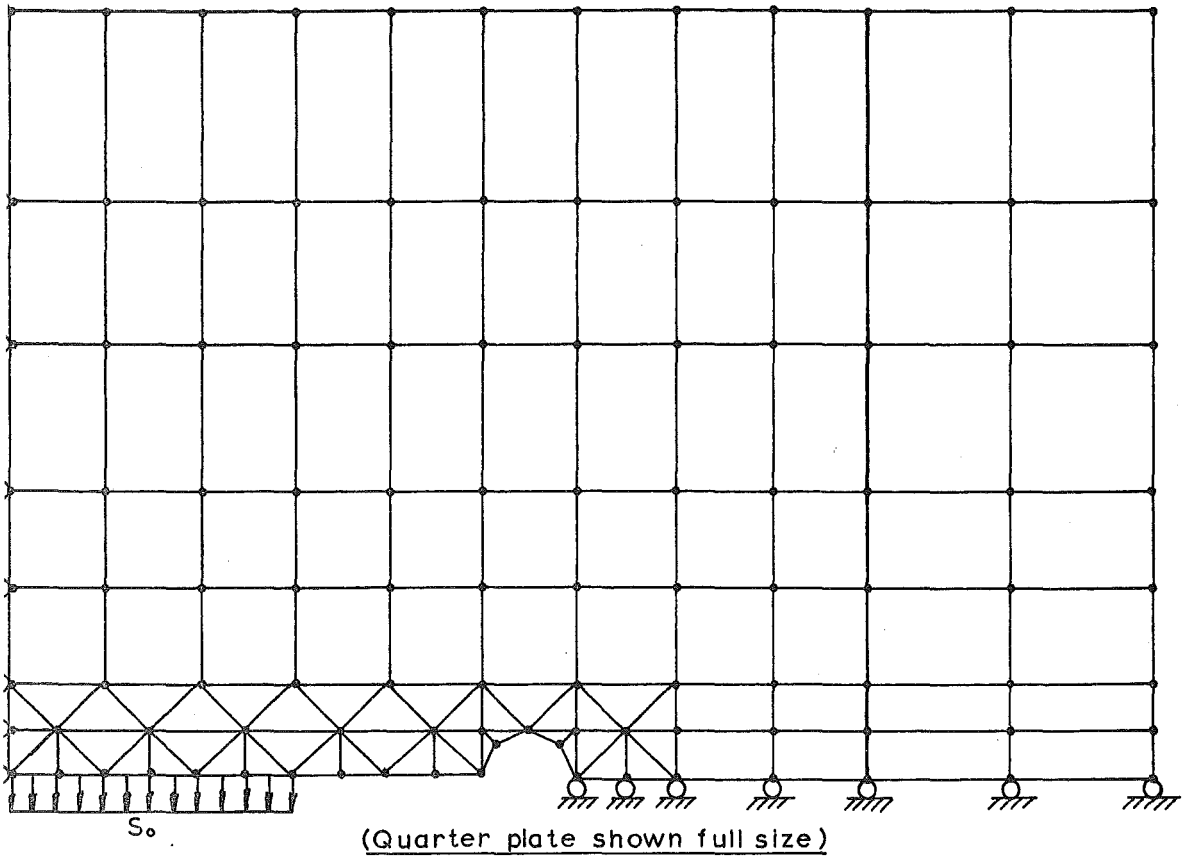

Fig.A2·2 Rectangular plate containing a straight slit with circular holes at the ends and the grid system.

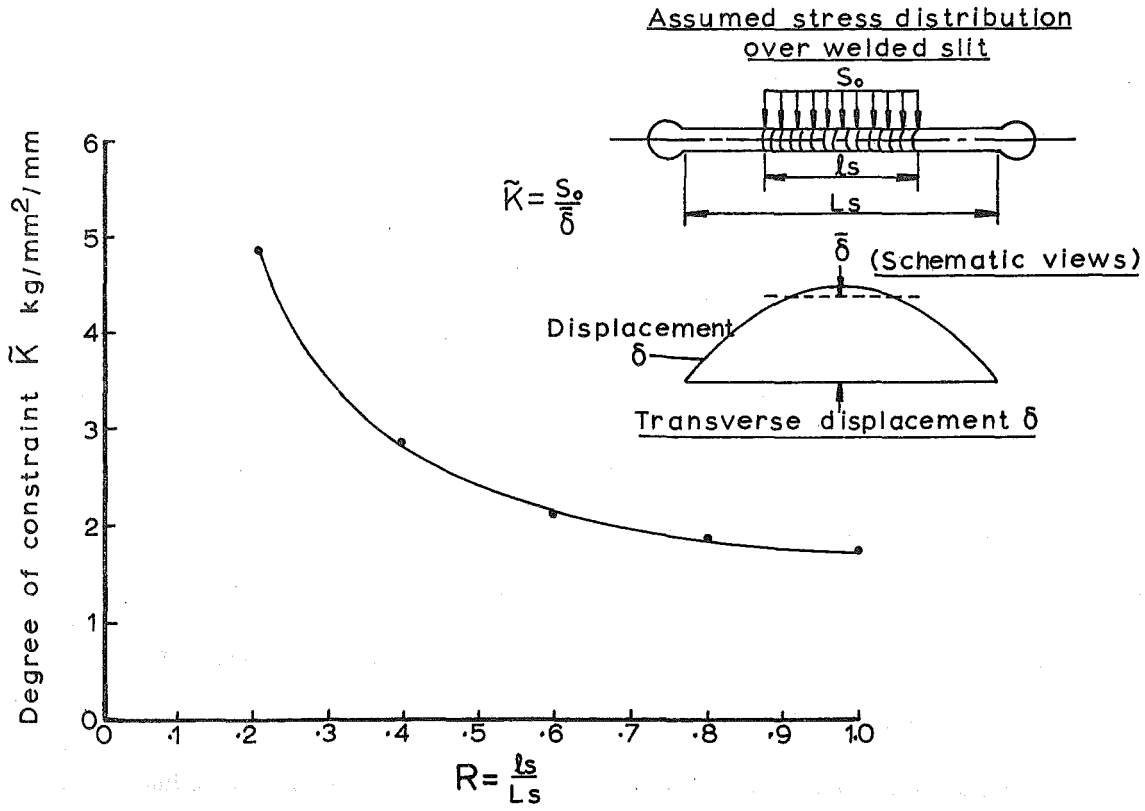

Fig.A2·3 Relationship between weld length to slit length ratio R, and the degree of constraint $\tilde{K}$.

necessary as out-of-plane distortion is not of interest.

In the study taken by the author, a specimen with a straight slit and circular holes at the end was used. This specimen was chosen because it is much simpler in geometry and easier to make. However, H-type slit and straight slit can be effectively studied by the present computer programme developed on the F.E.M. basis.

The grid network adopted for this specimen is shown in Fig. A2.2, and the results of the computer analysis on the degree of constraint with weld length are shown in Fig. A2.3. The results show good agreement with that published by Masabuchi and Ich.

The author suggests using this programme to compute the salient dimensions of a specific type of self-restrained specimens such that for a particular slit length Ls and weld length ℓs fixed, the dimensions of plates Lp and Wp can be varied so that the degree of constraint is different.

Hence by taking residual stress measurements on a series of specimens of different known degrees of constraint, the effect of restraint on residual welding stress can be studied for a fixed weld length and slit length. X-ray measurements can be conveniently taken off such specimens and the previous problem of obstruction by the clamps is alleviated.

The Finite Element Method is a numerical stress analysis technique which is described in detail in text[97]. The computer programme requires large storage area and must be run on a large computing system such as the IBM 360/44 which has auxiliary disk storage.

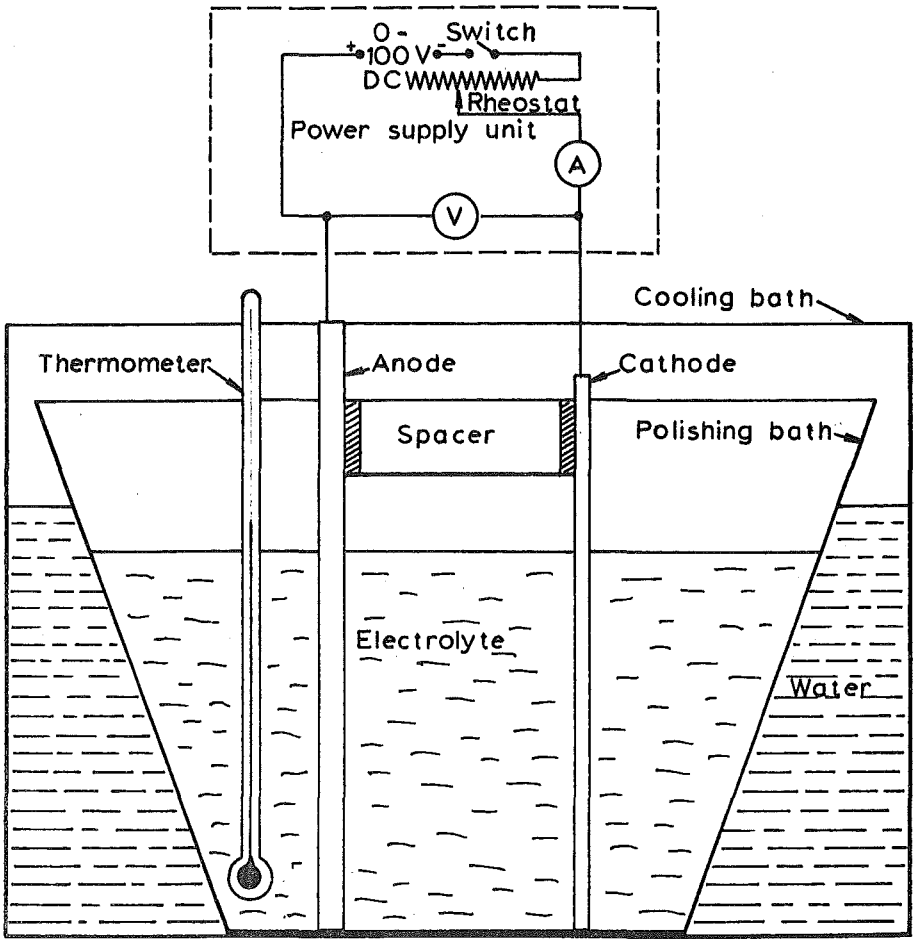

Fig. A3·1 Diagrammatic sketch of electropolishing apparatus.

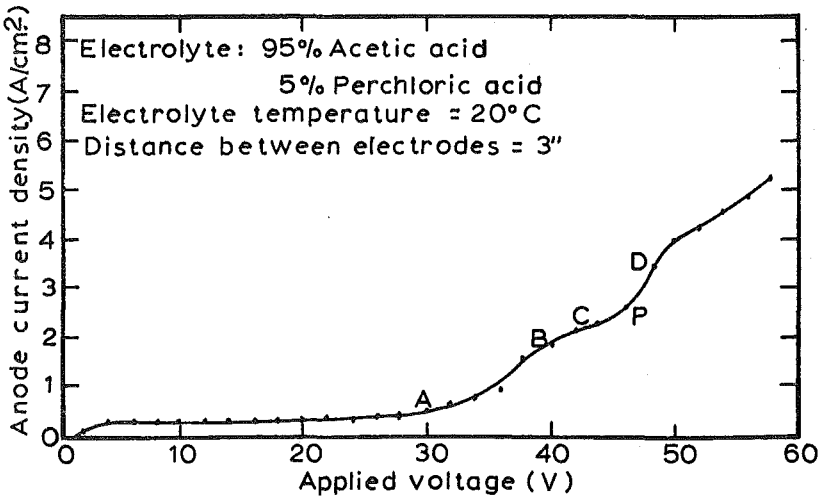

Fig. A3·2 Relation between cell voltage and anode current density when using a series circuit. Anodic process at region A-B etching ; B-C instability ; C-D polishing ; P indicates optimum polishing conditions.

APPENDIX 3

ELECTROPOLISHING PROCEDURE

A3.1 Introduction

The electropolishing (or in full electrolytic polishing) is a complex anodic process where a metal anode is etched or polished depending on the conditions of operation and the solution used. The process produces a smooth and bright finished surface. Furthermore, the process removes metals without inducing any strains on the remaining bulk metal. Hence the process is most suited for obtaining surfaces which are to be completely free from deformation produced by initial mechanical preparation. Details of the electropolishing process are described in text[78].

A3.2 Experimental Procedure

The set-up used in the present study is shown in Fig. A3.1. The power supply is provided by the Shandon Electropolisher power supply Type 6510 which is a separate unit from the Shandon Electropolisher. The two baths used are made of polythene which is inert to most acids. A stainless steel plate acts as the cathode.

The solution chosen for electropolishing low carbon steel is of the compositions:

95% Acetic acid (sp.gr. 1.065)

5% Perchloric acid (sp.gr. 1.60)

***Caution: Care must be taken when making solutions using Perchloric acid[78] which can be explosive.

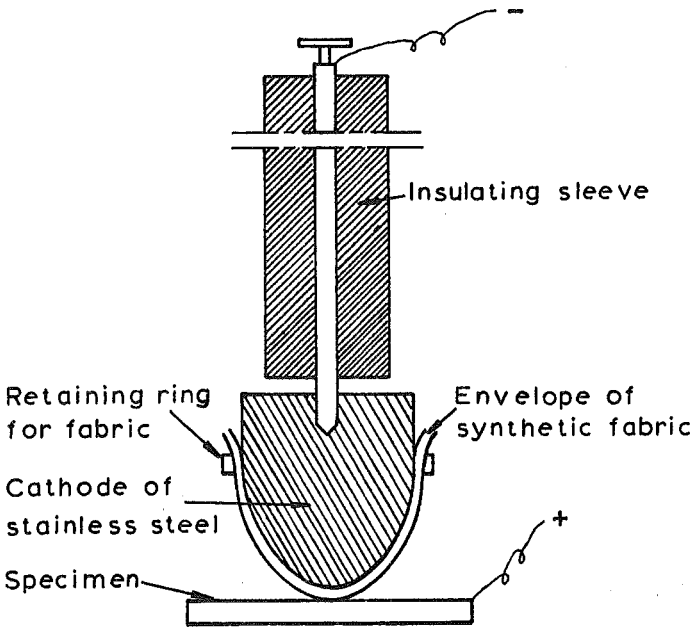

Fig.A3·3 Sketch of tampon for "Ellopol".[98]

The relation between the cell voltage and anode current was studied and the results are plotted in Fig. A3.2. It was found that polishing occurs at about 44v. and above. The higher the voltage reached, the faster the polishing takes place. It was also found that electroetching at 30v. also produces satisfactory surface which produces sharp reflection during X-ray measurements. Hence, all the specimens were electroetched under the following conditions:

Cathode:	Stainless-steel
Voltage:	30
Current density:	0.36 amps/cm^2
Time:	8 min.
Temperature:	20^oC

Moreover, it was found to simultaneously electropolish each welded plate at nine spots of 1 cm diameter, the current required would exceed the capacity of the power supply unit. About 0.002" in depth of metals were removed.

The masking of the surface not required to be prepared was effected by covering the whole surface with polythene insulation tape and cutting circular windows over the spots to be prepared.

A3.3 Discussion

The present procedure is rather cumbersome for applications on large specimens. Especially when using the present tank method, large volumes of dangerous solutions are involved. However, in 1957 Jacquet[98] introduced the 'tampon' technique which uses a metallic electrode surrounded by sheets of synthetic fibres which retain an appreciable quantity of

electrolyte (see Fig. A3.3). This electrode or tampon is rubbed over the surface to be polished. The results obtained by Jacquet showed the surface prepared is good enough for micro-examination.

This portable unit developed by Jacquet appears to be most promising for practical applications on large engineering structures on which X-ray stress measurements are to be taken. The author would propose developing this method for actual applications in future work.

APPENDIX 4

ABSORPTION FACTOR

The total energy reflected by an 'infinitely' thick flat specimen in the back reflection case (see Fig. A1.1) can be expressed by the equation (A1.3) as follows:

$$I = QI_0SA(\theta,\psi_0)$$

where Q = factors like temperature factor, angular factor, and others which affect the reflected X-ray intensity.

$A(\theta,\psi_0) = \frac{a}{(a+b)}$ is the absorption factor.

The specimen absorption factor $A(\theta,\psi_0)$ varies with diffraction angle and angle of incidence of the X-ray beam as follows:

$$A(\theta,\psi_0) = \frac{\cos\ (\psi_0+2\eta)}{\cos\ \psi_0 + \cos\ (\psi_0+2\eta)} \qquad (A4.1)$$

On expanding equation (A4.1) we have

$$A(\theta,\psi_0) = \frac{\cos\ (\psi_0+\eta)\cos\ \eta - \sin\ (\psi_0+\eta)\sin\ \eta}{\cos\ \psi_0 + \cos\ (\psi_0+2\eta)} \qquad (A4.2)$$

As $$\cos\ \psi_0 + \cos\ (\psi_0+2\eta) = \cos\ (\psi_0+\eta)\ \cos\ \eta, \qquad (A4.3)$$

therefore from equations (A4.2) and (A4.3) we have

$$A(\theta,\psi_0) = 1 - \tan\ (\psi_0+\eta)\ \tan\ \eta. \qquad (A4.4)$$

Since $90^{\circ}-\theta = \eta$ we have from equation (A4.4) the required form of the absorption factor:

$$A(\theta,\psi_0) = 1 - \tan\ (\psi_0+\eta)\ \cot\ \theta. \qquad (A4.5)$$

APPENDIX 5

PARABOLIC LEAST SQUARES FIT

Consider $\bar{n}$ equally spaced points on the peak of the $K\alpha_1$ line profile ($\bar{n}$ being an odd number). A parabolic curve can be fitted over these points and the axis of symmetry of the fitted parabola is taken as the measure of the peak position. The fitting of a parabolic curve over these experimental points can be effected by the least squares method described below.

From Fig. 5.5, take the measured point at $x = x_m$ which is closest to the apparent peak position as the reference point. From the general equation of a parabola, we have:

$$y = a(x-x_m)^2 + 2b(x-x_m) + c.$$

The axis of symmetry of the parabola lies at the point $x = x_m - 2b/a$. Hence, the objectives are to find the best estimates of the values of a and b.

The method of least squares can be applied where the sum of the squares of the error is to be a minimum. Thus

$$a(x_i-x_m)^2 + 2b(x_i-x_m) + c - y_i = F(a,b,c).$$

To find the values of a, b and c which will minimise $F(a,b,c)$ we obtain the partial derivatives $\partial F/\partial a$, $\partial F/\partial b$, and $\partial F/\partial c$ and set each to zero. Thus we have the following:

$$(1) \quad \Sigma y_i (x_i-x_m)^2 = a\Sigma(x_i-x_m)^4 + 2b\Sigma(x_i-x_m)^3 + c\Sigma(x_i-x_m)^2$$

$$(2) \quad \Sigma y_i (x_i-x_m) = a\Sigma(x_i-x_m)^3 + 2b\Sigma(x_i-x_m)^3 + c\Sigma(x_i-x_m)$$

$$(3) \quad \Sigma y_i = a\Sigma(x_i-x_m)^2 + 2b\Sigma(x_i-x_m) + \bar{n}c.$$

The above system of three homogeneous equations in three unknowns can be solved by the Cramer's Rule. From this we obtain:

$$a = \frac{\begin{vmatrix} \Sigma y_i (x_i - x_m)^2 & 2\Sigma (x_i - x_m)^3 & \Sigma (x_i - x_m)^2 \\ \Sigma y_i (x_i - x_m) & 2\Sigma (x_i - x_m)^2 & \Sigma (x_i - x_m) \\ \Sigma y_i & 2\Sigma (x_i - x_m) & \bar{n} \end{vmatrix}}{D}$$

$$b = \frac{\begin{vmatrix} \Sigma (x_i - x_m)^4 & \Sigma y_i (x_i - x_m)^2 & \Sigma (x_i - x_m)^2 \\ \Sigma (x_i - x_m)^3 & \Sigma y_i (x_i - x_m) & \Sigma (x_i - x_m) \\ \Sigma (x_i - x_m)^2 & \Sigma y_i & \bar{n} \end{vmatrix}}{D}$$

where D is the determinant of the system of three homogeneous equations. Hence the peak position of the $K\alpha_1$ line profile is obtained from the least squares method where a and b are the values which will minimise F(a,b,c). The peak position of the $K\alpha_1$ peak is $x = x_m - 2b/a$. The number of points used in the present study is $\bar{n} = 5$.

APPENDIX 6

TABLE 5-2(a)

EXPERIMENT: Calibration of Low Carbon Steel Tensile Specimen.

AREA OF CROSS-SECTION: 40.30 mm^2.

SURFACE PREPARATION: Abraded with fine emery paper and etched with 10% Nital.

CONDITION: Recovery annealed at 650°C for 1½ hr.

METHOD OF ANALYSIS: Data acquired at 0.25° intervals for computer analysis; optimised value of $K\alpha_2/K\alpha_1$ ratio used with the Fourier Method.

$\beta = 0°$

Load (kg)	ψ_o (deg)	Optimum $K\alpha_2/K\alpha_1$	% Misfit	Peak $K\alpha_1$ (deg)	Ibreadth $K\alpha_1$ (deg)	Imax $K\alpha_1$
100	0	0.4191	1.2422	161.0429	1.9087	30.44
100	35	0.4316	0.7081	161.2293	1.8172	26.88
200	0	0.4066	1.4530	161.0579	1.9426	30.97
200	35	0.4191	0.5407	161.1849	1.8698	26.79
300	0	0.4066	0.9805	161.1224	1.9736	30.66
300	35	0.4176	0.5772	161.1823	1.8353	26.97
400	0	0.4129	1.5966	161.1318	1.9187	31.55
400	35	0.4520	0.5320	161.1303	1.8210	27.15
500	0	0.4348	1.4030	161.1486	1.9695	30.65
500	35	0.4004	0.3091	161.0699	1.9921	26.31
600	0	0.3988	0.9172	161.1936	2.0241	31.08
600	35	0.4426	0.6972	161.0459	1.8260	26.86
700	0	0.3723	0.6861	161.1939	2.0491	31.06
700	35	0.4348	0.4559	160.9864	1.8995	26.61

TABLE 5-2(b)

EXPERIMENT: Calibration of Low Carbon Steel Tensile Specimen.

AREA OF CROSS-SECTION: 40.30 mm^2.

SURFACE PREPARATION: Abraded with fine emery paper and etched with 10% Nital.

CONDITION: Recovery annealed at 650°C for 1½ hr.

METHOD OF ANALYSIS: Data acquired at 0.25° intervals for computer analysis; assumed constant value for Kα2/Kα1 ratio is used with the Fourier Method.

$\beta = 0°$

Load (kg)	ψ_o (deg)	Assumed Kα2/Kα1	% Misfit	Peak Kα1 (deg)	Ibreadth Kα1 (deg)	Imax Kα1
100	0	0.5	2.1901	161.0395	1.8318	30.01
100	35	0.5	1.5298	161.2277	1.7478	26.68
200	0	0.5	2.4203	161.0522	1.8514	30.49
200	35	0.5	1.6749	161.1826	1.7856	26.55
300	0	0.5	2.0361	161.1180	1.8831	30.14
300	35	0.5	1.6731	161.1795	1.7498	26.75
400	0	0.5	2.7862	161.1254	1.8345	31.09
400	35	0.5	1.1221	161.1287	1.7736	26.99
500	0	0.5	2.0626	161.1422	1.9058	30.30
500	35	0.5	1.1778	161.0633	1.8865	25.95
600	0	0.5	1.9359	161.1870	1.9259	30.47
600	35	0.5	1.2026	161.0440	1.7679	26.69
700	0	0.5	1.8408	161.1860	1.9226	30.29
700	35	0.5	1.2975	160.9842	1.8335	26.38

TABLE 5-2(c)

EXPERIMENT: Calibration of Low Carbon Steel Tensile Specimen.

AREA OF CROSS-SECTION: 40.30 mm^2.

SURFACE PREPARATION: Abraded with fine emery paper and etched with 10% Nital.

CONDITION: Recovery annealed at 650°C for 1½ hr.

METHOD OF ANALYSIS: Data acquired at 0.1° intervals for computer analysis; optimised value for Kα2/Kα1 ratio is used with the Fourier Method.

$\beta = 0°$

Load (kg)	ψ_o (deg)	Optimum Kα2/Kα1	% Misfit	Peak Kα1 (deg)	Ibreadth Kα1 (deg)	Imax Kα1
100	0	0.4191	1.1993	161.0501	1.9095	30.48
100	35	0.4160	0.6801	161.2239	1.8310	26.96
200	0	0.4098	1.4738	161.0531	1.9380	30.96
200	35	0.4160	0.4838	161.1800	1.8645	26.90
300	0	0.3988	0.9317	161.1236	1.9791	30.73
300	35	0.4035	0.5858	161.1828	1.8463	27.04
400	0	0.4082	1.5958	161.1322	1.9191	31.61
400	35	0.4629	0.6099	161.1257	1.7974	27.27
500	0	0.4301	1.5740	161.1497	1.9638	30.82
500	35	0.4176	0.4386	161.0782	1.9547	26.26
600	0	0.4113	0.9407	161.1871	1.9978	31.10
600	35	0.4551	0.6881	161.0351	1.8121	26.81
700	0	0.3816	0.7799	161.1844	2.0330	31.08
700	35	0.4410	0.4761	161.0011	1.8880	26.64

TABLE 5-2(d)

EXPERIMENT: Calibration of Low Carbon Steel Tensile Specimen.

AREA OF CROSS-SECTION: 40.30 mm^2.

SURFACE PREPARATION: Abraded with fine emery paper and etched with 10% Nital.

CONDITION: Recovery annealed at 650°C for $1\frac{1}{2}$ hr.

METHOD OF ANALYSIS: Data acquired at 0.1° intervals for computer analysis; assumed constant value for $K\alpha_2/K\alpha_1$ ratio is used with the Fourier Method.

$\beta = 0°$

Load (kg)	ψ_o (deg)	Assumed $K\alpha_2/K\alpha_1$	% Misfit	Peak $K\alpha_1$ (deg)	Ibreadth $K\alpha_1$ (deg)	Imax $K\alpha_1$
100	0	0.5	2.1599	161.0470	1.8330	30.05
100	35	0.5	1.5381	161.2223	1.7453	26.70
200	0	0.5	2.5417	161.0491	1.8498	30.49
200	35	0.5	1.5988	161.1777	1.7767	26.66
300	0	0.5	2.1664	161.1192	1.8808	30.16
300	35	0.5	1.7648	161.1802	1.7448	26.78
400	0	0.5	2.7971	161.1244	1.8301	31.12
400	35	0.5	1.0641	161.1249	1.7613	27.14
500	0	0.5	2.2877	161.1443	1.8950	30.45
500	35	0.5	1.2674	161.0744	1.8699	25.95
600	0	0.5	1.7980	161.1821	1.9133	30.56
600	35	0.5	1.1137	161.0337	1.7667	26.69
700	0	0.5	1.8659	161.1762	1.9154	30.39
700	35	0.5	1.1879	160.9994	1.8283	26.44

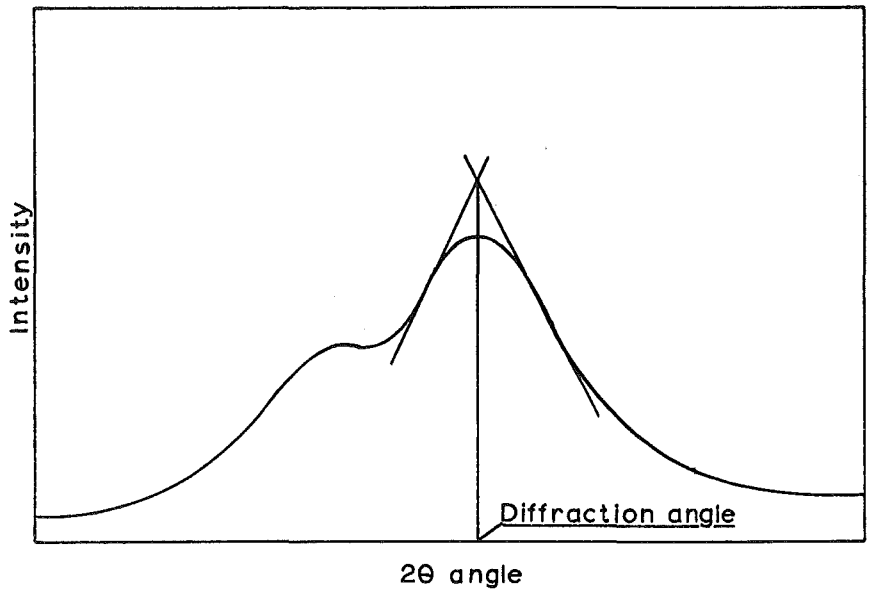

Fig. A7·2 Triangular method of determining diffraction angle.

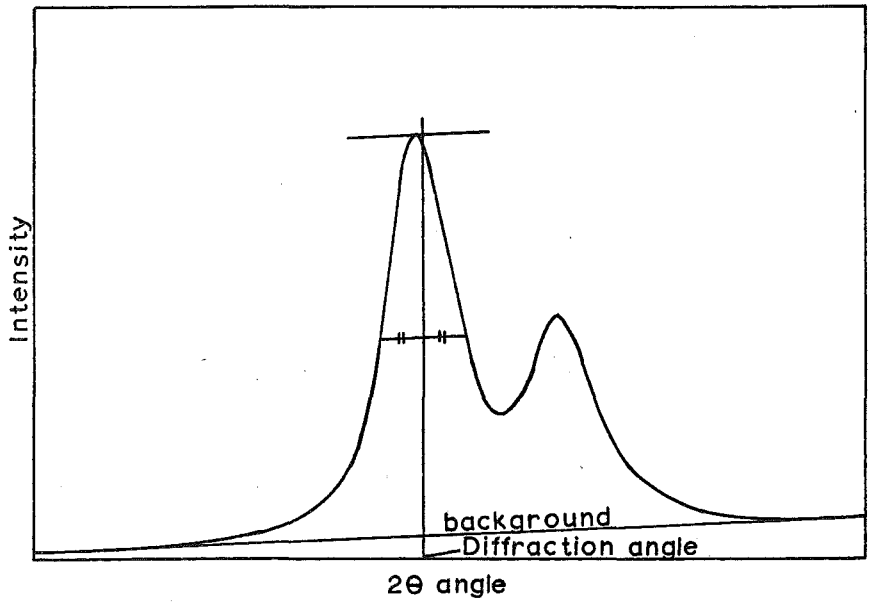

Fig. A7·1 Half peak method of determining diffraction angle.

APPENDIX 7

COMPARISON OF THE COMPUTER METHOD AND GRAPHICAL METHODS OF CHART ANALYSIS

A7.1 Introduction

The diffraction angle of the $K\alpha_1$ line profile can be measured by a number of methods as described below:

Graphical methods

(a) Half peak method: Locate the background, and then draw a line passing through the point of half the value of the peak in parallel with the background line. Regard the middle point of the half value width as the diffraction angle (see Fig. A7.1).

Note: This method can only be applied if the $K\alpha_1$ and $K\alpha_2$ peaks are distinct on the $K\alpha$ line profile.

(b) Triangular method: Draw rectilinear lines along the slopes on both sides of the diffraction profile. The intersection of the straight lines can be regarded as the diffraction angle (see Fig. A7.2).

Computer method

This numerical method is described in detail in section 5.3.

A7.2 Procedure

Two sets of graphical outputs were analysed. In the first set we have the outputs from the calibration experiment where $\beta = 0^{\circ}$ and the surface has been electropolished. The $K\alpha_1$ and $K\alpha_2$ peaks were distinct and thus three methods of chart analysis were used. The line widths of these outputs were uniform and the analysed results are shown in Table A7-1.

TABLE A7-1

Graphical Methods:	Triangular Method			Half peak Method		
Load (kg)	θ_1 (deg)	θ_2 (deg)	$\Delta\theta = \theta_1 - \theta_2$	θ_1 (deg)	θ_2 (deg)	$\Delta\theta = \theta_1 - \theta_2$
0	161.36	161.43	-0.07	161.38	161.44	-0.06
150	161.40	161.31	0.09	161.43	161.37	0.06
300	161.45	161.28	0.17	161.47	161.32	0.15
450	161.48	161.24	0.24	161.52	161.26	0.26
600	161.53	161.18	0.35	161.56	161.21	0.35
750	161.58	161.18	0.40	161.61	161.21	0.40
Computer Method				Ibreadth Kα1 (deg)		
0	161.36	161.41	-0.05	1.14		
150	161.40	161.32	0.08	1.13		
300	161.46	161.28	0.18	1.12		
450	161.49	161.23	0.26	1.11		
600	161.53	161.18	0.35	1.15		
750	161.58	161.16	0.42	1.12		

* Data from calibration experiment where $\beta = 0^\circ$ and the surface been electropolished.

TABLE A7-2

	Triangular Method			Computer Method			
Point	θ_1 (deg)	θ_2 (deg)	$\Delta\theta = \theta_1 - \theta_2$	θ_1 (deg)	θ_2 (deg)	$\Delta\theta = \theta_1 - \theta_2$	Ibreadth Kα1 (deg)
1	160.68	161.32	-0.64	160.59	161.22	-0.63	2.28
2	161.18	161.32	-0.14	161.16	161.31	-0.15	1.89
3	161.25	161.29	-0.04	161.25	161.31	-0.06	1.34
4	161.12	161.31	-0.19	161.10	161.31	-0.21	1.38
5	161.12	161.32	-0.20	161.13	161.30	-0.17	1.40
6	161.13	161.36	-0.23	161.12	161.36	-0.24	1.25
7	161.01	161.24	-0.23	161.03	161.25	-0.22	1.28
8	161.20	161.31	-0.11	161.13	161.31	-0.18	1.34
9	161.05	161.48	-0.43	161.04	161.49	-0.45	1.28

* Data from specimen No. 5 after welding. ($\beta = 45^\circ$)

In the second set, the graphical outputs from measurements on specimen No. 5 in the direction $\beta = 45^{o}$ were analysed. The diffraction profiles were broad and the $K\alpha_1$ and $K\alpha_2$ peaks were not distinct in some of the cases. Only the triangular method was used to determine the diffraction angles graphically from these data. The analysed results are shown in Table A7-2.

A7.3 Discussion and Conclusions

From Table A7-1 it can be seen that the absolute value of the diffraction angles obtained by the triangular method and the computer method agreed satisfactorily. However, the half peak method shows results which deviate from this. This is due to the arbitrary nature of the measure of diffraction angle defined in the half peak method. The relative changes in the diffraction angle $\Delta\theta$ used in the calculation of stress show a maximum deviation of 0.02 deg., which is equivalent to 1 kg/mm^2, amongst the results obtained graphically and numerically. This was thought to be satisfactory in view of the precision attained in the calibration experiment where a maximum deviation from the least squares line (for case $\beta = 0^{o}$ as shown in Fig. 6.6) is about 1 kg/mm^2.

From Table A7-2, the diffraction angles determined graphically deviate significantly from those analysed numerically for cases where the diffraction profiles were broad. This is due to the effects of correcting the broad diffraction profiles for LPA factors and separating the $K\alpha_2$ component from the $K\alpha$ line profiles when analysing the data numerically, whereas these corrections were neglected when analysing the data graphically. However, the relative changes in diffraction angles $\Delta\theta$ were shown to agree satisfactorily for both numerical

and graphical methods. With the exception of point 8, the maximum deviation in $\Delta\theta$ as obtained by both methods shows the same order of magnitudes as before, that is, about 0.02^{o} ($\equiv$ 1 kg/mm^2).

Regarding point 8, it was found that the diffraction angle at $\psi_0 = 0^{o}$ showed significant deviation even though the width is narrow. On closer examination of the particular output it was found that the slopes on both sides of the $K\alpha_1$ peak vary continuously such that the drawing of a straight line on the slope is suspect. It ought to be remarked that many of the graphical outputs showed such feature which makes the graphical method suspect; especially when the diffraction profiles were as broad as those shown in the example in Fig. 6.1.

Hence, it can be concluded that under the conditions of uniform and sharp diffraction profiles, the graphical method can produce results which agree satisfactorily with results obtained numerically. However, under the conditions where the diffraction profiles were diffused and non-uniform, much uncertainty was experimenced when using the graphical methods. The numerical method can always be relied upon when the diffraction profiles were broad. The limit on the accuracy of the numerical method lies on the raw data itself. Hence, further improvement on the accuracy of X-ray stress measurements must be looked at in the direction of improving the capability of the measuring instruments.

APPENDIX 8

TABLE 6-1

EXPERIMENT: X-ray Study on the Effects of Surface Preparations on the Surface Layer of a Polycrystalline Material.

MATERIAL: 0.19% C Low Carbon Steel.

CONDITION: Recovery annealed at 650°C for ½ hr.

SURFACE PREPARATION: Initial surface preparation is M/C ground with coolant; M/C ground with a 46 grit wheel; 0.005" cuts.

THICKNESS OF SPECIMEN: 0.124".

$\beta = 90°$

SURFACE PREPARATION	Assumed $K\alpha_2/K\alpha_1$	t (inch)	ψ_o (deg)	Peak $K\alpha_1$ (deg)	Ibreadth $K\alpha_1$ (deg)
M/C ground	0.5	0.124	0	161.6244	2.5345
M/C ground	0.5	0.124	35	161.4745	2.5066
Abraded 240 emery paper	0.5	0.123	0	160.9170	2.7626
Abraded 240 emery paper	0.5	0.123	35	161.3029	2.0909
Abraded 640 emery paper	0.5	0.122	0	160.9231	2.1609
Lapped 1μm diamond dust	0.5	0.120	0	160.9464	1.8240
Lapped 1μm diamond dust	0.5	0.118	0	160.9933	1.8021
Lapped 1μm diamond dust	0.5	0.118	35	161.3559	1.6040
Electropolished at 30v	0.5	0.116	0	161.8154	1.4134
Electropolished at 30v	0.5	0.116	35	161.3655	1.3785
Electropolished at 45v	0.5	0.114	0	161.7497	1.3474
Electropolished at 45v	0.5	0.114	35	161.3377	1.2299
STARTING WITH A NEW SPECIMEN SIMILAR TO THE ABOVE ONE. INITIAL THICKNESS = 0.124"; SURFACE IS M/C SURFACE GROUND AS BEFORE.					
Electropolished at 40v	0.5	0.122	0	161.8398	1.6153
Electropolished at 40v	0.5	0.122	35	161.4082	1.6074
Electropolished at 40v	0.5	0.120	0	161.8754	1.5065
Electropolished at 40v	0.5	0.120	35	161.3537	1.4782

APPENDIX 9

TABLE 6-2(a)

EXPERIMENT: Calibration of Low Carbon Steel Tensile Specimen.

AREA OF CROSS-SECTION: 40.30 mm^2.

SURFACE PREPARATION: Abraded and etched with 10% Nital.

CONDITION: Recovery annealed at 650°C for 1½ hr.

$\beta = 0°$

Load (kg)	ψ_o (deg)	Optimum $K\alpha_2/K\alpha_1$	Peak $K\alpha_1$ (deg)	Ibreadth $K\alpha_1$ (deg)	tan $2\theta\psi=0°$	$\Delta\tan 2\theta\psi/\Delta\sin^2\psi$
200	0	0.4113	161.0565	1.9522	-0.343225	0.009947
200	35	0.3973	161.2922	1.8817	-	-
400	0	0.3926	161.1118	1.9567	-0.342218	0.002686
400	35	0.4254	161.1756	1.8559	-	-
600	0	0.4223	161.1706	1.9343	-0.340904	-0.003594
600	35	0.4191	161.0851	1.8399	-	-
800	0	0.3879	161.2326	1.9841	-0.339553	-0.009026
800	35	0.4723	161.0175	1.8052	-	-
1000	0	0.4535	161.2490	1.9196	-0.339144	-0.012420
1000	35	0.4410	160.9527	1.8059	-	-

Sample Calculations of X-ray Elastic Constant

From equation (4.17) we have for the surface stress σ_φ in the direction of measurements:

$$\sigma_\varphi = \Omega \cdot \frac{E}{1+\nu} \cdot \frac{\Delta \tan 2\theta_\psi}{\Delta \sin^2 \psi} \qquad \text{(A9.1)}$$

where $$\Omega = -\frac{\cot \theta_o (1 - 2\sin^2\theta_o)^2}{2} \qquad \text{(A9.2)}$$

By differentiating equation (A9.1) we have

$$\Omega \cdot \frac{\partial \Delta \tan 2\theta\psi / \Delta \sin^2\psi}{\partial \sigma\varphi} = \frac{1+\nu}{E} \qquad \text{(A9.3)}$$

Rewriting equation (A9.3) we have

$$\frac{\partial \sigma\varphi}{\partial \Delta \tan 2\theta\psi / \Delta \sin^2\psi} = \Omega \cdot \frac{E}{1+\nu}$$

$$= K \text{ the X-ray stress constant.} \qquad \text{(A9.4)}$$

From equations (4.14) and (4.6) we have for $\psi = 0°$ and under uniaxial stress case:

$$\Omega.(\tan 2\theta_{\psi=0°} - \tan 2\theta_o) = -\frac{\nu\sigma\varphi}{E} \qquad \text{(A9.5)}$$

Hence by differentiating equation (A9.5) we have

$$\Omega \cdot \frac{\partial \tan 2\theta_{\psi=0°}}{\partial \sigma\varphi} = -\frac{\nu}{E} \qquad \text{(A9.6)}$$

Also from the intercept of the least squares line $\tan 2\theta_{\psi=0°}$ vs. $\Delta \tan 2\theta\psi / \Delta \sin^2\psi$ we have $\tan 2\theta_o$; that is the strain free condition.

Therefore from Table 6-2(a) we have by the least squares method (programmed in the Hewlett Packard Calculator) the following:

From $\tan 2\theta_{\psi=0°}$ vs. $\Delta \tan 2\theta\psi / \Delta \sin^2\psi$ we have from the intercept

$\tan 2\theta_o = 0.341563$; that is $\theta_o \simeq 80.57$.

Substituting θ_o into equation (A9.2) we have

$$\Omega = -0.074366$$

From equation (A9.3) we have

$$\frac{1+\nu}{E} = 84.58 \times 10^{-6} \text{ mm}^2/\text{kg}.$$

From equation (A9.6) we have

$$-\frac{\nu}{E} = -17.02 \times 10^{-6} \text{ mm}^2/\text{kg}.$$

Hence we have $E = 14802 \text{ kg/mm}^2$ and $\nu = 0.25$.

From equation (A9.4) we have $K = -879.3 \text{ kg/mm}^2$.

TABLE 6-2(b)

EXPERIMENT: Calibration of Low Carbon Steel Tensile Specimen.

AREA OF CROSS-SECTION: 38.00 mm^2.

SURFACE PREPARATION: Electropolished.

CONDITION: Recovery annealed at 650°C for 1½ hr.

$\beta = 0°$

Load (kg)	ψ_o (deg)	Optimum $K\alpha_2/K\alpha_1$	Peak $K\alpha_1$ (deg)	Ibreadth $K\alpha_1$ (deg)	tan $2\theta_{\psi=0°}$	$\Delta \tan 2\theta_\psi / \Delta \sin^2\psi$
0	0	0.4863	161.3592	1.1374	-0.337330	0.002317
0	35	0.4301	161.4142	1.1152	-	-
150	0	0.5254	161.3963	1.1310	-0.336526	-0.003171
150	35	0.3863	161.3209	1.1258	-	-
300	0	0.5160	161.4620	1.1185	-0.335133	-0.007693
300	35	0.4066	161.2788	1.1087	-	-
450	0	0.5098	161.4862	1.1113	-0.334585	-0.010745
450	35	0.4223	161.2301	1.1065	-	-
600	0	0.5020	161.5345	1.1510	-0.333542	-0.014913
600	35	0.4343	161.1786	1.0987	-	-
750	0	0.5129	161.5808	1.1227	-0.332575	-0.017671
750	35	0.4316	161.1587	1.1540	-	-

TABLE 6-2(c)

AREA OF CROSS-SECTION: 39.75 mm^2.

$\beta = 45°$

Load (kg)	ψ_o (deg)	Optimum $K\alpha_2/K\alpha_1$	Peak $K\alpha_1$ (deg)	Ibreadth $K\alpha_1$ (deg)	tan $2\theta_{\psi=0°}$	$\Delta \tan 2\theta_\psi / \Delta \sin^2\psi$
0	0	0.5191	161.3579	1.1997	-0.337370	0.000585
0	35	0.5160	161.3718	1.1286	-	-
150	0	0.5395	161.3633	1.1721	-0.337260	0.000370
150	35	0.5098	161.3721	1.1398	-	-

TABLE 6-2(c) Continued next page.

Load (kg)	ψ_o (deg)	Optimum $K\alpha_2/K\alpha_1$	Peak $K\alpha_1$ (deg)	Ibreadth $K\alpha_1$ (deg)	tan $2\theta\psi=0°$	$\Delta\tan 2\theta\psi/\Delta\sin^2\psi$
300	0	0.5535	161.4039	1.1904	-0.336365	-0.003659
300	35	0.5066	161.3169	1.1397	-	-
450	0	0.5535	161.4635	1.1759	-0.335092	-0.008169
450	35	0.5113	161.2689	1.1522	-	-
600	0	0.5410	161.5200	1.2101	-0.333886	-0.012450
600	35	0.5348	161.2231	1.1421	-	-
750	0	0.5238	161.5631	1.1893	-0.332951	-0.016367
750	35	0.5113	161.1723	1.1878	-	-

TABLE 6-2(d)

AREA OF CROSS-SECTION: 39.63 mm^2.

$\beta=90°$

Load (kg)	ψ_o (deg)	Optimum $K\alpha_2/K\alpha_1$	Peak $K\alpha_1$ (deg)	Ibreadth $K\alpha_1$ (deg)	tan $2\theta\psi=0°$	$\Delta\tan 2\theta\psi/\Delta\sin^2\psi$
0	0	0.5129	161.2906	1.1875	-0.338664	0.001478
0	35	0.4910	161.3257	1.1945	-	-
150	0	0.5238	161.3028	1.2185	-0.338408	-0.000722
150	35	0.4785	161.2856	1.2320	-	-
300	0	0.5176	161.3297	1.2289	-0.337792	-0.004275
300	35	0.4816	161.2280	1.1998	-	-
450	0	0.5738	161.3690	1.1630	-0.336956	-0.007038
450	35	0.4566	161.2014	1.1635	-	-
600	0	0.5207	161.4508	1.2069	-0.335257	-0.011287
600	35	0.4566	161.1817	1.1798	-	-
750	0	0.5629	161.4866	1.2321	-0.334443	-0.015926
750	35	0.4426	161.1064	1.1852	-	-

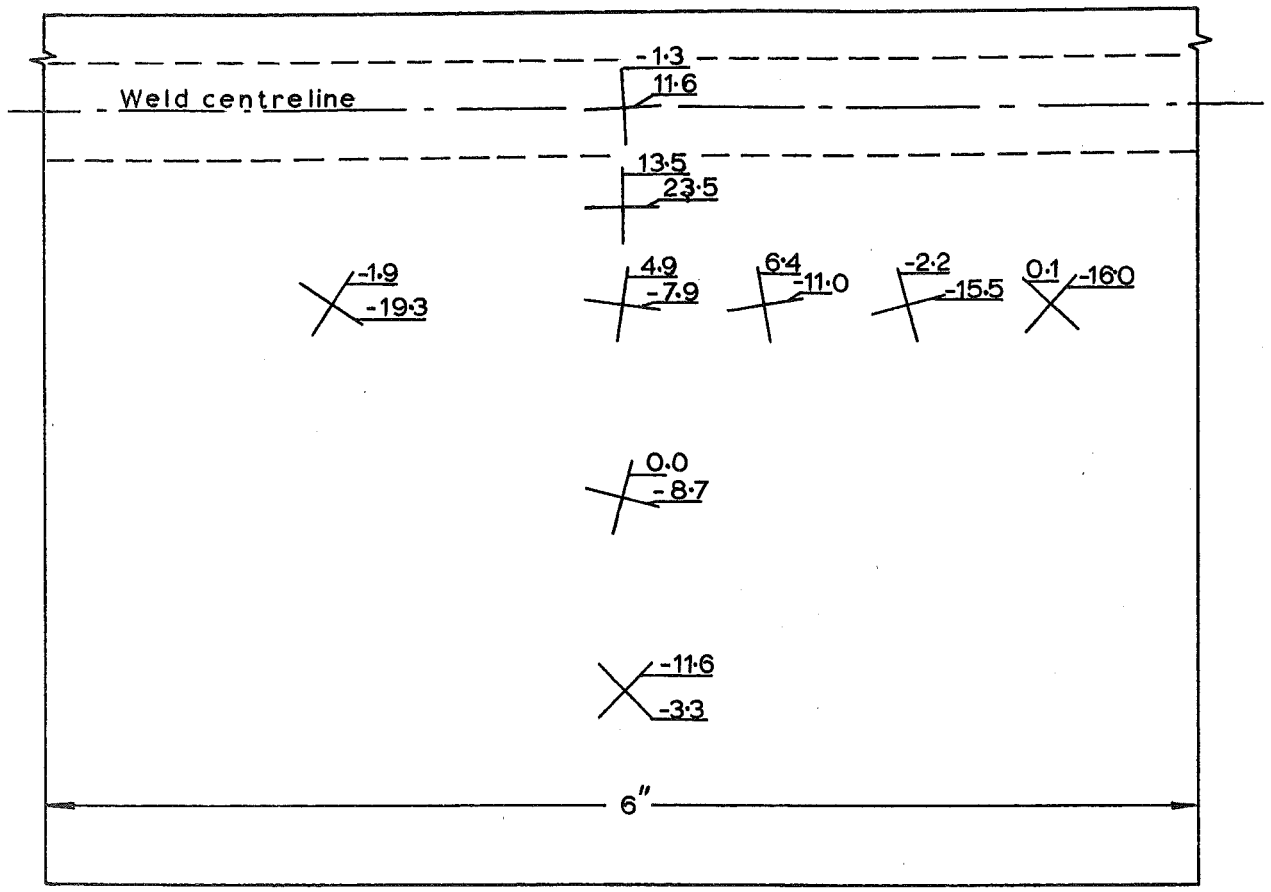

(b)

Principal stresses in a machine-welded plate.(kg/mm^2).
(specimen No.1)

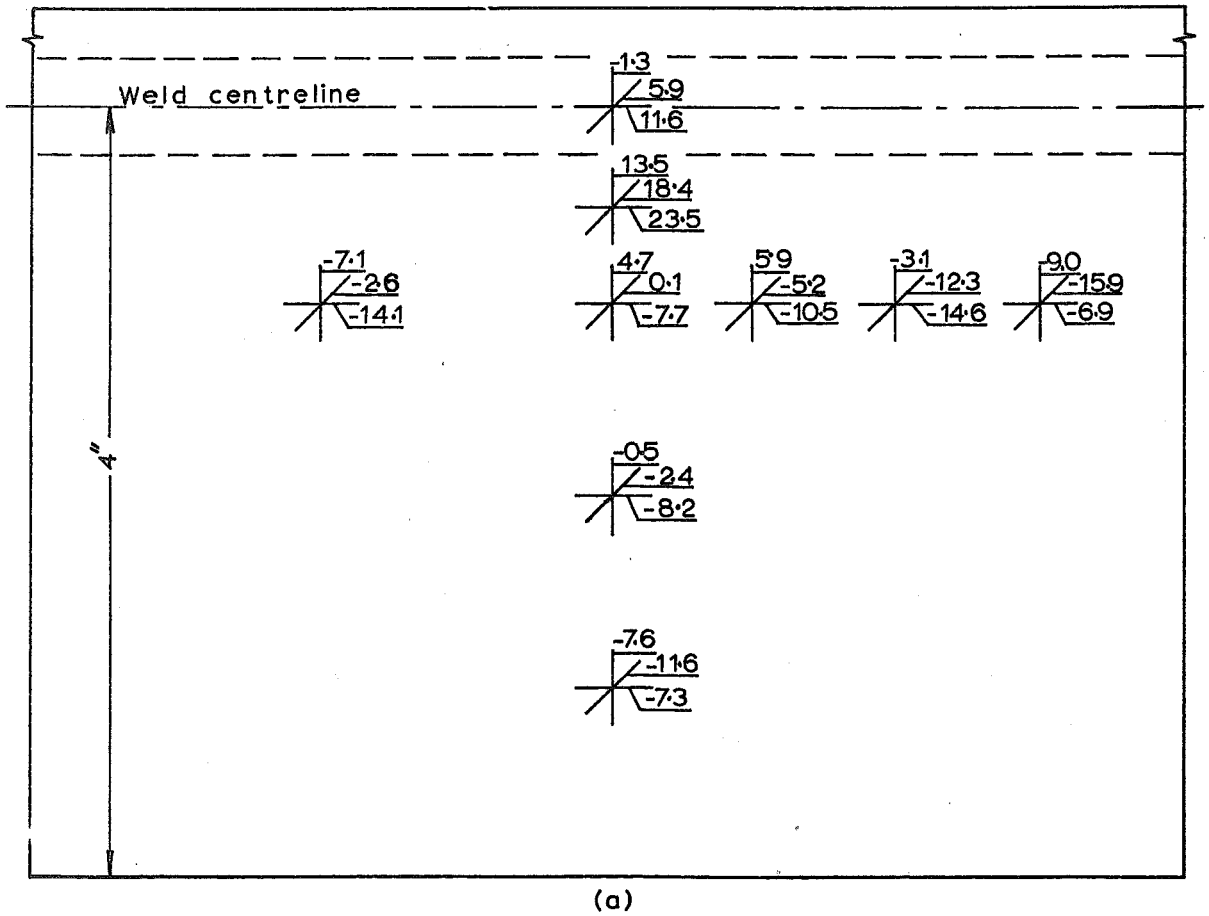

(a)

Fig.7·2 Residual stresses in a machine-welded plate.(kg/mm^2).
(single-vee weld using short-circuiting arc method)

APPENDIX 10

TABLES FOR RESIDUAL STRESS MEASUREMENTS ON WELDED PLATES.

TABLE 7-1

SPECIMEN No. 1

EDGE PREPARATION: Single Vee Notched.

WELDING TECHNIQUE: Short Circuiting Transfer.

SURFACE PREPARATION: Electropolished.

Point	$\sigma_{\beta=0°}$	$\sigma_{\beta=45°}$	$\sigma_{\beta=90°}$	σ_{max}	σ_{min}	$\theta_p°$
1	11.57	5.92	-1.28	11.62	-1.33	3.44
2	23.49	18.38	13.48	23.49	13.48	-0.60
3	-7.67	0.07	4.66	4.86	-7.86	-7.17
4	-8.23	-2.40	-0.45	0.01	-8.69	-13.25
5	-7.28	-11.58	-7.61	-3.31	-11.58	-43.86
6	-14.62	-12.25	-3.10	-2.18	-15.54	15.24
7	-14.11	-2.64	-7.07	-1.90	-19.28	-33.06
8	-10.52	-5.24	5.85	6.35	-11.02	9.77
9	-6.86	-15.88	-8.96	0.13	-15.95	-41.25

*stresses are in kg/mm^2 unit.

The residual stress pattern is plotted in Fig. 7.2(a).

and the principal stress pattern is plotted in Fig. 7.2(b).

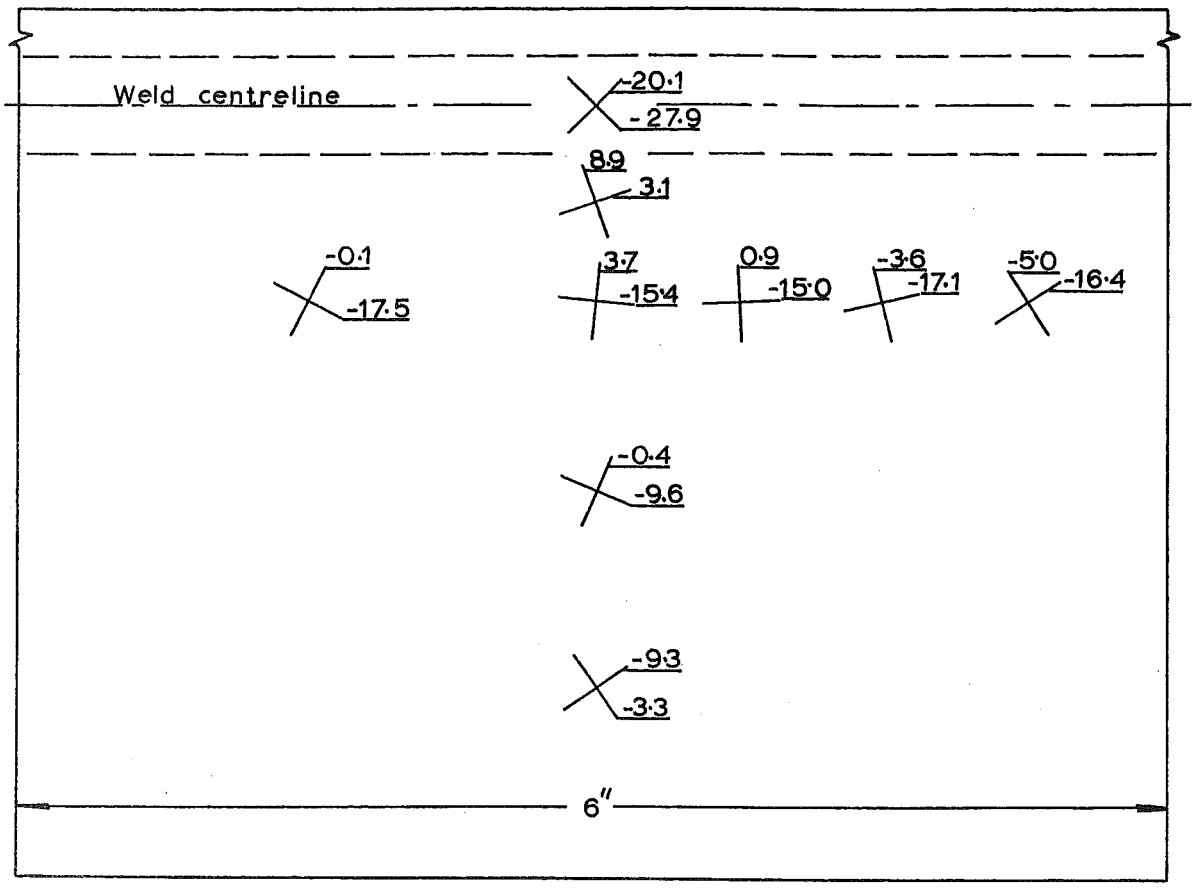

(b)

Principal stresses in a machine-welded plate.(kg/mm^2).
(specimen No.2)

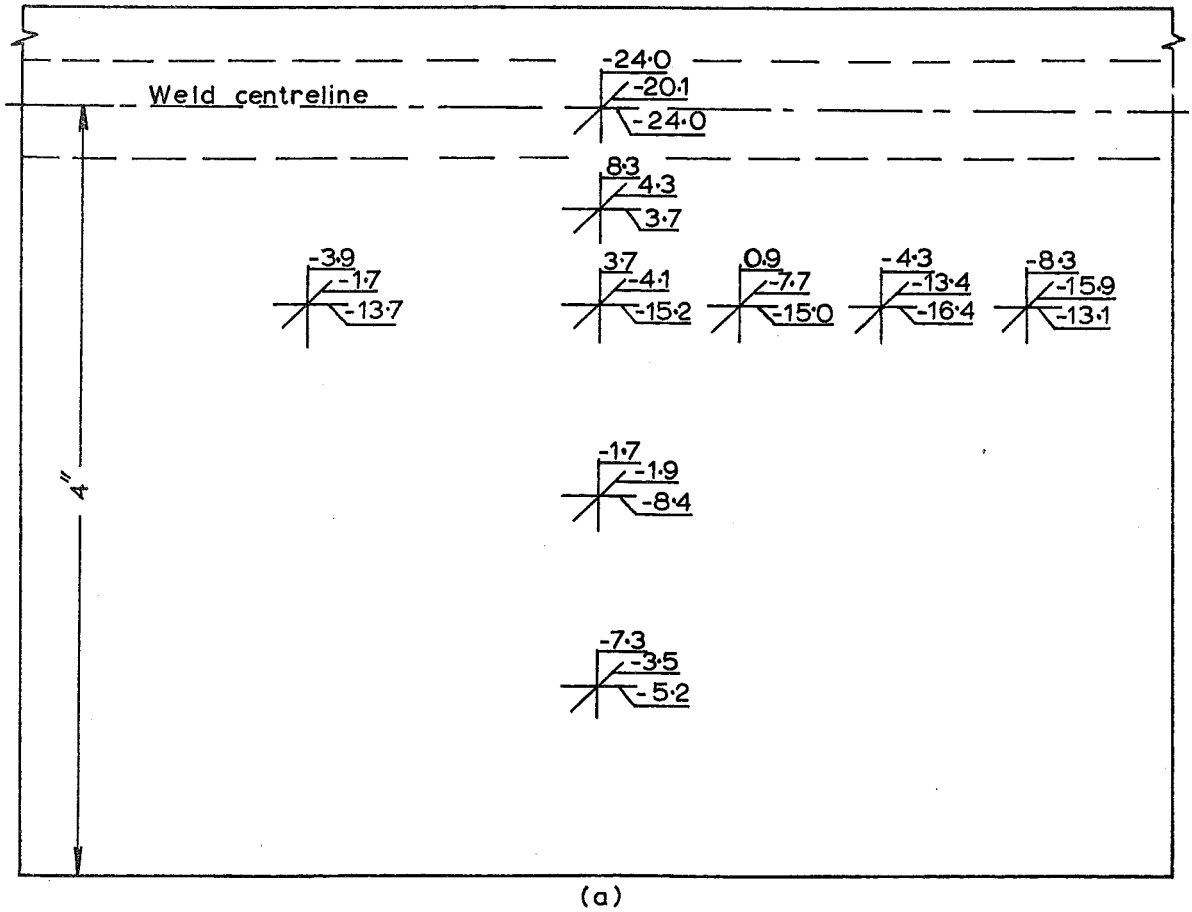

(a)

Fig.7·3 Residual stresses in a machine-welded plate.(kg/mm^2).
(single-vee weld using spray arc method)

TABLE 7-2

SPECIMEN No. 2

EDGE PREPARATION: Single Vee Notched.

WELDING TECHNIQUE: Spray arc Transfer.

SURFACE PREPARATION: Electropolished.

Point	$\sigma_{\beta=0°}$	$\sigma_{\beta=45°}$	$\sigma_{\beta=90°}$	σ_{max}	σ_{min}	θ_p°
1	-24.00	-20.10	-23.98	-20.10	-27.88	-44.93
2	3.70	4.27	8.31	8.89	3.12	18.48
3	-15.24	-4.05	3.47	3.65	-15.42	-5.55
4	-8.37	-1.85	-1.68	-0.41	-9.64	-21.75
5	-5.24	-3.45	-7.28	-3.27	-9.25	35.02
6	-16.39	-13.37	-4.31	-3.60	-17.10	13.28
7	-13.73	-1.68	-3.88	-0.14	-17.47	-27.67
8	-15.01	-7.74	0.86	0.89	-15.04	2.40
9	-13.11	-15.89	-8.28	-4.97	-16.42	32.53

*stresses are in kg/mm^2 unit.

The residual stress pattern is plotted in Fig. 7.3(a).

and the principal stress pattern is plotted in Fig. 7.3(b).

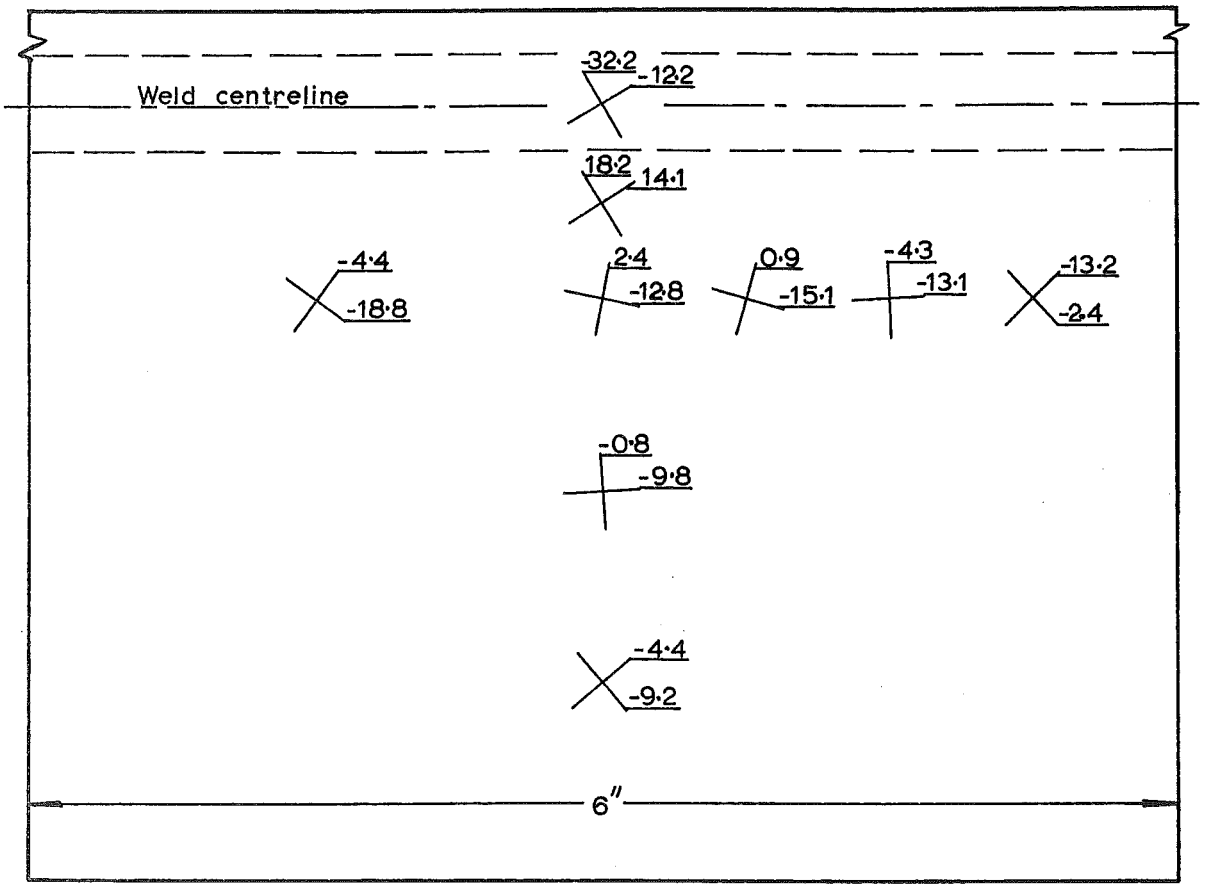

(b)

Principal stresses in a machine-welded plate.(kg/mm^2).
(specimen No.3)

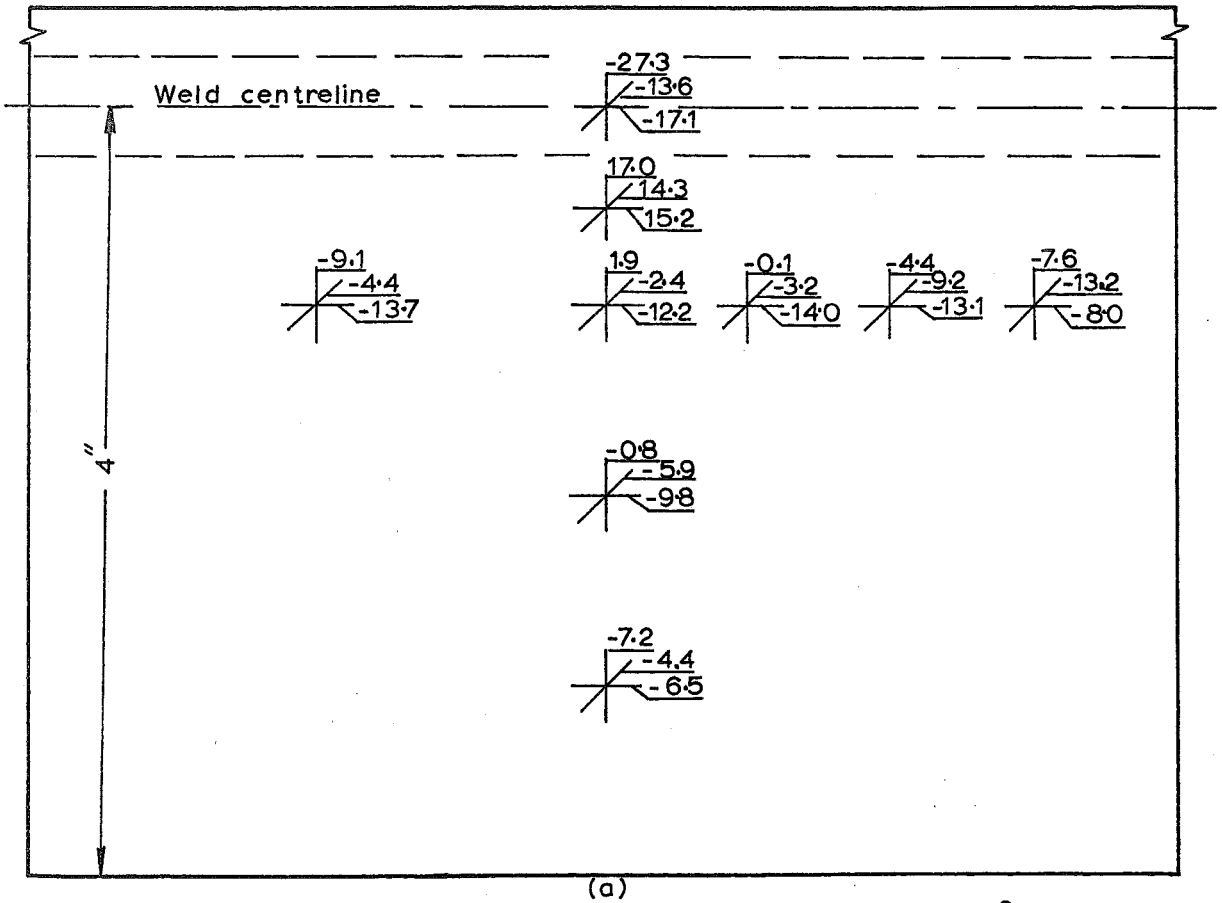

(a)

Fig.7.4 Residual stresses in a machine-welded plate.(kg/mm^2).
(double-vee weld using spray arc method)

TABLE 7-3

SPECIMEN No. 3

EDGE PREPARATION: Double Vee Notched.

WELDING TECHNIQUE: Spray arc Transfer.

SURFACE PREPARATION: Electropolished.

Point	$\sigma_{\beta=0^\circ}$	$\sigma_{\beta=45^\circ}$	$\sigma_{\beta=90^\circ}$	σ_{max}	σ_{min}	θ°_p
1	-17.13	-13.61	-27.30	-12.22	-32.21	-29.71
2	15.24	14.30	17.03	18.18	14.09	32.00
3	-12.24	-2.44	1.91	2.42	-12.75	-10.53
4	-9.78	-5.92	-0.81	-0.77	-9.82	3.97
5	-6.45	-4.40	-7.16	-4.37	-9.24	40.80
6	-13.06	-9.20	-4.35	-4.32	-13.09	3.24
7	-13.70	-4.39	-9.14	-4.03	-18.81	-36.02
8	-14.04	-3.21	-0.14	0.87	-15.05	-14.59
9	-7.96	-13.15	-7.62	-2.43	-13.15	44.09

*stresses are in kg/mm^2 unit.

The residual stress pattern is plotted in Fig. 7.4(a).

and the principal stress pattern is plotted in Fig. 7.4(b).

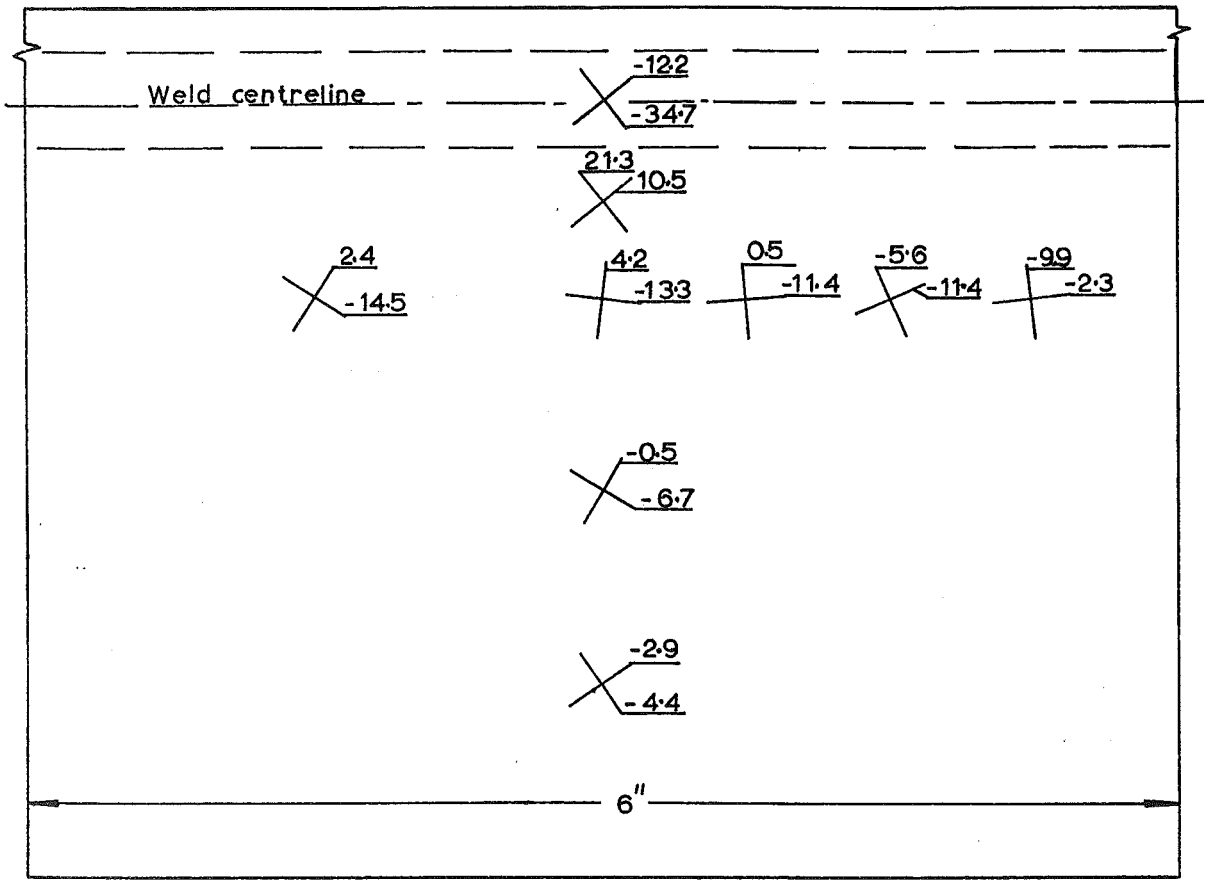

(b)

Principal stresses in a machine-welded plate.(kg/mm^2). (specimen No.4)

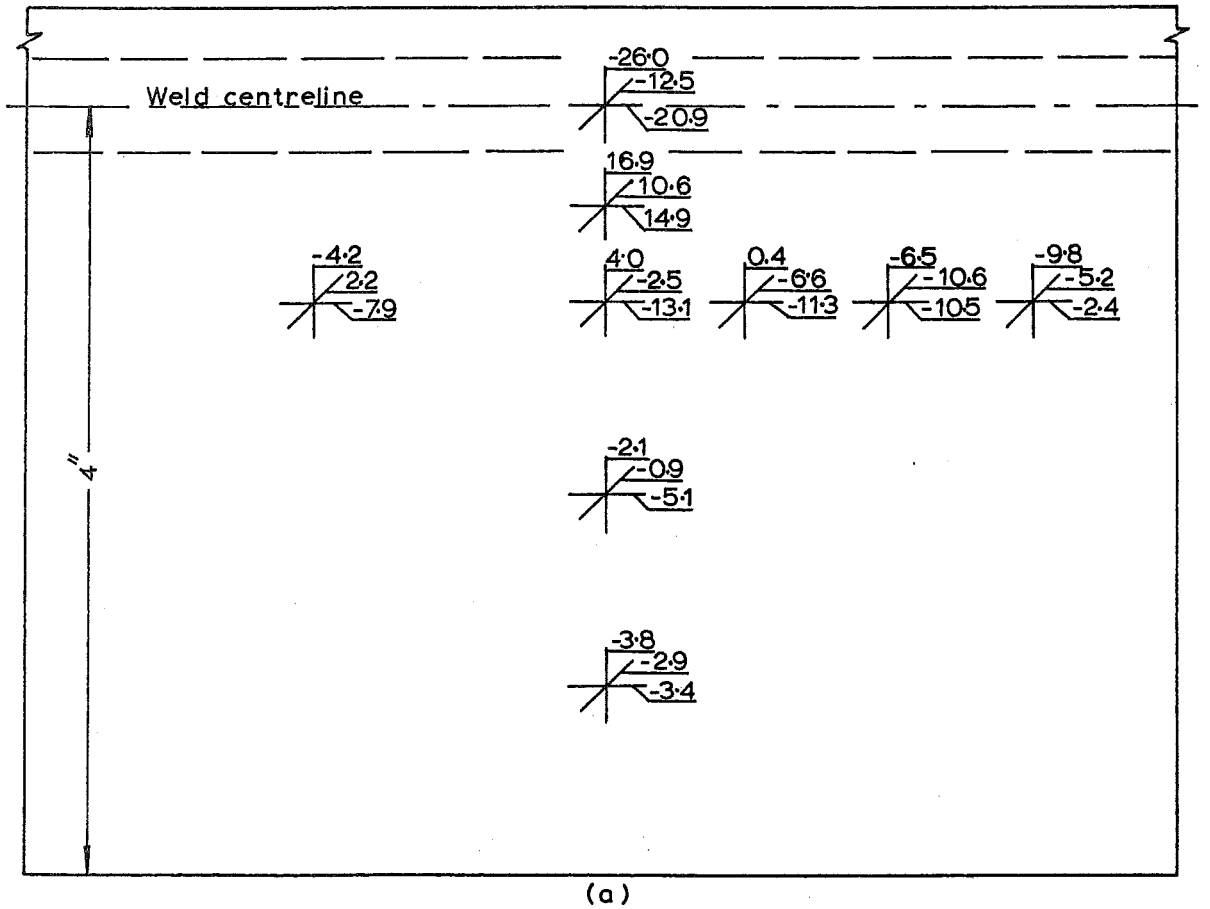

(a)

Fig.7·5 Residual stresses in a machine-welded plate.(kg/mm^2). (double vee weld using short-circuiting arc method)

TABLE 7-4

SPECIMEN No. 4

EDGE PREPARATION: Double Vee Notched.

WELDING TECHNIQUE: Short Circuiting Transfer.

SURFACE PREPARATION: Electropolished.

Point	$\sigma_{\beta=0°}$	$\sigma_{\beta=45°}$	$\sigma_{\beta=90°}$	σ_{max}	σ_{min}	θ_p°
1	-20.86	-12.52	-26.01	-12.22	-34.65	38.36
2	14.91	10.61	16.92	21.31	10.52	39.64
3	-13.09	-2.53	4.00	4.23	-13.32	-6.63
4	-5.14	-0.91	-2.12	-0.52	-6.74	-30.48
5	-3.36	-2.89	-3.84	-2.85	-4.35	35.66
6	-10.48	-10.62	-6.52	-5.60	-11.40	23.48
7	-7.89	2.19	-4.19	2.41	-14.49	-33.00
8	-11.26	-6.64	0.35	0.47	-11.38	5.77
9	-2.36	-5.17	-9.82	-2.25	-9.93	6.93

*stresses are in kg/mm^2 unit.

The residual stress pattern is plotted in Fig. 7.5(a).

and the principal stress pattern is plotted in Fig. 7.5(b).

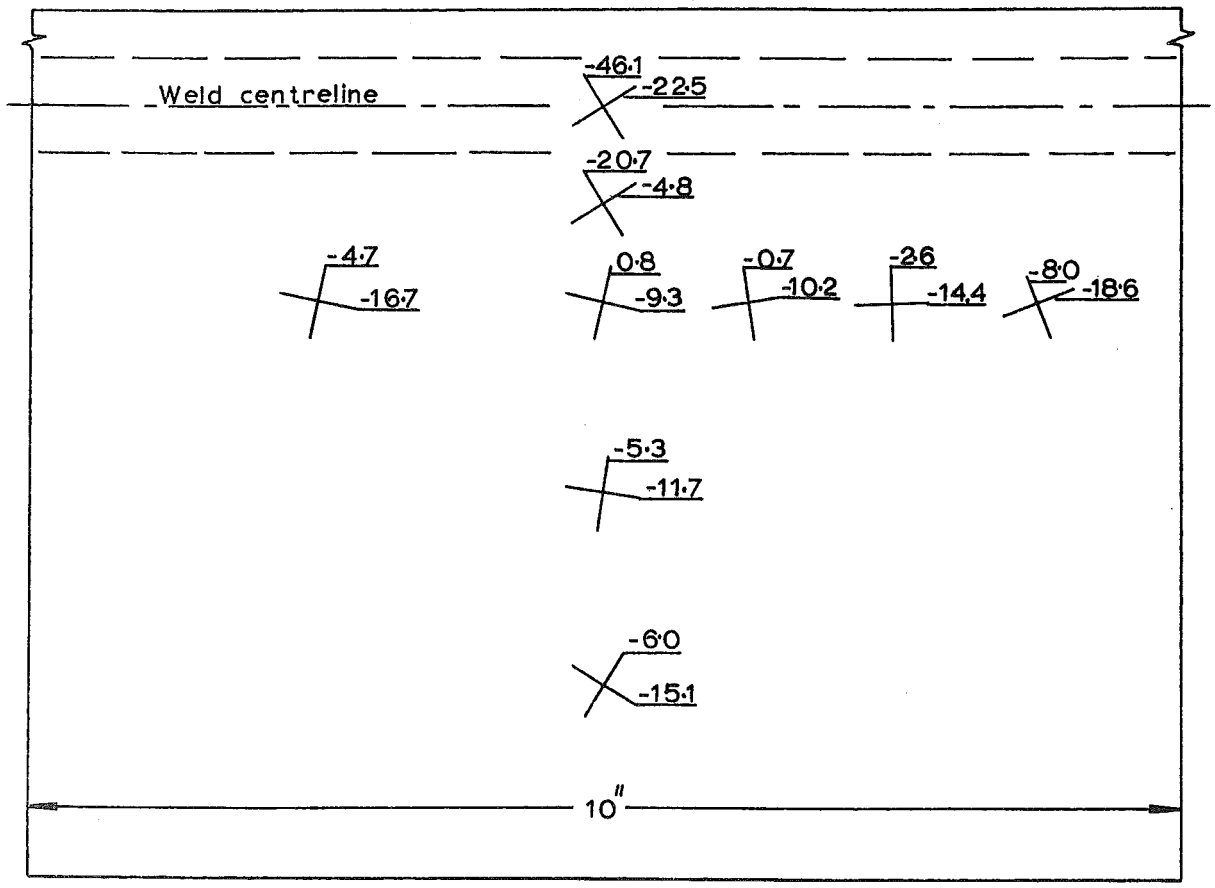

(b)

Principal stresses in a machine-welded plate,(kg/mm^2).
(specimen No.5)

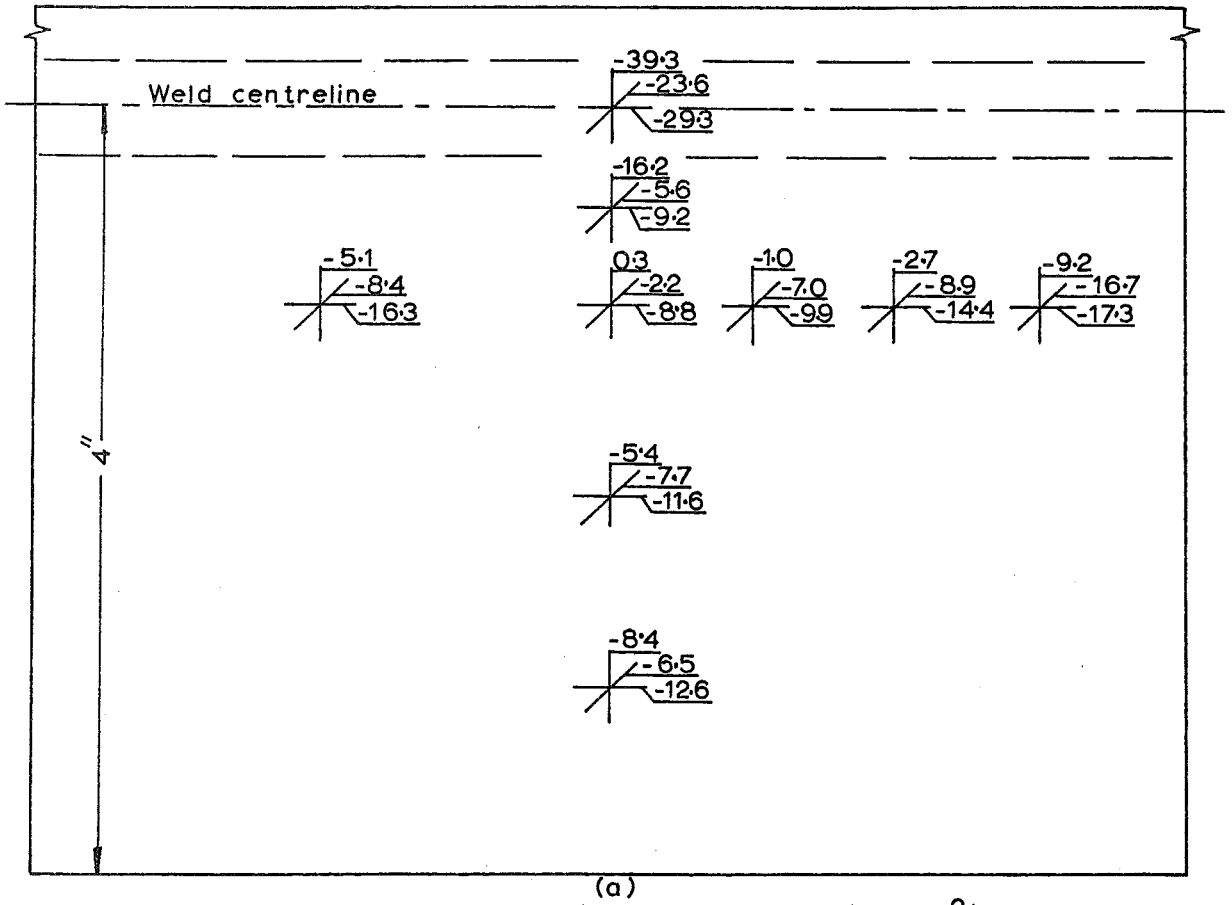

(a)

Fig.7·6 Residual stresses in a machine-welded plate.(kg/mm^2).
(single-vee weld using short circuiting arc method)

TABLE 7-5

SPECIMEN No. 5

EDGE PREPARATION: Single Vee Notched.

WELDING TECHNIQUE: Short Circuiting Transfer.

SURFACE PREPARATION: Electropolished.

Point	$\sigma_{\beta=0°}$	$\sigma_{\beta=45°}$	$\sigma_{\beta=90°}$	σ_{max}	σ_{min}	$\theta_p°$
1	-29.27	-23.57	-39.30	-22.45	-46.12	32.46
2	-9.24	-5.55	-16.23	-4.75	-20.72	32.03
3	-8.82	-2.21	0.32	0.75	-9.25	-12.03
4	-11.55	-7.67	-5.43	-5.32	-11.66	-7.50
5	-12.63	-6.49	-8.44	-5.98	-15.09	-31.31
6	-14.40	-8.91	-2.65	-2.64	-14.41	1.87
7	-16.26	-8.40	-5.13	-4.68	-16.71	-11.21
8	-9.88	-7.01	-0.99	-0.72	-10.15	9.76
9	-17.34	-16.72	-9.24	-7.98	-18.60	20.15

*stresses are in kg/mm^2 unit.

The residual stress pattern is plotted in Fig. 7.6(a).

and the principal stress pattern is plotted in Fig. 7.6(b).

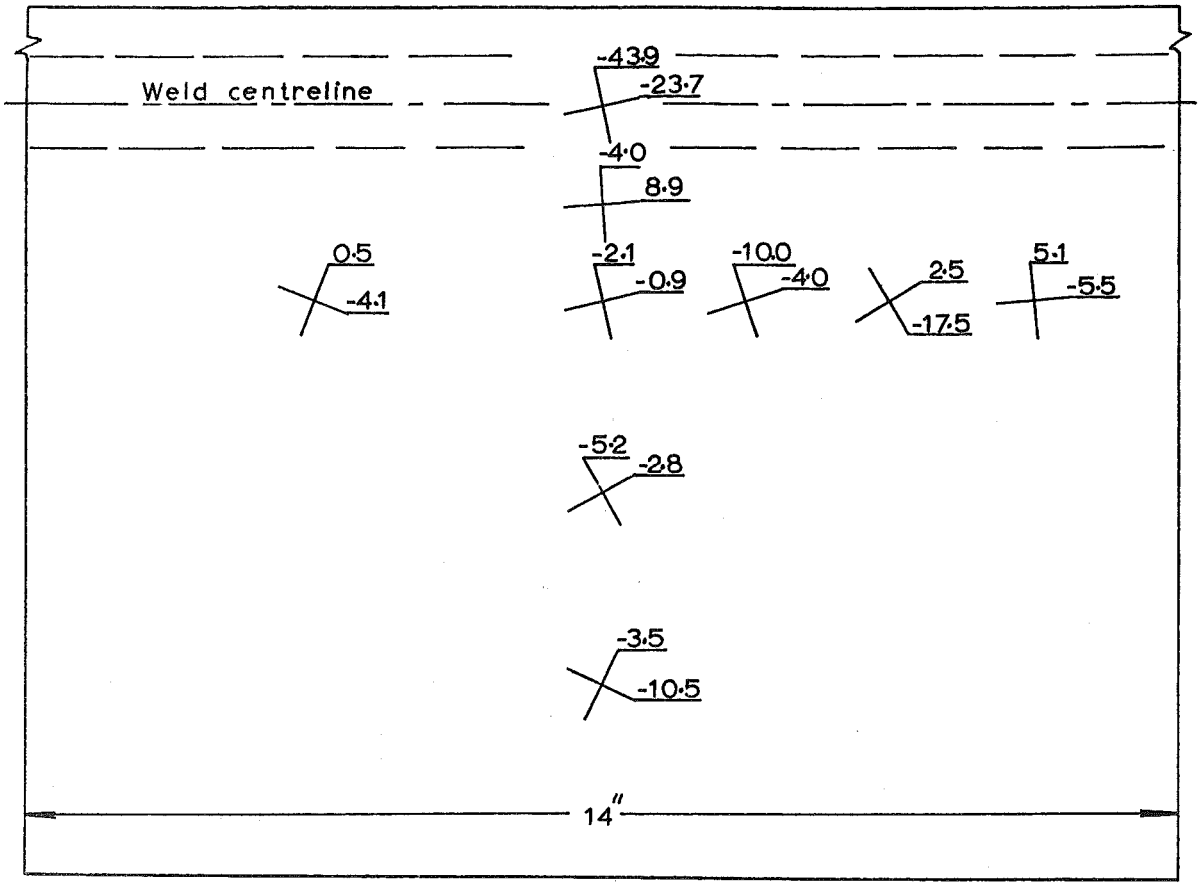

(b)

Principal stresses in machine-welded plate. (kg/mm^2).
(specimen No.6)

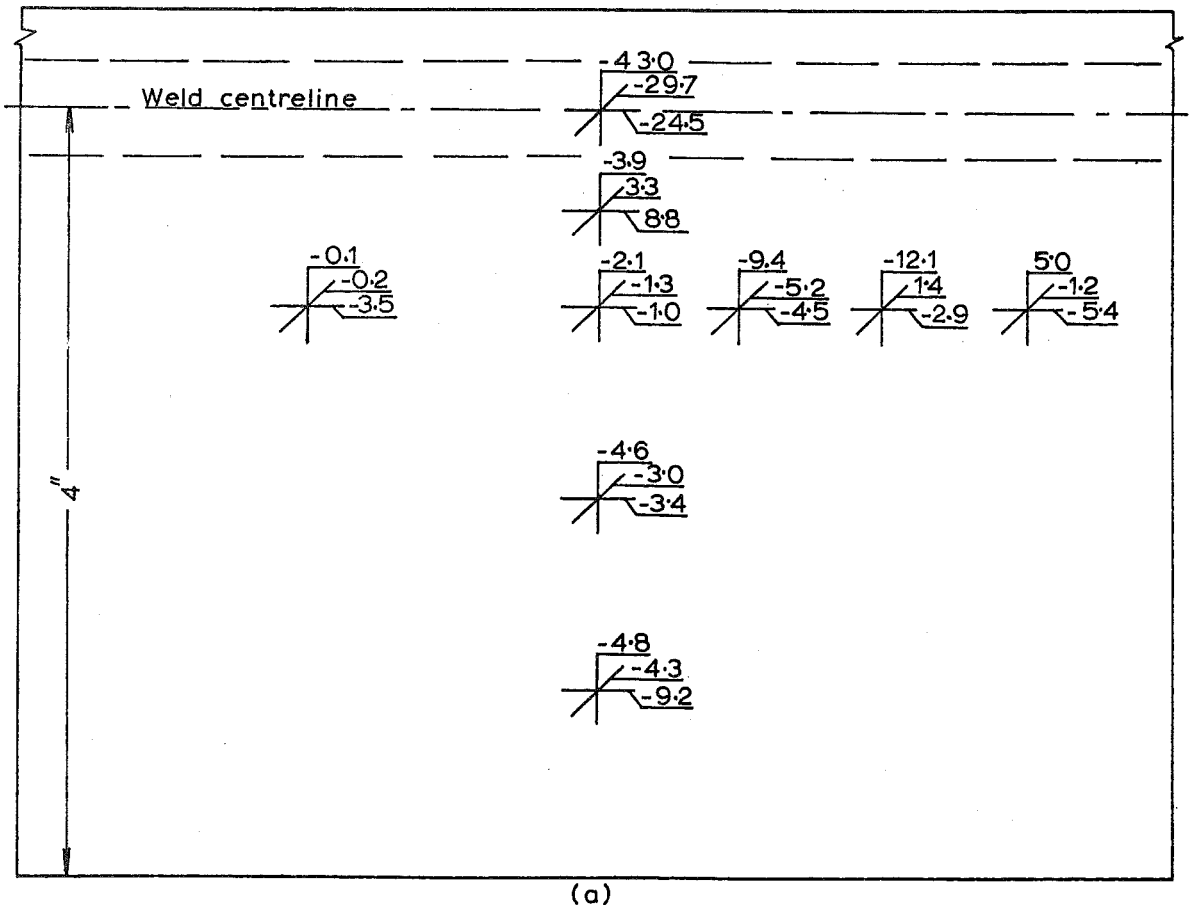

(a)

Fig.7·7 Residual stresses in a machine-welded plate.(kg/mm^2).
(single vee weld using short circuiting arc method)

TABLE 7-6

SPECIMEN No. 6

EDGE PREPARATION: Single Vee Notched.

WELDING TECHNIQUE: Short Circuiting Transfer.

SURFACE PREPARATION: Electropolished.

Point	$\sigma_{\beta=0°}$	$\sigma_{\beta=45°}$	$\sigma_{\beta=90°}$	σ_{max}	σ_{min}	θ_p°
1	-24.53	-29.72	-43.00	-23.68	-43.85	11.83
2	8.80	3.30	-3.94	8.86	-4.00	3.89
3	-0.98	-1.26	-2.06	-0.92	-2.12	12.85
4	-3.36	-2.97	-4.62	-2.79	-5.19	29.15
5	-9.22	-4.33	-4.76	-3.52	-10.46	-25.01
6	-2.90	1.39	-12.08	2.51	-17.49	31.33
7	-3.50	-0.22	-0.10	0.52	-4.12	-21.45
8	-4.52	-5.20	-9.42	-3.95	-9.99	17.92
9	-5.41	-1.23	4.99	5.09	-5.51	5.55

*stresses are in kg/mm^2 unit.

The residual stress pattern is plotted in Fig. 7.7(a).

and the principal stress pattern is plotted in Fig. 7.7(b).